Ingenieurfakultät Bau Geo Umwelt
Signalverarbeitung in der Erdbeobachtung

Object-based Multibaseline SAR Interferometry

Jian Kang

Vollständiger Abdruck der von der Ingenieurfakultät Bau Geo Umwelt der Technischen Universität München zur Erlangung des akademischen Grades eines

Doktor-Ingenieurs (Dr.-Ing.)

genehmigten Dissertation.

Vorsitzender:	Prof. Dr.-Ing. Uwe Stilla
Prüfer der Dissertation:	1. Prof. Dr.-Ing. habil. Xiaoxiang Zhu
	2. Prof. Dr.-Ing. habil. Richard Bamler
	3. Prof. Dr.-Ing. Uwe Sörgel (Schriftliche Beurteilung)

Die Dissertation wurde am 23.05.2019 bei der Technischen Universität München eingereicht und durch die Ingenieurfakultät Bau Geo Umwelt am 02.09.2019 angenommen.

Abstract

By illuminating the scene of interest with electromagnetic signals, Synthetic Aperture Radar plays an important role in remote sensing for producing up to decimeter resolution images of earth from airborne and spaceborne platforms with the most unique advantage of the all-weather capability. By exploiting interferometry of SAR images at different acquisition time stamps, geophysical parameters, such as heights and displacement rates, can be extracted by signal processing algorithms.

At the sensor level, spaceborne SAR systems have met an unprecedented growth in recent years. For instances, X-Band missions like TerraSAR-X [WB10] and COSMO-SkyMed [Cal+14] can achieve up to 1 m resolution. Aimed for the displacement mapping at a high time frequency, Sentinel-1 satellites [Fle12] have the capability for earth observation by every six days. Japan's ALOS-2 satellite [MKS17] can supply "colorful" SAR observations globally by its full polarization. At the algorithm level, extensive research has been done for geophysical information extraction from SAR images in decades. With respect to different scattering cases, i.e. point scatterers and distributed scatterers, prevalent algorithms can be split into two categories: Persistent Scatterer Interferometry (PSI) and Distributed Scatterer Interferometry (DSI).

Although the conventional techniques for geophysical parameter estimation do exploit information from multiple neighbouring pixels, no explicit semantic and geometric information that might be preserved in the images has been utilized. Such geometric information can be the object mask of a building façade where the height and deformation obey certain prior knowledge, such as continuity and smoothness. Introducing them into the retrieval of phase history parameters can be of great advantage. Moreover, investigation of property inherent in object-based Interferometric SAR (InSAR) data stacks can be further assisted to the improvement of geophysical parameter estimation.

A general framework for object-based InSAR parameter retrieval, where the parameters of the whole object are jointly estimated by the inversion of a regularized tensor model instead of pixelwise, is developed in this thesis. In typical settings without outliers, the proposed method outperforms the current pixelwise estimators, e.g., periodogram, by a factor of at least two in the accuracy of the linear deformation estimates.

The inherent low rank property of object-based InSAR phase stacks is further investigated in this thesis. Based on that, two tensor-decomposition based methods are proposed for robustly reconstructing object-based InSAR phase stacks. Without requiring the precise segmentation of object masks, the proposed methods can be efficiently exploited for object-based geophysical parameter estimation. In cases of InSAR data corrupted by outliers, the methods can improve the accuracy of geophysical parameters estimated via conventional multibaseline InSAR techniques, e.g. PSI, by a factor of ten to thirty in typical settings.

Last but not least, an extension of robust low rank tensor decomposition to Distributed

Scatterer (DS) InSAR phase tensors is also proposed. Under the typical parameter setting of TanDEM-X, the proposed method shows the out-performance of the elevation estimation by a factor of two compared to other state-of-the-art methods, such as SqueeSAR. With the application on 3D reconstruction of a mountainous area based on TanDEM-X bistatic InSAR stack, the performance of the method is further validated.

Zusammenfassung

Durch die Beleuchtung der interessierenden Szene mit elektromagnetischen Signalen spielt SAR (Synthetic Aperture Radar) eine wichtige Rolle bei der Fernerkundung, um eine Auflösung von bis zu Dezimeter zu erreichen Bilder von der Erde von Plattformen in der Luft und im Weltraum mit dem einzigartigen Vorteil der Allwetterfähigkeit. Durch Ausnutzung der Interferometrie von SAR-Bildern bei verschiedenen Erfassungszeitstempeln können geophysikalische Parameter wie Höhen und Verschiebungsraten durch Signalverarbeitungsalgorithmen extrahiert werden.

Auf Sensorebene haben weltraumgestützte SAR-Systeme in letzter Zeit ein beispielloses Wachstum erfahren Jahre. X-Band-Missionen wie TerraSAR-X [WB10] und COSMO-SkyMed [Cal+14] können beispielsweise eine Auflösung von bis zu 1 m erreichen. Sentinel-1-Satelliten [Fle12] sind für die Verschiebungskartierung bei einer hohen Zeitfrequenz ausgelegt und bieten die Möglichkeit, alle sechs Erdbeobachtungen durchzuführen Tage. Der japanische Satellit ALOS-2 [MKS17] kann durch seine vollständige Polarisierung "farbenfrohe" SAR-Beobachtungen weltweit liefern. Auf der Algorithmusebene wurden seit Jahrzehnten umfangreiche Untersuchungen zur Gewinnung geophysikalischer Informationen aus SAR-Bildern durchgeführt. In Bezug auf unterschiedliche Streuung d.h. Punktstreuer und verteilte Streuer können die vorherrschenden Algorithmen in zwei Kategorien unterteilt werden: Persistent Scatterer Interferometry (PSI) und Distributed Scatterer Interferometrie (DSI).

Obwohl die herkömmlichen Techniken zur geophysikalischen Parameterschätzung Informationen aus mehreren benachbarten Pixeln ausnutzen, wurden keine expliziten semantischen und geometrischen Informationen verwendet, die in den Bildern erhalten bleiben könnten. Solche geometrischen Informationen kann die Objektmaske einer Gebäudefassade sein, deren Höhe und Verformung sicher gehorchen Vorkenntnisse wie Kontinuität und Laufruhe. Einführung in das Abrufen von Phasenverlaufsparameter können von großem Vorteil sein. Darüber hinaus kann die Untersuchung der Eigenschaften objektbasierter interferometrischer SAR (InSAR) -Datenstacks weiter unterstützt werden Verbesserung der geophysikalischen Parameterschätzung.

Ein allgemeiner Rahmen für den objektbasierten InSAR-Parameter-Abruf, bei dem die Parameter von Das gesamte Objekt wird stattdessen gemeinsam durch die Inversion eines regulierten Tensormodells geschätzt von pixelweise, wird in dieser Arbeit entwickelt. Bei typischen Einstellungen ohne Ausreißer übertrifft das vorgeschlagene Verfahren die aktuellen Pixelschätzer, z. B. das Periodogramm, um einen Faktor von mindestens zwei bei der Genauigkeit der linearen Deformationsschätzungen.

Die inhärente Eigenschaft eines niedrigen Rangs von objektbasierten InSAR-Phasenstapeln wird weiter untersucht in dieser These. Darauf aufbauend werden zwei auf Tensorzersetzung basierende Verfahren für vorgeschlagen Objektbasierte InSAR-

Phasenstapel auf robuste Weise rekonstruieren. Ohne die genaue Segmentierung von Objektmasken zu erfordern, können die vorgeschlagenen Verfahren effizient für die objektbasierte geophysikalische Parameterschätzung verwendet werden. In Fällen von InSAR-Daten, die durch Ausreißer beschädigt wurden, können die Verfahren die Genauigkeit geophysikalischer Parameter verbessern, die mit herkömmlichen Multibaseline-InSAR-Techniken geschätzt werden, z. PSI um den Faktor 10 bis 30 in typischen Umgebungen.

Nicht zuletzt wird auch eine Erweiterung der robusten Tensorzerlegung mit geringem Rang auf InSAR-Phasentensoren mit verteilter Streuung (DS) vorgeschlagen. Unter der typischen Parametereinstellung Bei TanDEM-X zeigt das vorgeschlagene Verfahren die Outperformance der Höhenschätzung um den Faktor zwei im Vergleich zu anderen Methoden des Standes der Technik, wie z. B. SqueeSAR. Mit der Anwendung zur 3D-Rekonstruktion eines Berggebiets auf Basis von TanDEM-X bistatic InSAR Stack wird die Leistung der Methode weiter validiert.

Table of contents

Acronyms and initialisms

AD Anderson–Darling 26, 27, 85, 87, 89, 90, 119

ADMM Alternating Direction Method of Multipliers 14, 15, 17, 22, 23, 30, 33–35, 40–44, 52, 59, 60, 78, 97

APES amplitude and phase estimation filter 28

APS atmospheric phase screen 20

BCD Block Coordinate Descent 34

CCG complex circular Gaussian 19, 26, 27

CS compressive sensing 29

D-TomoSAR Differential SAR Tomography 28

DLR Deutsches Zentrum für Luft- und Raumfahrt (engl. German aerospace center) 46, 50, 52, 115

DOA directions of arrival 28

DS Distributed Scatterer

DSI Distributed Scatterer Interferometry 13, 25, 27, 28

FFT Fast Fourier Transform 34, 77

GLRT generalized likelihood-ratio test 25, 27

HoRPCA High order Robust Principal Component Analysis 43, 55, 59, 61, 62, 116, 121

HoSVD Higher order Singular Value Decomposition 56, 58, 115

i.i.d. independent and identically distributed 53

ILS integer least squares 27, 85–87

InSAR Interferometric Synthetic Aperture Radar (SAR)

KKT Karush–Kuhn–Tucker 40

KS Kolmogorov–Smirnov 13, 26, 27, 85

LAMBDA least squares ambiguity decorrelation 26, 27

LBP local binary pattern 47

LiDAR light detection and ranging

LOS line-of-sight 20

MAP maximum *a posteriori* 29, 32, 43

MLE maximum likelihood estimator 26–28, 31, 37, 38, 85, 114

MM multimaster 27

MSE mean squared error 57, 58, 61, 62, 66, 116, 117, 121

MST minimum spanning tree 48

MUSIC multiple signal classification 28

NP non-deterministic polynomial-time 59

NSS nonlocal self-similarity 27

NST Nonuniform Soft Thresholding 60

NSVT Nonuniform Singular Value Thresholding 59, 60

OSM OpenStreetMap 14, 29

PCA Principal Component Analysis 53, 56

PDF probability density function 21, 82, 119

PS Persistent/Permanent Scatterer

PSI Persistent Scatterer Interferometry 13, 25, 26, 28–30, 36–38, 44, 46, 50, 60–62, 64–70, 72–76, 78, 80–82, 85, 87, 89–91, 97, 113, 114, 116–119

RELAX modern parametric relaxation spectral estimator 28

RoMIO Robust Mutibaseline InSAR technique via Object-based low rank tensor decomposition 30, 53, 60–62, 64–70, 72–74, 76, 78, 80–83, 97, 116–119, 121

RPCA Robust Principal Component Analysis 55

SAR Synthetic Aperture Radar

SBAS small baseline subset 26, 27

SHP Statistically Homogeneous Pixels 13, 21, 26, 27, 85–87, 89

SM single-master 27, 28

SNR signal-to-noise ratio 25, 38, 39, 41, 44, 50, 52, 61, 62, 68, 85, 97, 114, 116

StaMPS stanford method for persistent scatterers 25

SVD singular value decomposition 28, 43, 56, 60

SVM Support Vector Machine 47

SVT Singular Value Thresholding 43, 44, 77

TGV total generalized variation 39, 41, 42, 97, 114

TomoSAR SAR Tomography 28, 29, 46, 47, 85, 98

TV total variation 14, 30, 33–42, 44, 45, 50, 51, 53, 76, 81–83, 97, 98, 113–115, 119

Notation and symbols

$|\cdot|$ absolute operator

$\mathbf{C}$ complex covariance matrix

$\overline{u}$ complex conjugate

$\mathbb{E}[\cdot]$ expected value of a random variable

φ interferometric phase

$\mathbf{X}$ matrix

(R_1, R_2, R_3) tensor multilinear rank

$\otimes$ outer product

ϕ phase

$\odot$ element-wise product

$\|\mathscr{E}\|_1$ L_1 norm of tensor

$\|\mathscr{X}\|_*$ tensor nuclear norm

$\mathscr{X}$ tensor

$\mathbf{X}_{(n)}$ mode-n unfolding of tensor $\mathscr{X}$

$\mathbf{b}$ vector

λ wavelength

1 Introduction

1.1 Motivation

By illuminating the scene of interest with electromagnetic signals, SAR plays an important role in remote sensing for producing up to decimeter resolution images of earth from airborne and spaceborne platforms with the most unique advantage of the all-weather capability. By exploiting interferometry of SAR images at different acquisition time stamps, geophysical parameters, such as heights and displacement rates, can be extracted by signal processing algorithms.

At the sensor level, spaceborne SAR systems have met an unprecedented growth in recent years. For instances, X-Band missions like TerraSAR-X [WB10] and COSMO-SkyMed [Cal+14] can achieve up to 1 m resolution. Aimed for the displacement mapping at a high time frequency, Sentinel-1 satellites [Fle12] have the capability for earth observation every six days. Japan's ALOS-2 satellite [MKS17] can supply "colorful" SAR observations globally by its full polarization. At the algorithm level, extensive research has been done for geophysical information extraction from SAR images. With respect to different scattering cases, i.e. point scatterers and distributed scatterers, prevalent algorithms can be split into two categories: Persistent Scatterer Interferometry (PSI) [FPR01; Ada+03; FPS09; Sou+11; GB12; Kam06; WZB14; Cos+14; ZDL11; DMFP09] and Distributed Scatterer Interferometry (DSI) [Fer+11; GA12; WZB12; Jia+15; SE+16; WZ16; CLJ16]. Generally, the key steps of PSI involve Persistent/Permanent Scatterer (PS) candidate identification and parameter estimation. For example, PS pixels can be selected according to *amplitude dispersion index*, which can be calculated by the ratio between the temporal standard deviation and mean of the amplitudes [FPR01]. In order to extract geophysical information from non-urban areas with Distributed Scatterer (DS), interferometry techniques for parameter estimation from such stochastic signals have been extensively carried out in decades. Normally, Statistically Homogeneous Pixels (SHP) selection for covariance matrix estimation and optimal phase history retrieval from such covariance matrices are the two key steps in DS interferometry. As introduced in [Fer+11], SqueeSAR exploits Kolmogorov–Smirnov (KS) test for selecting SHP with the assumption that the statistics of amplitude data can be seen as a proxy for phase stability.

Although those conventional techniques for geophysical parameter estimation do exploit information from multiple neighbouring pixels, no explicit semantic and geometric information that might be preserved in the images has been utilized. Such geometric information can be the object mask of a building façade where the height and deformation obey certain prior knowledge, such as continuity and smoothness. Introducing them into the retrieval of phase history parameters can be of great advantage, for example, to improve the accuracy of the estimates, or to reduce the number of images required to obtain a reliable estimation. In one pioneer work [ZGS15a], Zhu *et al.* demonstrated that by introducing building footprints from

OpenStreetMap (OSM) as prior knowledge of pixels sharing similar heights into frameworks based on joint sparse reconstruction techniques, a highly accurate tomographic reconstruction can be achieved using just six interferograms, instead of the typically-required 20-100.

1.2 Objective

The objective of this thesis is to investigate the advanced Interferometric SAR (InSAR) signal processing methods for geophysical parameter estimation at an object-based level. By integrating prior knowledge, such as total variation (TV), into the geophysical parameter reconstruction models, the proposed methods in this thesis demonstrate the novelty in threefold:

- Geophysical parameter estimation improvement for both PS and DS signals.
- Reliable estimation results reconstructed with limited number of SAR images.
- Robust geophysical parameter estimation in the existence of outliers.

For reaching those goals, this thesis addresses three separate parts of research.

Object-based multibaseline InSAR geophysical parameter estimation

Development of object-based multibaseline InSAR geophysical parameter estimation framework, with the application of object masks extracted from optical images. Such framework takes advantage of prior knowledge of the spatial smoothness for the joint optimization of geophysical parameters and the solver based on Alternating Direction Method of Multipliers (ADMM) is introduced.

Low-rank analysis in object-based multibaseline InSAR

For objects in urban areas, high-coherence of SAR images along the temporal direction and pixel similarity along the spatial direction lead to the inherent low-rank nature in multibaseline InSAR data stacks. Such property is investigated in this chapter and two novel tensor decomposition methods are also proposed. Moreover, the object-based semantic masks required for geophysical parameter reconstruction can be loosed, when low rank tensor decomposition methods are exploited.

Robust low rank tensor decomposition for Distributed Scatterer

Besides the application of tensor decomposition based methods on PS, the corresponding framework is extended for cases of DS. With a limited number of SAR interferograms (around six), the proposed method demonstrates the reliable performance of geophysical parameter reconstruction and outperforms other the state-of-the-art multibaseline InSAR techniques for DS, such as SqueeSAR [Fer+11] and PD-PSInSAR [CLJ16].

1.3 Organization of this thesis

Chapter 2 briefly introduces basics of SAR imaging, signal models of SAR interferogram pixels, tensor and the ADMM optimization framework. Chapter 3 gives an overview of current technologies for mutlibaseline InSAR technologies. Chapter 4 introduces the framework of object-based multibaseline InSAR geophysical parameter estimation. Chapter 5 investigates the low-rank property inherent in InSAR data stacks and propose two novel tensor decomposition methods for robustly recovering geophysical parameters. Chapter 6 presents the extension of tensor decomposition based method for DS and demonstrates the superiority to other methods on the 3D reconstruction of a TanDEM-X bistatic InSAR stack on a mountainous area. Chapter 7 draws a conclusion of this thesis and discusses some potential further research directions.

2 Basics

This chapter briefly describes SAR principles, imaging models, acquisition geometries, signal models of InSAR and basics of tensor and ADMM optimization framework, which provide a knowledge background for the following chapters. For the detailed introduction of each topic, the readers are suggested to refer to [BH98; Buc00; Mor+13; Ros+00; KB09; Cic+15; Boy+11].

2.1 Synthetic Aperture Radar imaging mode

By illuminating the scene of interest with electromagnetic signals, conventional SAR measures the backscattering coefficients and the location of targets in a two-dimensional image coordinate system, with one axis along the along-track direction, also called *azimuth* direction, and the other axis defined as cross-track direction, also known as *range* direction. Figure 2.1 demonstrates its side-looking geometry. In the range direction, SAR system measures the time it takes a radar pulse to the target and return to the radar and in the azimuth direction, the location is determined by the Doppler frequency shift whenever the relative velocity between the target and radar is not zero [Ros+00]. Commonly utilized microwave lengths of SAR systems are designed as $2.4-3.8$ cm (X-band), $3.8-7.5$ cm (C-band) or $15-30$ cm (L-band).

Along the range direction, targets are distinguished by measuring the runtime of their reflected echos, and the corresponding range resolution:

$$\delta_{\mathrm{r}} = \frac{c}{2B} \tag{2.1}$$

is determined by the bandwidth B of the transmitted signals and the speed of light [Mor+13]. For the azimuth direction, its resolution is limited by the length of the physical antenna and also the distance from the sensor to the illuminated scene. Through the forward movement of the sensor and coherent processing of the reflected echos, synthetic aperture in the azimuth direction can be built up. By doing so, SAR system can greatly improve the azimuth resolution, which is only dependent of its physical antenna size d_{A}:

$$\delta_{\mathrm{az}} = \frac{d_{\mathrm{A}}}{2}. \tag{2.2}$$

2.2 SAR signal model

As shown in Figure 2.2, within one resolution cell of a SAR image, the total signal returned from it is the *coherent* sum of the returns from all the individual scatterers [Buc00; Ros+00;

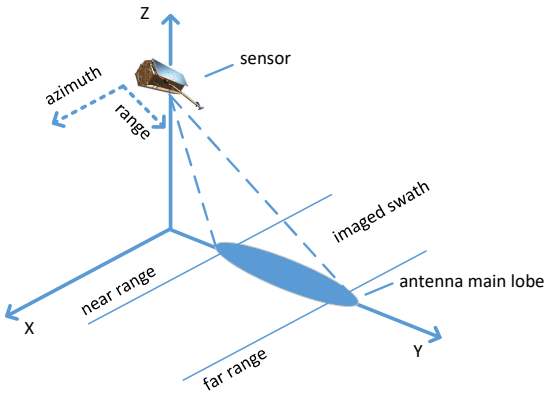

Figure 2.1: SAR image acquisition geometry. SAR system measures the time it takes a radar pulse to the target and return to the radar and in the azimuth direction, the location is determined by the Doppler frequency shift whenever the relative velocity between the target and radar is not zero.

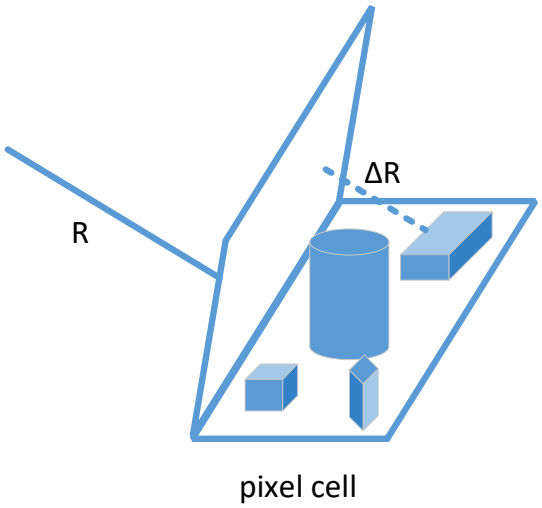

Figure 2.2: Within one resolution cell of a SAR image, the total signal returned from it is the *coherent* sum of the returns from all the individual scatterers.

Mor+13], which can be represented as:

$$g = A_{\mathrm{B}} \exp(j(\phi_{\mathrm{B}} - \frac{4\pi}{\lambda} R)) = \exp(-j\frac{4\pi}{\lambda} R) \times \sum_{i=1}^{N} a_i \exp(j(\phi_i - \frac{4\pi}{\lambda} \Delta R_i)), \tag{2.3}$$

where A_{B} and ϕ_{B} are backscatter amplitude and phase of a resolution cell, λ is the wavelength of the transmitted echo, R is the range between the sensor and the resolution cell, a_i and ϕ_i are backscatter amplitude and phase of ith scattering element in the cell, ΔR_i is the associated differential range, and N is the total number of scattering elements. In particular, $\exp(-j\frac{4\pi}{\lambda} R)$ is the phase contribution by range and $\sum_{i=1}^{N} a_i \exp(j(\phi_i - \frac{4\pi}{\lambda} \Delta R_i))$ is the signal contribution by the coherent sum of the phases induced by differential ranges and backscatter phases returned from the scattering elements within the resolution cell. The amplitude and phase of the backscattered signals are dependent on the physical and electrical properties of the observed targets [Mor+13].

There are normally two cases of scattering elements: point scatterers and DS.If there is one scatterer remarkably dominating the others in the resolution cell, which leads to the main contribution of the backscatter phase, we can call that point scatter. If the point scatter is highly coherent throughout the whole stack of SAR images, it is then known as PS. PS usually exists in urban areas, especially for man-made objects such as building walls, railway lines, lamp posts and windowpanes, and also happens for high-resolution systems. DS are those that can be decomposed into a sufficiently high number of random scattering elements within the resolution cell, with the assumption that there is no single scattering element dominates the others [BH98]. Based on the *central limit theorem*, the signal contributed by all the scattering elements of such resolution cell can be considered as complex circular Gaussian (CCG) variable with its amplitude following Rayleigh distribution and a uniformly distributed phase [DR+58]. DS usually happens in non-urban areas and for natural objects in medium resolution (around 10m) system.

2.3 InSAR signal model

As illustrated in Figure 2.3, by the multiplication of one SAR image taken at position O_1 with the complex conjugate of another SAR image acquired at a nearby position O_2, the corresponding interferogram can be generated. Note that co-registration of the two SAR images is conducted before the interferogram generation, in order to ensure the signals of the corresponding resolution cells are from the same elemental scatterers [Mor+13]. Within each resolution cell, its phase is dependent on the corresponding range difference [BH98], described as:

$$\varphi = \frac{4\pi}{\lambda} \Delta R. \tag{2.4}$$

After removing the phase contribution due to the reference surface, the flattened interferometric phase can be represented by:

$$\varphi_{\mathrm{flat}} = \varphi_{\mathrm{topo}} + \varphi_{\mathrm{defor}} + \varphi_{\mathrm{atm}} + \varphi_{\mathrm{noise}}, \tag{2.5}$$

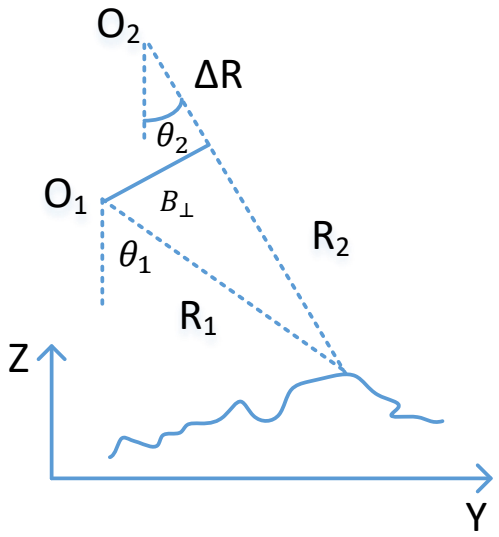

Figure 2.3: Across-track SAR interferometry generated by the multiplication of one SAR image taken at position O_1 with the complex conjugate of another SAR image acquired at a nearby position O_2.

where φ_{topo} represents the phase contributed by topography, φ_{defor} refers to the deformation phase due to the slight displacement of the targets in the direction of the satellite line-of-sight (LOS), φ_{atm} denotes the phase induced by atmospheric effects, which is termed as atmospheric phase screen (APS) [ZRH97; Han01], and φ_{noise} is the phase noise. Specifically, φ_{topo} is determined by $-\frac{4\pi}{\lambda}\frac{B_\perp}{R\sin\theta}h$ with perpendicular baseline of two images $B_\perp$, topography height h and the incidence angle θ. If the two images are acquired at different times, φ_{atm} and φ_{defor} should be considered.

As an extension to multibaseline InSAR case, the corresponding interferometric phase vector can be formulated as:

$$\boldsymbol{\varphi}_{\text{flat}} = -\frac{4\pi}{\lambda}\frac{\mathbf{b}}{R\sin\theta}h + \boldsymbol{\varphi}_{\text{defor}} + \boldsymbol{\varphi}_{\text{atm}} + \boldsymbol{\varphi}_{\text{noise}}, \tag{2.6}$$

where $\mathbf{b}$ is the vector of perpendicular baselines, $\boldsymbol{\varphi}_{\text{defor}}$ is the deformation phase vector, and $\boldsymbol{\varphi}_{\text{atm}}$ represents APS phase vector. Normally, $\boldsymbol{\varphi}_{\text{defor}}$ can be modeled as a function with respect to the acquisition time $\mathbf{t}$. APS is usually assumed to be spatially low-frequency and temporally uncorrelated. The deterministic models described in Equation (2.5) and Equation (2.6) are applied for the case of PS. If the pixel is DS, both are the expected values of interferometric phases.

2.4 Single-look InSAR statistics

Coherence is one of the key parameters to measure the decorrelation of DS between two co-registered SAR images. Such decorrelation can be summarized as follows [ZV92]:

- *Temporal decorrelation*: Backscattering property change of the scene between different acquisition times, especially that the observed areas are vegetated or prone to snow coverage.
- *Spatial decorrelation*: Different incidence angles at the two times at which the SAR images are acquired.

Correspondingly, it has the following formula:

$$\gamma_c = \frac{\mathbb{E}[g_1 g_2^*]}{\sqrt{\mathbb{E}[|g_1|^2]\mathbb{E}[|g_2|^2]}}, \tag{2.7}$$

where expected value of a random variable is denoted as $\mathbb{E}[\cdot]$. In practice, it is usually conducted by averaging L adjacent looks with the assumption of local stationarity. The coherence magnitude ranges from 0 to 1, where 0 represents the complete decorrelation and 1 means the full coherence. Correspondingly, the joint probability density function (PDF) of the interferometric amplitude and phase can be represented as [Lee+94; TBQ95; BH98]:

$$p_{|v|,\varphi}(|v|,\varphi) = \frac{2|v|}{\pi \bar{I}^2(1-|\gamma_c|^2)} \exp\left(\frac{2|\gamma_c||v|\cos(\varphi-\bar{\varphi})}{\bar{I}(1-|\gamma_c|^2)}\right) K_0\left(\frac{2|v|}{\bar{I}(1-|\gamma_c|^2)}\right), \tag{2.8}$$

where $\bar{I} = \sqrt{\mathbb{E}[|g_1|^2]\mathbb{E}[|g_2|^2]}$, $\bar{\varphi}$ denotes the expected interferometric phase and $K_0(\cdot)$ is the modified Bessel function. As a generation to multibaseline SAR images of DS, the corresponding joint PDF can be formulated as [GT08; WZ16]:

$$p(\mathbf{g}|\mathbf{C}) = \frac{1}{\pi^N \det(\mathbf{C})} \exp(-\mathbf{g}^H \mathbf{C}^{-1} \mathbf{g}), \tag{2.9}$$

where N is the number of SAR images, $(\cdot)^H$ indicates the Hermitian transpose operator and $\mathbf{C} = \mathbb{E}(\mathbf{g}\mathbf{g}^H)$ denotes the complex covariance matrix. Likewise, it is usually calculated by averaging L adjacent SHP.

2.5 Tensor

With the emergence of big data, standard flat-view matrix models cannot usually fulfill the requirements of data analysis. Benefiting from multilinear algebra, high-dimensional data can be flexibly represented as *tensor* and more general latent components in the data can be extracted from tensor-based than matrix-based methods. Tensor-based methods have been widely exploited in the fields of signal processing, computer vision and machine learning for the study of videos, hyperspectral images and 3D medical images, *etc.* [KB09; Cic+15; Sid+17; PFS17].

A tensor can be considered as a multi-dimensional array. The *order* of a tensor is the number of its *modes* or *dimensions*. A tensor of order N in the complex domain can be denoted as $\mathscr{X} \in \mathbb{C}^{I_1 \times I_2 \cdots \times I_N}$ and its entries as $x_{i_1,i_2,\cdots,i_N}$. Specifically, vector $\mathbf{x}$ is a tensor of order one, and $\mathbf{X}$ can be represented as a tensor of order two. *Fibers* are the higher-order analogy of matrix rows and columns, which are defined by fixing every index but one. *Slices* of a tensor are

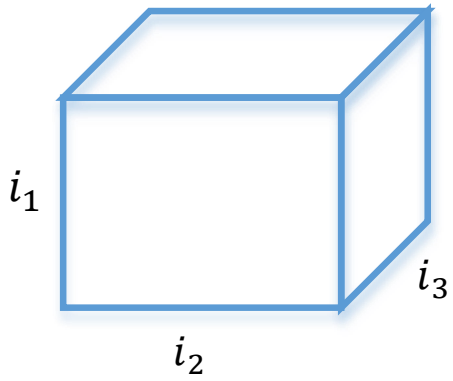

Figure 2.4: Third-order tensor (3D array).

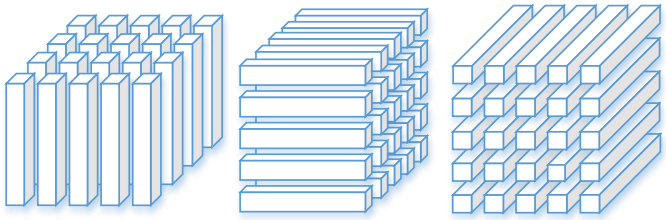

Figure 2.5: Fibers.

obtained by fixing all but two indices. Matricization, also known as *unfolding*, is the process of reordering the elements of a tensor into a matrix. Specifically, mode-n unfolding of tensor $\mathcal{X}$ is defined by $\mathbf{X}_{(n)}$ that is obtained by arranging the mode-n fibers as the columns of the matrix. An example of a third-order tensor, its fibers and slices are displayed in Figure 2.4, Figure 2.5 and Figure 2.6, respectively.

2.6 Alternating Direction Method of Multipliers

ADMM is an optimization framework for solving the following problem:

$$\underset{\mathbf{x},\mathbf{y}}{\operatorname{argmin}} f_1(\mathbf{x}) + f_2(\mathbf{y}), \quad s.t. \ \mathbf{A}\mathbf{x} + \mathbf{B}\mathbf{y} = \mathbf{c}, \tag{2.10}$$

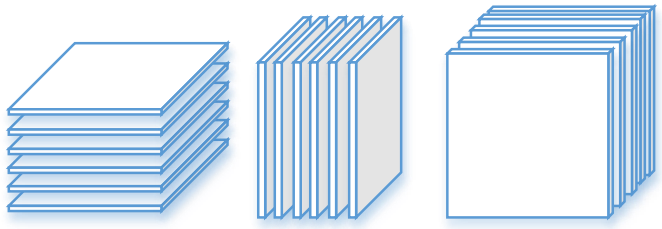

Figure 2.6: Slices.

with variables $\mathbf{x} \in \mathbb{C}^n$ and $\mathbf{y} \in \mathbb{C}^m$, where $\mathbf{A} \in \mathbb{C}^{p \times n}$, $\mathbf{B} \in \mathbb{C}^{p \times m}$ and $\mathbf{c} \in \mathbb{C}^p$. Correspondingly, its augmented Lagrangian form is:

$$L_\rho(\mathbf{x}, \mathbf{y}, \mathbf{u}) = f_1(\mathbf{x}) + f_2(\mathbf{y}) + \langle \mathbf{u}, \mathbf{A}\mathbf{x} + \mathbf{B}\mathbf{y} - \mathbf{c} \rangle + \frac{\rho}{2} \|\mathbf{A}\mathbf{x} + \mathbf{B}\mathbf{y} - \mathbf{c}\|_2^2, \tag{2.11}$$

where ρ is the *penalty parameter* and $\mathbf{u}$ is the *dual variable* related to the constraint $\mathbf{A}\mathbf{x} + \mathbf{B}\mathbf{y} = \mathbf{c}$. By taking the advantages of splitting one difficult optimization problem into several subproblems, where each of them has a closed-form solution, Equation (2.10) can be solved by iterating over the steps:

$$\mathbf{x}^{(i+1)} = \underset{\mathbf{x}}{\operatorname{argmin}}\, f_1(\mathbf{x}) + \frac{\rho}{2} \|\mathbf{A}\mathbf{x} + \mathbf{B}\mathbf{y}^{(i)} - \mathbf{c} + \frac{\mathbf{u}^{(i)}}{\rho}\|_2^2, \tag{2.12}$$

$$\mathbf{y}^{(i+1)} = \underset{\mathbf{y}}{\operatorname{argmin}}\, f_2(\mathbf{y}) + \frac{\rho}{2} \|\mathbf{A}\mathbf{x}^{(i+1)} + \mathbf{B}\mathbf{y} - \mathbf{c} + \frac{\mathbf{u}^{(i)}}{\rho}\|_2^2, \tag{2.13}$$

$$\mathbf{u}^{(i+1)} = \mathbf{u}^{(i)} + \mathbf{A}\mathbf{x}^{(i+1)} + \mathbf{B}\mathbf{y}^{(i+1)} - \mathbf{c}. \tag{2.14}$$

For a comprehensive understanding of ADMM, the reader is referred to [Boy+11; PB+14].

3 State of the art in multibaseline InSAR

Multibaseline InSAR technologies have been extensively investigated for decades and proposed to retrieve geophysical parameters (namely elevation and deformation parameters) for extended areas. As introduced in the last chapter, there are normally two scattering mechanisms, i.e. PS and DS, of the observed areas, Respectively, PSI and DSI are the associated signal processing techniques for the parameter estimation. Moreover, in regard to the decomposition of multiple phase centers in each resolution cell, SAR tomography techniques are the workhorses for tackling the *layover* problem. The history and state-of-the-art research for those topics are reviewed in this chapter.

3.1 Persistent Scatterer Interferometry

PSI [FPR01; Hoo+04; Weg+10; Wer+03; Kam06] is one of the most powerful techniques for geophysical parameter estimation based on multibaseline SAR images. Based on PSs which are characterized by geometrically and temporally stable phase response, PSI effectively overcomes the limitations brought by geometrical and temporal decorrelation on the performance of geophysical parameter estimation in multibaseline InSAR. Typically, for PSs with high signal-to-noise ratio (SNR), e.g. 10dB, millimeter precision on the linear deformation rate estimation can be achieved with around 30 SAR images [FPR01].

3.1.1 Persistent Scatterer candidate identification

As first proposed in [FPR01], pixels are selected as PS candidates according to *amplitude dispersion index* D_a, which can be calculated by the ratio between the temporal standard deviation and mean of the amplitudes. [FPR01] has shown the estimation of the phase stability based on amplitude dispersion maintains very well with high SNR (10dB). Typically, pixels are chosen as PS candidates when D_a is between 0.25 and 0.4 [FPR01; Col+03]. Low spectral phase diversity is exploited as a proxy for PS candidate selection in [Wer+03]. By exploiting the spatial correlation of phase measurements, stanford method for persistent scatterers (StaMPS) [Hoo06] is applicable for selecting PS in areas undergoing non-steady deformation without prior knowledge. Likewise, based on spatial correlation analysis, PS pairs are identified via the construction of PS arc in [Cos+08]. Sublook coherence approached is proposed in [Sch+06] for point-like scatterer identification without the requirement of certain number of temporal SAR images. Other spectral correlation based methods, such as phase variance approach [Gia+08] and generalized likelihood-ratio test (GLRT) approach [SF+15], are investigated for PS candidate selection. Also, the evaluation of such coherent scatterer selection methods is conducted in [WAL18]. By exploring the statistical properties of the eigenvalues of the covariance matrix, a new PS candidate selection approach is introduced in [NKL18].

3.1.2 Parameter estimation

Methods for estimating geophysical parameters such as topography height and linear deformation rates from PS have been extensively studied in recent years. With the assumption that the deterministic signal of PS $\mathbf{g}$ corrupted by CCG noise, maximum likelihood estimator (MLE) of the parameters $\boldsymbol{\theta}$ is [RB74; FPR01; WZ16]:

$$\underset{\boldsymbol{\theta}}{\operatorname{argmax}} \frac{1}{(2\pi\sigma^2)^N} \exp(-\frac{1}{2\sigma^2}\|\mathbf{g}-\tilde{\mathbf{g}}(\boldsymbol{\theta})\|_2^2), \tag{3.1}$$

where $\boldsymbol{\theta}$ represents the unknown geophysical parameters, $\tilde{\mathbf{g}}(\boldsymbol{\theta})$ is the modeled PS signal, N is the number of interferograms and σ^2 denotes the variance of complex noise. Equation (3.1) can also be rewritten as:

$$\underset{\boldsymbol{\theta}}{\operatorname{argmax}} |\frac{1}{N}\sum_{n=1}^{N} g_n \exp(-j\varphi_n(\boldsymbol{\theta}))|, \tag{3.2}$$

which is well-known as *temporal coherence* [FPR01]. In order to describe the precision of the estimated parameters, least squares ambiguity decorrelation (LAMBDA), which is originally developed for the ambiguity resolution of GPS signal, is adapted to parameter estimation for PS signals in [KH04]. To improve the robustness of MLE, *M-estimator* is proposed in [WZ16]. Rather than equally treating each temporal observation in Equation (3.1), weighted functions are exploited in M-estimator to downweight the observations corrupted by outliers or unmodeled phases. In order to take advantages of large number of useful SAR acquisitions and avoid spatial decorrelation, small baseline subset (SBAS) algorithm has been proposed for deformation retrieval in [Ber+02]. For the estimation of non-steady deformation with no prior knowledge, [Hoo06] first isolates wrapped deformation signals in PSs and proposes a 3D phase unwrapping method for retrieving their real phases. Based on building arc networks with no phase ambiguities and least squares estimator, a PS time series modeling method without phase unwrapping for deformation rate estimation is proposed in [ZDL11]. Recently, a review of different PSI techniques is given in [Cro+16].

3.2 Distributed Scatterer Interferometry

In order to extract geophysical information from non-urban areas with DS, interferometry techniques for parameter estimation from such stochastic signals have been extensively carried out in decades. Normally, SHP selection for covariance matrix estimation and optimal phase history retrieval from such covariance matrices are the two key steps in DS interferometry.

3.2.1 Statistically Homogeneous Pixels selection

For extracting optimal phase histories from sample covariance matrices, SHP should be selected first. Normally those pixels sharing the same statistical behavior are selected based on their amplitudes. As introduced in [Fer+11], SqueeSAR exploits KS test [Ste70] for selecting SHP with the assumption that the statistics of amplitude data can be seen as a proxy for phase stability [FPR01]. Besides, Anderson–Darling (AD) test can be explored as another option for

effectively selecting SHP in [WZB12; GA12; GA14]. Composed of KS, AD, Kullback–Leibler divergence and GLRT, different amplitude-based methods for selecting SHP are evaluated in [PB11]. Among those, AD has been proved to be the most effective statistical test for selecting two pixels with the same distribution. To overcome the drawback of SHP selection in non-Gaussian SAR scenes and the biased estimation of sample covariance, a hybrid framework is proposed in [JDL14]. For non-urban areas without man-made structures, the spatial and temporal variation of the amplitudes returned from scatterers may induce problems for amplitude-based methods. By directly investigating phase information, [CLJ16] utilizes coherence matrices to examine whether the corresponding two pixels are from the same distribution. GLRT for coherence matrices is exploited as a criteria for the GLRT identification. In a similar vein, such criteria is also deployed for nonlocal self-similarity (NSS) to select homogeneous patches and covariance matrix estimation [Del+15].

3.2.2 Single-master phase history retrieval

Estimating optimal phase histories from covariance matrices built by the selected SHP is the second key step in DSI. The construction of covariance matrices can be considered as the generation of multimaster (MM) interferograms. In order to link all the available interferometric phases, optimal phase histories, i.e. single-master (SM) phases, are then estimated from such covariance matrices. It is also well-known as *phase linking* [GT08] or *phase triangulation* [Fer+11], where iterative algorithms are proposed for solving the following problem based on MLE:

$$\underset{\boldsymbol{\varphi}}{\operatorname{argmin}} \boldsymbol{\xi}^H (|\hat{\boldsymbol{\Gamma}}|^{-1} \odot \hat{\boldsymbol{\Gamma}}) \boldsymbol{\xi}, \tag{3.3}$$

where $\boldsymbol{\xi} = \exp(j\boldsymbol{\varphi})$, $\hat{\boldsymbol{\Gamma}}$ denotes the sample coherence matrix obtained from SHP, $|\cdot|$ is the absolute operator and $\odot$ denotes the Hadamard operator.

The approximate solution of such nonlinear optimization problem can also be obtained by the eigenvalue decomposition of sample covariance matrix $\hat{\mathbf{C}}$ [For+15] or $\hat{\boldsymbol{\Gamma}}$ [CLJ16]. Moreover, multiple scattering mechanisms of DS can be separately analyzed by such method. In a mathematical point of view, several phase linking methods are analyzed in [CLJ15]. Although SBAS [Ber+02] has not exploited the full information of all the possible MM interferograms, it can also be considered as a phase linking method for DS processing based on small-baseline subsets. SM phase histories are then estimated based on least squares estimator. To improve the robustness of SBAS in cases of outliers and unwrapping phase errors, minimum L_1 norm criterion is investigated in the inversion of parameters of interest [GA12]. As an extension of LAMBDA from PS to DS, an integer least squares (ILS) based method is proposed in [SE+16]. By formulating a system of linear observation equations with the full exploitation of covariance matrices, it is capable of the uncertainty study from the observations propagated to the final estimates. For the DS characteristics deviate from the CCG, *M-estimator* is applied to estimate the SM phase histories [WZ16]. Targeting at InSAR time series processing for big data in real time, an efficient algorithm containing key steps of signal subspace estimation and the generation of artificial interferograms [DZLD11], i.e. data compression, is introduced in [ADZB17]. As a follow-on, an improved phase linking method which takes advantages of

eigenvalue decomposition and MLE is proposed in [ADZB18]. Its key idea is the introduction of extra weights in Equation (3.3), in cases of erroneous coherence matrix estimation.

Commonly, based on the methods of phase linking, SM phase histories can be estimated from time series of SAR data, the corresponding geophysical parameters, such as residual topography height and linear deformation rate, can then be reconstructed in a similar processing chain of PS signals.

3.3 SAR Tomography

Even though PSI and DSI techniques can provide the additional information along the elevation dimension, a single scatterer or a single phase center in each resolution cell is usually prerequisite. In cases of *layover*, i.e. multiple scatterers at different elevations superimposed in the same resolution cell, those techniques cannot be sufficient for reconstructing the real 3D structure of the scene, especially in urban areas with dense buildings. SAR Tomography (TomoSAR) technique has been proposed for alleviating those limitations by synthesizing an aperture in the elevation dimension with the multiple acquisitions of SAR images obtained of the same scene. The signal of nth SAR image can be mathematically modeled as [RM00; FSS03; ZB10b; For+14]:

$$g_n = \int_{I_s} \gamma(s) \exp(-j \frac{4\pi B_{\perp_n}}{\lambda R} s) ds, \tag{3.4}$$

where I_s is the elevation support and $\gamma(s)$ denotes the complex reflectivity profile along the elevation dimension (s).

3.3.1 Tomographic inversion

In a more compact form, Equation (3.4) can be rewritten as the linear system [FSS03; ZB10b; For+14]:

$$\mathbf{g} = \mathbf{R}_s \boldsymbol{\gamma}, \tag{3.5}$$

where $\mathbf{R}_s$ is the predesigned discrete Fourier matrix with respect to elevation s. Considering deformation parameter into the tomographic inversion, $\mathbf{R}_s$ should be generalized into $\mathbf{R}_{s,t}$, which is the 2D Fourier basis support of elevation s and time t. Such inversion problem is well-known as Differential SAR Tomography (D-TomoSAR) [Lom05; FRS09]. The linear inverse problem of Equation (3.5) can be solved by analyzing singular value decomposition (SVD) on $\mathbf{R}_s$ and mitigating noise level by restricting the solution space to the subspace spanned by the orthogonal vectors with large singular values [FSS03]. By assuming the uniform distribution of baselines, the tomographic inversion can be viewed as directions of arrival (DOA) estimation problem and several spectral estimation methods, such as Capon, amplitude and phase estimation filter (APES) and multiple signal classification (MUSIC), are analyzed in [LMG03; GL05]. As the extension, multilook modern parametric relaxation spectral estimator (RELAX) and APES algorithms are furthermore investigated for cases of DS. More comprehensive discussion of spectral estimation methods can be found in [SM+05] and a review of spectral estimation methods applied in TomoSAR is presented in [GLM02]. Benefiting from the high-resolution SAR systems, e.g. TerraSAR-X [WB10] and COSMO-SkyMed

[Cal+14], a detailed study of tomographic capability of TerraSAR-X spotlight mode is demonstrated in [ZB10b]. Besides, with Wiener-type regularization, a maximum *a posteriori* (MAP) estimator is proposed and several model order selection methods for estimating the number of scatterers have been compared. Compared to the range (0.6m in TerraSAR-X spotlight mode) and azimuth (1m) [Ein+09], the resolution of elevation direction is at least an order of magnitude lower and it is limited by Rayleigh resolution [ZB10b; ZB14]:

$$\rho_s = \frac{\lambda R}{\Delta B_\perp}, \tag{3.6}$$

where $\Delta B_\perp$ is the perpendicular baseline range or elevation aperture length. By utilizing compressive sensing (CS) theory [Bar07; Don06], two or more scatterers within the Rayleigh resolution can be separated, which makes it invaluable for TomoSAR reconstruction in urban areas [ZB10a; BES11]. In [ZGS15b], exploiting OSM building footprints as prior knowledge of pixels sharing similar heights into frameworks based on joint sparse reconstruction techniques, a highly accurate tomographic reconstruction can be achieved using just six interferograms. Aiming at decreasing the computational cost of normal CS based tomography methods, a randomized blockwise proximal gradient has been developed for the practical use in large-scale 3D point cloud generation in urban areas [Shi+18]. Via the combination of TomoSAR and PSI, the performance of deformation retrieval in layover-affected areas can be improved [Sid+16], since the phase contributions of multiple scatterers may influence the deformation estimation in the normal PS processing. Taking advantage of staring spotlight mode, [Ge+18] demonstrates the density and accuracy improvement of 3D TomoSAR point cloud generation compared with the conventional sliding spotlight mode of TerraSAR-X.

Most of the above-mentioned techniques are tailored for recovering the elevation profiles with the assumption that the illuminated scene is constituted by PS. In cases of DS, e.g. forest areas, SAR tomography problem is formulated and discussed in [Teb10] with single and multipolarimetric SAR observations. With parametric and nonparametric spectral estimation methods, [SZ16a] demonstrates the performance of 3D reconstruction in forest areas based on millimeterwave (Ka-band) SAR system. Covariance matrix estimation plays an essential role in tomogram reconstruction from DS, [DHo+18] has proposed a novel estimation method based on the spatial and radiometric similarities of nonlocal patches measured with Riemannian distances [DGH13] and several performance metrics have been analyzed for the evaluation of 3D TomoSAR point cloud generation.

3.4 Contributions of this thesis

Although some of the above-mentioned techniques do exploit information from multiple neighboring pixels or patches, the natural semantic and geometric information in SAR images has not been explicitly employed. Such geometric information can be the object mask of a building façade where the height and deformation obey certain prior knowledge, such as continuity and smoothness. Introducing them into the retrieval of phase history parameters can be of great advantage, for example, to improve the accuracy of the estimates, or to reduce the number of images required to obtain a reliable estimation.

In a summary, this thesis makes the following contributions to the field of multibaseline InSAR.

- Extended the multibaseline InSAR signal model of single pixel to an object-level by means of a tensor representation. By exploiting the prior knowledge of the deformation pattern of objects, an object-based InSAR parameter inversion technique is proposed and the optimization procedure based on ADMM is introduced.
- Given object areas, e.g. façades, bridges and roofs, an InSAR phase stack can be represented by a 3-mode tensor and its multidimensional low-rank property is first investigated in this thesis. Based on such property, robust low rank tensor decomposition methods, e.g. Robust Mutibaseline InSAR technique via Object-based low rank tensor decomposition (RoMIO), are proposed in this thesis, which can efficiently improve the accuracy of geophysical parameters estimated via conventional multibaseline InSAR techniques, e.g. PSI. Furthermore, proper regularization terms, e.g. TV, can be also integrated into the tensor decomposition model, which can both mitigate outliers and complex Gaussian noise in real dataset.
- As the extension of robust low rank tensor decomposition method for DS processing, the corresponding framework is proposed in this thesis, based on the low-rank property inherent in the multi-looked DS pixels. With a limited number of SAR interferograms (around six), the proposed method demonstrates the reliable performance of geophysical parameter reconstruction on a TanDEM-X bistatic InSAR stack of a mountainous area.

4 Object-based multibaseline InSAR geophysical parameter estimation

Past research mostly focused on the optimal retrieval of geophysical parameters on the basis of a single pixel or a pixel cluster. Only until recently, the first demonstration of object-based urban infrastructure monitoring by fusing InSAR and the semantic classification labels derived from optical images was presented by [Wan+17]. Given such classification labels in the SAR images, a general framework for object-based InSAR parameter retrieval, where the parameters of the whole object are jointly estimated by the inversion of a regularized tensor model instead of pixelwise. In this chapter, single-pixel multibaseline InSAR signal model is first recapped in Section 4.1. Based on that, the tensor representation of InSAR signal model for objects is introduced in Section 4.2. Then, the proposed object-based multibaseline InSAR inversion is presented in Section 4.3. In Section 4.4, a robust filter is demonstrated for outlier removal for real InSAR dataset. In order to obtain the semantic masks in SAR images, SARptical processing [Wan+17] is demonstrated in Section 4.5.1 and the case study of deformation retrieval is illustrated in Section 4.6. A short discussion for the proposed method is demonstrated in Section 4.7. Most materials in this chapter have been published in [Kan+17].

4.1 Single-pixel multibaseline InSAR signal model

The interferometric phase history of a PS in a multibaseline InSAR stack is determined by the elevation (topography) of the scatter, as well as its deformation over the observed period. Correspondingly, a PS signal $\mathbf{g}(s,p)$ can be modeled as follows:

$$\bar{\mathbf{g}}(s,p) = a\exp\{-j(\frac{4\pi}{\lambda r}s\times\mathbf{b}+\frac{4\pi}{\lambda}p\times\boldsymbol{\tau})\}, \tag{4.1}$$

where a is the modeled amplitude of the PS, $\mathbf{b}$ is the vector of the spatial baseline, $\boldsymbol{\tau}$ is the vector of the deformation model, e.g. $\boldsymbol{\tau}=\mathbf{t}_{tp}$ for linear motion, and $\boldsymbol{\tau}=\sin(2\pi(\mathbf{t}_{tp}-t_0))$ for the seasonal motion model with the temporal baseline $\mathbf{t}_{tp}$, s and p are the unknown elevation and deformation parameters to be estimated, respectively, λ is the wavelength of the radar transmitted signals and r denotes the range between radar and the observed object.

As introduced in Equation (3.1), the MLE of the parameters s and p can be formulated as solving the following problem:

$$\underset{s,p}{\operatorname{argmin}}\,\|\mathbf{g}-\bar{\mathbf{g}}(s,p)\|_2^2, \tag{4.2}$$

which is equivalent to the periodogram [DMFP09; RB74; WZ16],

$$\underset{s,p}{\operatorname{argmax}}\,|\bar{\mathbf{g}}(s,p)^H\mathbf{g}|. \tag{4.3}$$

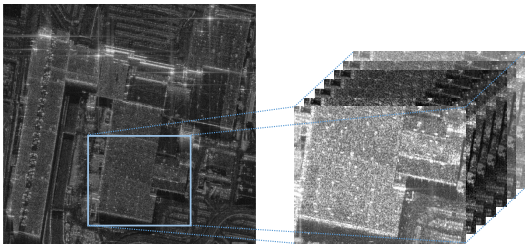

Figure 4.1: InSAR phase tensor example of TerraSAR-X data with a roof area (blue rectangular) of Las Vegas Convention Center.

where $\mathbf{g}$ is the input-observed PS phase vector. Since the complex phase of PSs is mainly focused on, the amplitude is ignored in the following content.

4.2 Tensor extension of multibaseline InSAR signal model

Given an object area, e.g. roof, as illustrated in Figure 4.1, its interferometric phase stack can be represented as a 3-mode tensor $\mathcal{G} \in \mathbb{C}^{I_1 \times I_2 \times I_3}$, where I_1, I_2 represent the spatial dimension in range and azimuth, respectively, and I_3 denotes the number of SAR interferograms. Similar to equation Equation (4.1), its tensor extension (amplitude dropped) can be expressed as follows:

$$\bar{\mathcal{G}}(\mathbf{S},\mathbf{P}) = \exp\{-j(\frac{4\pi}{\lambda r}\mathbf{S}\otimes\mathbf{b} + \frac{4\pi}{\lambda}\mathbf{P}\otimes\boldsymbol{\tau})\}. \tag{4.4}$$

Here, $\overline{\mathcal{G}}$ is the modeled complex phase tensor of the object, $\mathbf{S}$ and $\mathbf{P}$ represent the matrices of elevation and deformation to be estimated, respectively. The symbol $\otimes$ denotes the outer product, which plays a role in the dimension extension [Cic+15].

4.3 Object-based multibaseline InSAR inversion

Given the observed complex phase tensor $\mathcal{G}$ of a certain object, the goal is to jointly reconstruct all the parameters. In the proposed method, the prior knowledge of the spatial patterns of such geophysical parameters is exploited. To this end, the optimization problem of equation Equation (4.2) is extended to the following expression:

$$\underset{\mathbf{S},\mathbf{P}}{\operatorname{argmin}}\, \alpha\|\mathcal{G} - \bar{\mathcal{G}}(\mathbf{S},\mathbf{P})\|_F^2 + \mu f(\mathbf{S},\mathbf{P}). \tag{4.5}$$

The first term is the data fidelity term, which calculates the Frobenius norm of the log likelihood between the observed tensor $\mathcal{G}$ and the modeled tensor $\overline{\mathcal{G}}$. $f(\mathbf{S},\mathbf{P})$ denotes the penalty term which represents the spatial prior of $\mathbf{S}$ and $\mathbf{P}$. The regularization parameter μ controls the balance between these two terms. Therefore, Equation (4.5) can be considered as the MAP estimator of $\mathbf{S}$ and $\mathbf{P}$.

4.3.1 Object-based multibaseline InSAR inversion with total variation regularization

One popular smoothness prior is the TV norm, which is widely used in multiple image processing problems, e.g. image deblurring, denoising and inpainting [ZC08; TYH09; CP11], and is also applied for interferometric phase denoising [Den+09; SDT11]. Specifically, TV penalizes the perturbations of signal u by limiting its gradient:

$$\mathrm{TV}(u) = \int_{\Omega} |\nabla u| \mathrm{d}x. \tag{4.6}$$

In such case, with the smoothness assumption of deformation pattern, Equation (4.5) can be rewritten as:

$$\underset{\mathbf{S},\mathbf{P}}{\operatorname{argmin}} \alpha \|\mathscr{G} - \bar{\mathscr{G}}(\mathbf{S},\mathbf{P})\|_F^2 + \mu \|\mathbf{P}\|_{TV}, \tag{4.7}$$

where $\|\mathbf{X}\|_{TV}$ denotes the TV norm with the definition as $\|\mathbf{X}\|_{TV} := \sum_{i_1,i_2} |x_{i_1,i_2} - x_{i_1-1,i_2}| + |x_{i_1,i_2} - x_{i_1,i_2-1}|$. Such optimization problem can be solved with ADMM framework. In doing so, auxiliary variables are introduced and Equation (4.7) can be rewritten as:

$$\underset{\mathbf{S},\mathbf{P}}{\operatorname{argmin}} \alpha \|\mathscr{G} - \bar{\mathscr{G}}(\mathbf{S},\mathbf{Z})\|_F^2 + \mu \|\mathbf{F}\|_1, \quad s.t.\ D(\mathbf{P}) = \mathbf{F},\ \mathbf{P} = \mathbf{Z}, \tag{4.8}$$

where $D(\cdot)$ is the first-order difference operator. The corresponding constraint optimization problem can be converted into an augmented Lagrangian function, yielding

$$\begin{aligned} L(\mathbf{S},\mathbf{P},\mathbf{F},\mathbf{Z},\mathbf{\Gamma}_1,\mathbf{\Gamma}_2) =& \alpha \|\mathscr{G} - \exp\{-j(\frac{4\pi}{\lambda r}\mathbf{S}\otimes\mathbf{b} + \frac{4\pi}{\lambda}\mathbf{Z}\otimes\boldsymbol{\tau})\}\|_F^2 + \mu\|\mathbf{F}\|_1 + \\ & \langle \mathbf{\Gamma}_1, D(\mathbf{P}) - \mathbf{F}\rangle + \langle \mathbf{\Gamma}_2, \mathbf{P} - \mathbf{Z}\rangle + \frac{\rho}{2}(\|D(\mathbf{P}) - \mathbf{F}\|_F^2 + \|\mathbf{P} - \mathbf{Z}\|_F^2), \end{aligned} \tag{4.9}$$

where $\mathbf{\Gamma}_1, \mathbf{\Gamma}_2$ are the introduced dual variables and ρ is the penalty parameter. ADMM takes advantage of splitting one difficult optimization problem into several subproblems, where each of them can be solved easily. Accordingly, the minimization of $L(\mathbf{S},\mathbf{P},\mathbf{F},\mathbf{Z},\mathbf{\Gamma}_1,\mathbf{\Gamma}_2)$ with respect to each variable can be tackled by solving the following subproblems:

1) $\mathbf{S}$ *subproblem*: By fixing the other variables, the subproblem of L with respect to $\mathbf{S}$ is

$$\min_{\mathbf{S}} \alpha \|\mathscr{G} - \exp\{-j(\frac{4\pi}{\lambda r}\mathbf{S}\otimes\mathbf{b} + \frac{4\pi}{\lambda}\mathbf{Z}\otimes\boldsymbol{\tau})\}\|_F^2. \tag{4.10}$$

It can be pixel-wisely solved by exploiting periodogram on each PS phase vector.

2) $\mathbf{P}$ *subproblem*: By fixing the other variables, the subproblem of L with respect to $\mathbf{P}$ is

$$\min_{\mathbf{P}} \langle \mathbf{\Gamma}_1, D(\mathbf{P}) - \mathbf{F}\rangle + \langle \mathbf{\Gamma}_2, \mathbf{P} - \mathbf{Z}\rangle + \frac{\rho}{2}(\|D(\mathbf{P}) - \mathbf{F}\|_F^2 + \|\mathbf{P} - \mathbf{Z}\|_F^2). \tag{4.11}$$

Then, by calculating the gradient of L with respect to $\mathbf{P}$ and setting it as zero, the following linear system is obtained:

$$(\rho\mathbf{I} + \rho D^* D)\mathbf{P} = \rho D^*(\mathbf{F}) + \rho\mathbf{Z} - D^*(\mathbf{\Gamma}_1) - \mathbf{\Gamma}_2, \tag{4.12}$$

where $D^*(\cdot)$ is the adjoint operator of $D(\cdot)$. According to the block-circulant structure of the matrix D^*D, its inverse problem can be efficiently solved by exploiting Fast Fourier Transform (FFT) and its inverse transform [Wan+18; SO14; Ji+16].

3) $\mathbf{F}$ *subproblem*: By fixing the other variables, the subproblem of L with respect to $\mathbf{F}$ is:

$$\min_{\mathbf{F}} \mu\|\mathbf{F}\|_1 + \frac{\rho}{2}\|\mathbf{F} - D(\mathbf{P}) - \frac{\mathbf{\Gamma}_1}{\rho}\|_F^2. \tag{4.13}$$

This L_1-norm-induced subproblem can be efficiently solved by applying the soft-thresholding operator defined by $\mathscr{S}_\gamma(\mathbf{A}) := \text{sign}(\mathbf{A}) \odot \max(|\mathbf{A}| - \gamma, 0)$, where $|\mathbf{A}| = \text{sign}(\mathbf{A}) \odot \mathbf{A}$.

4) $\mathbf{Z}$ *subproblem*: By fixing the other variables, the subproblem of L with respect to $\mathbf{Z}$ is:

$$\min_{\mathbf{Z}} \alpha\|\mathscr{G} - \exp\{-j(\frac{4\pi}{\lambda r}\mathbf{S}\otimes\mathbf{b} + \frac{4\pi}{\lambda}\mathbf{Z}\otimes\boldsymbol{\tau})\}\|_F^2 + \frac{\rho}{2}\|\mathbf{Z} - \mathbf{P} + \frac{\mathbf{\Gamma}_2}{\rho}\|_F^2. \tag{4.14}$$

Such unconstrained nonlinear optimization problem can be solved by Quasi-Newton method [Zhu+97; Byr+95]. Note that global optimization can not be guaranteed to achieve with any choice of initialization point in the solution space for such nonlinear problem. Initializing the parameters $\mathbf{S}$ and $\mathbf{Z}$ by the estimation results of periodogram is adopted.

5) Multiplier updating: All the dual variables can be updated by:

$$\begin{aligned} \mathbf{\Gamma}_1 &:= \mathbf{\Gamma}_1 + \rho(D(\mathbf{P} - \mathbf{F})), \\ \mathbf{\Gamma}_2 &:= \mathbf{\Gamma}_2 + \rho(\mathbf{P} - \mathbf{Z}). \end{aligned} \tag{4.15}$$

The detailed ADMM pseudocode for solving Equation (4.7) is summarized in Algorithm 1. Using a predefined convergence condition, e.g. 10^{-3}, the solution $\hat{\mathbf{S}}, \hat{\mathbf{P}}$ can be obtained. Note that in the proposed algorithm, for simplicity, spatial prior knowledge is imposed on just deformation matrix $\mathbf{P}$. One can also introduce TV norm on both the parameter matrices and utilize the same optimization strategy as the above.

4.3.1.1 Convergence analysis

Such ADMM-based optimization strategy utilized in Algorithm 1 can be considered as Block Coordinate Descent (BCD), whose convergence is theoretically guaranteed as long as each subproblem is convex [LSG17; WCX15]. In such case, since the subproblems of $\mathbf{S}$ and $\mathbf{Z}$ are not convex, the theoretical convergence cannot be guaranteed. However, the convergence of Algorithm 1 on the simulated data is experimentally analyzed and displayed in Figure 4.2. It can be demonstrated that the convergence of Algorithm 1 can be achieved around 20 iterations.

4.3.1.2 Visualized comparison

A multibaseline InSAR stack with the ground truth spatial linear deformation rate ranging from 1 (mm/y) to 2.5 (mm/y) is simulated, as shown in the left figure of Figure 4.3. The spatial and temporal baselines are comparable to those of TerraSAR-X. The number of interferograms is 30. Uncorrelated complex circular Gaussian noise is added to the simulated stack with an SNR of 5dB.

Algorithm 1 Object-based approach (TV) solved by ADMM

Require: $\mathscr{G}, \mu, \rho, \alpha$

Initialize $\mathbf{S}$, $\mathbf{P}$, $\mathbf{Z}$, $\mathbf{F}$, $\mathbf{\Gamma}_1$, $\mathbf{\Gamma}_2$
for $k = 0$ to maxIter **do**
  Fix other variables to update $\mathbf{S}$ in Equation (4.10) by utilizing periodogram.
  Fix other variables to update $\mathbf{P}$ in Equation (4.11) by calculating $\mathbf{H_P}$ and $\mathbf{T_P}$, where
  $\mathbf{H}_\mathbf{P}^{(k)} = \rho D^*(\mathbf{F}^{(k)}) + \rho \mathbf{Z}^{(k)} - D^*(\mathbf{\Gamma}_1^{(k)}) - \mathbf{\Gamma}_2^{(k)}$,
  $\mathbf{T_P} = |\text{fftn}(\mathbf{D}_h)|^2 + |\text{fftn}(\mathbf{D}_v)|^2$.
  $\mathbf{P}^{(k+1)} \leftarrow \text{ifftn}(\frac{\text{fftn}(\mathbf{H}_\mathbf{P}^{(k)})}{\rho + \rho \mathbf{T_P}})$.
  Fix other variables to update $\mathbf{F}$ in Equation (4.13) by element-wise soft-thresholding,
  $\mathbf{F}^{(k+1)} \leftarrow \mathscr{S}_{\frac{\mu}{\rho}}(D(\mathbf{P}^{(k+1)}) + \frac{\mathbf{\Gamma}_1^{(k)}}{\rho})$.
  Fix other variables to update $\mathbf{Z}$ in Equation (4.14) by utilizing Quasi-Newton method.
  Multiplier update by
  $\mathbf{\Gamma}_1^{(k+1)} \leftarrow \mathbf{\Gamma}_1^{(k)} + \rho(D(\mathbf{P}^{(k+1)}) - \mathbf{F}^{(k+1)})$,
  $\mathbf{\Gamma}_2^{(k+1)} \leftarrow \mathbf{\Gamma}_2^{(k)} + \rho(\mathbf{P}^{(k+1)} - \mathbf{Z}^{(k+1)})$.
  if convergence **then**
    break
  end if
end for

Ensure: $(\hat{\mathbf{S}}, \hat{\mathbf{P}})$

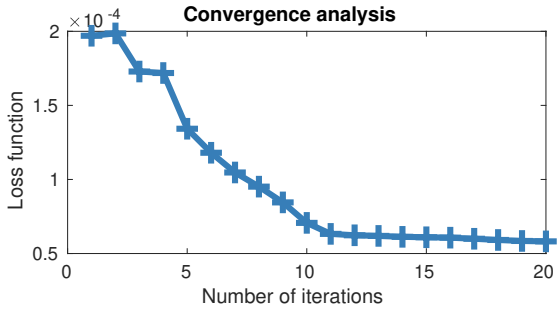

Figure 4.2: The convergence analysis of Algorithm 1 on a simulated data. It can be seen that within 20 iterations, the total loss of the optimization function is converged.

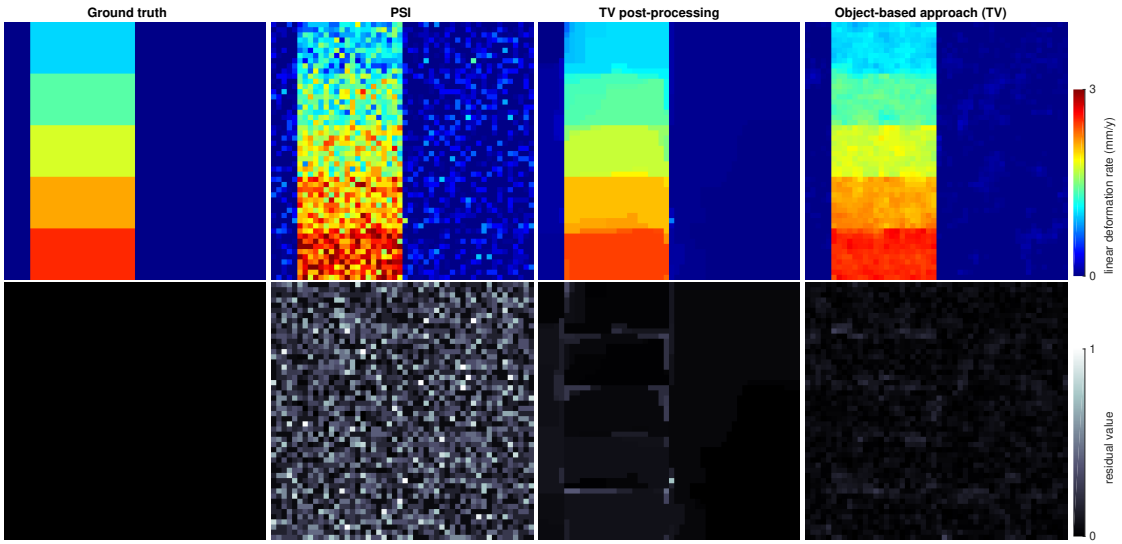

Figure 4.3: Visualized comparison of PSI, the proposed method and the TV post-processing on the estimation of deformation rates of the simulated data. As shown from the results, without considering the prior knowledge of the deformation rates along spatial directions, the result of PSI is much noisier compared to the results of the other two. The spatial pattern of the displacement variation cannot be easily recognized from such result. What is more interesting is the comparison between the proposed method and the TV post-processing approach. The results show that applying TV filtering afterwards can indeed achieve a certain level of denoising. However, over-smoothing phenomenon can be found in the map of residual values. In other words, larger bias is existed in the post-processing result than the proposed joint optimization method, especially around the areas of value jump.

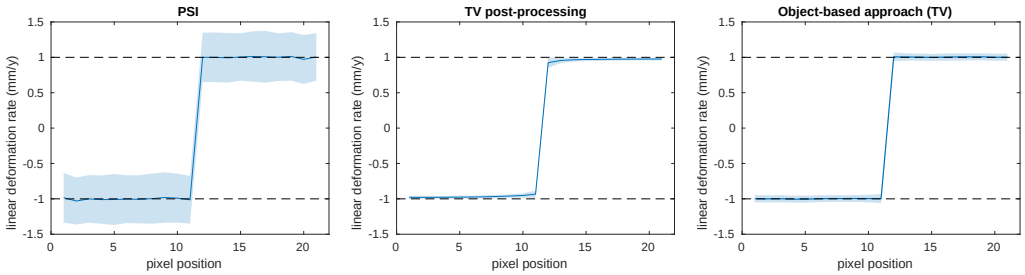

Figure 4.4: The compared methods on the step function approximation. As illustrated in the left subfigure, the expected values of the estimates by MLE employed in PSI can approximate the ground truth well. However, compared to the other two methods, its standard deviation is much larger, since the spatial prior knowledge of parameters is not taken advantage of in the reconstruction of PSI. In contrast, the standard deviations can be very well suppressed in either joint or separate optimization based method. However, consistently with the above analysis, bias can be found in the TV post-processing result, especially in the area of value jump.

The performance is visually compared with those obtained by the pixel-wise periodogram, which is exploited as parameter estimation method in PSI [FPR01], and the post-processing of TV denoising on the result of PSI. One may wonder that there is no big difference between the proposed object-based method and the result achieved by the separate processing of PSI and the associated variational denoising method. The results are displayed in Figure 4.3, where the first row is the estimated linear deformation rates of the comparing methods and the second row is the residual values between those and the ground truth.

As shown from the results, without considering the prior knowledge of the deformation rates along spatial directions, the result of PSI is much noisier compared to the results of the other two. The spatial pattern of the displacement variation cannot be easily recognized from such result. What is more interesting is the comparison between the proposed method and the TV post-processing approach. The results show that applying TV filtering afterwards can indeed achieve a certain level of denoising. However, over-smoothing phenomenon can be found in the map of residual values. In other words, larger bias is existed in the post-processing result than the proposed joint optimization method, especially around the areas of value jump. The plausible reason can be the joint optimization strategy can iteratively take advantage of both the data fidelity and the prior knowledge, given the original observed InSAR stacks. As a comparison, the TV post-processing approach searches the optimal solution given the initialization of the results obtained by PSI. In other words, the solution of the TV post-processing approach is strongly dependent on the results of PSI. When there are unreliable estimates at some points, the biases can be induced in the final result.

4.3.1.3 Step function approximation

In order to indicate how the details can be preserved by the proposed method, the results of 1000 Monte-Carlo simulations are reported in Figure 4.4 based on the experiment of step function approximation [Bai18; Bai18]. An InSAR stack with a linear deformation rate jump

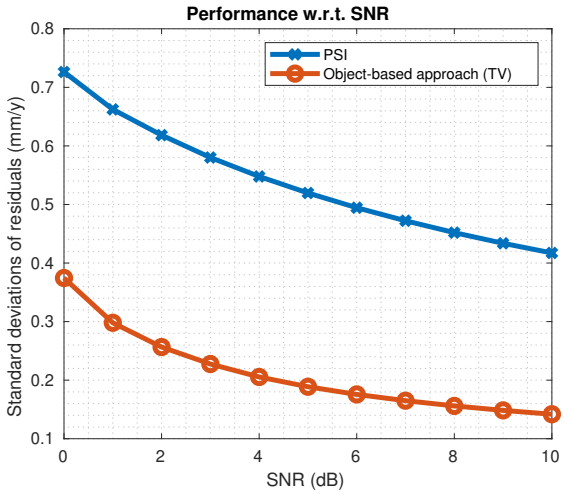

Figure 4.5: The performances of PSI and the proposed method with respect to different SNR on the simulated step function dataset. It can be seen that with the spatial regularization, the object-based method can achieve the performance improvement by a factor of two than PSI.

from −1 (mm/y) to 1 (mm/y) is simulated and SNR is imposed as 5dB. The dashed black lines indicate the ground truth value of linear deformation rates. Expected values of the estimates from the three methods are plotted in blue and the shaded areas denote the ± standard deviations around the expected values.

As illustrated in the left subfigure, the expected values of the estimates by MLE employed in PSI can approximate the ground truth well. However, compared to the other two methods, its standard deviation is much larger, since the spatial prior knowledge of parameters is not taken advantage of in the reconstruction of PSI. In contrast, the standard deviations can be very well suppressed in either joint or separate optimization based method. However, consistently with the above analysis, bias can be found in the TV post-processing result, especially in the area of value jump. Moreover, with respect to different SNRs, the standard deviations of residuals are displayed in Figure 4.5. It can be seen that with the spatial regularization, the object-based method can achieve the performance improvement by a factor of two than PSI.

4.3.1.4 Parameter setting

The two parameters to be tuned in the proposed method are α and μ. Fortunately, one can be set to constant and the other is tuned accordingly. In the experiments, α is set to be $\frac{1}{I_3}$ and tune μ in the range of 1×10^{-3} to 1×10^{-2}. Based on the simulation of step function, the performance of the proposed method under different parameter settings and SNRs is displayed in Figure 4.6. It can be seen that as the SNR increases, the optimal value of μ tends to be decreased, as larger weight should be relatively imposed on the data fidelity term. Moreover, when SNR approximates 10dB (red plot), the performance is slightly influenced by the choice of μ. In other words, high-quality observed dataset can finely guarantee the reliable parameter estimates, so that the reconstruction performance is not sensitive to the regularization

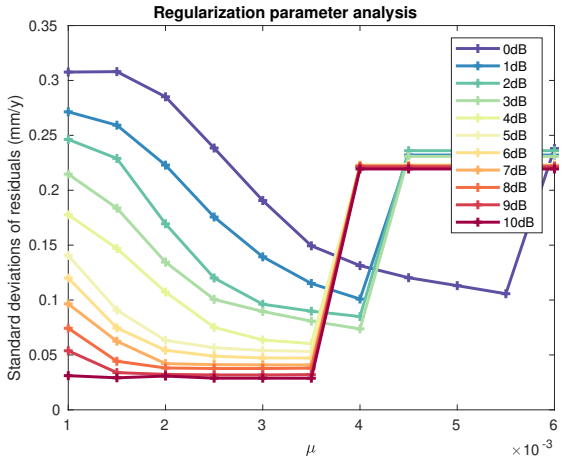

Figure 4.6: The performance of the proposed method under different parameter settings. It can be seen that as the SNR increases, the optimal value of μ tends to be decreased, as larger weight should be relatively imposed on the data fidelity term. Moreover, when SNR approximates 10dB (red plot), the performance is slightly influenced by the choice of μ.

parameter tuning.

4.3.2 Object-based multibaseline InSAR inversion with total generalized variation regularization

TV-based denoising method favors the piece-wise smooth restoration of noisy signals. In order to model the high-order components in the original signals, total generalized variation (TGV) [BKP10; SST11] has been proposed by considering second order derivatives in the regularization term with the following definition:

$$\mathrm{TGV}_{\beta}(u) = \min_{v} \beta_1 \int_{\Omega} |\nabla u - v| \mathrm{d}x + \beta_2 \int_{\Omega} |\nabla u + \nabla v^T| \mathrm{d}x. \tag{4.16}$$

In a discrete form, TGV norm [OY13; SO14] can be written as:

$$\|\mathbf{x}\|_{\mathrm{TGV}}^{\beta_1,\beta_2} := \min_{D(\mathbf{x})=\mathbf{s}+\mathbf{t}} (\beta_1 \|\mathbf{s}\|_{1,2}^{(2,N)} + \beta_2 \|G(\mathbf{t})\|_{1,2}^{(3,N)}), \tag{4.17}$$

where $G(\cdot)$ is the second-order difference operator and $\|\mathbf{s}\|_{1,2}^{(M,N)} = \sum_{k=1}^{N} \sqrt{\sum_{m=0}^{M-1} s_{k+mN}^2}$ is the mixed norm. In a matrix form, the first- and second-order difference operator can be denoted as:

$$D(\cdot) := \begin{bmatrix} \mathbf{D}_h \\ \mathbf{D}_v \end{bmatrix}, \quad G^*(\cdot) := \begin{bmatrix} \mathbf{D}_h & \mathbf{D}_v & \mathbf{0} \\ \mathbf{0} & \mathbf{D}_h & \mathbf{D}_v \end{bmatrix}, \tag{4.18}$$

where $\mathbf{D}_h$ and $\mathbf{D}_v$ are differential filter matrices for horizontal and vertical directions, respectively.

Accordingly, TGV regularized object-based multibaseline InSAR inversion for deformation reconstruction can be defined as:

$$\underset{\mathbf{S},\mathbf{P}}{\operatorname{argmin}} \alpha \|\mathcal{G} - \bar{\mathcal{G}}(\mathbf{S},\mathbf{P})\|_F^2 + \mu \|\mathbf{P}\|_{\mathrm{TGV}}. \tag{4.19}$$

In this subsection, the proposed ADMM optimization strategy for solving Equation (4.19) based on multivariable linear system [SO14] is briefly introduced. One experimental result is carried out and demonstrated in order to address the superiority compared with TV regularization.

To this end, by introducing auxiliary variables, Equation (4.19) can be rewritten as:

$$\underset{\mathbf{S},\mathbf{P}}{\operatorname{argmin}}\, \alpha\|\mathscr{G}-\bar{\mathscr{G}}(\mathbf{S},\mathbf{Z})\|_F^2+\beta_1\|\mathbf{y}_1\|_{1,2}^{(2,N)}+\beta_2\|\mathbf{y}_2\|_{1,2}^{(3,N)} \quad s.t.\ \mathbf{y}_1=D(\mathbf{P})-\mathbf{t},\ \mathbf{y}_2=G(\mathbf{t}),\ \mathbf{P}=\mathbf{Z}. \tag{4.20}$$

The corresponding augmented Lagrangian function is formulated as:

$$\begin{aligned} L(\mathbf{S},\mathbf{P},\mathbf{Z},\mathbf{y}_1,\mathbf{y}_2,\mathbf{t},\mathbf{\Gamma}_1,\mathbf{\Gamma}_2,\mathbf{\Gamma}_3) =& \alpha\|\mathscr{G}-\exp\{-j(\frac{4\pi}{\lambda r}\mathbf{S}\otimes\mathbf{b}+\frac{4\pi}{\lambda}\mathbf{Z}\otimes\boldsymbol{\tau})\}\|_F^2+\beta_1\|\mathbf{y}_1\|_{1,2}^{(2,N)}+\beta_2\|\mathbf{y}_2\|_{1,2}^{(3,N)}+\\ & \langle\mathbf{\Gamma}_1,D(\mathbf{P})-\mathbf{t}-\mathbf{y}_1\rangle+\langle\mathbf{\Gamma}_2,G(\mathbf{t})-\mathbf{y}_2\rangle+\langle\mathbf{\Gamma}_3,\mathbf{Z}-\mathbf{P}\rangle+\\ & \frac{\rho}{2}(\|D(\mathbf{P})-\mathbf{y}_1-\mathbf{t}\|_2^2+\|G(\mathbf{t})-\mathbf{y}_2\|_2^2+\|\mathbf{Z}-\mathbf{P}\|_F^2). \end{aligned} \tag{4.21}$$

By adopting ADMM optimization strategy, the subproblems with respect to each variable are described as:

1) $\mathbf{S}$ *subproblem*: By fixing the other variables, the subproblem of L with respect to $\mathbf{S}$ is

$$\min_{\mathbf{S}}\alpha\|\mathscr{G}-\exp\{-j(\frac{4\pi}{\lambda r}\mathbf{S}\otimes\mathbf{b}+\frac{4\pi}{\lambda}\mathbf{Z}\otimes\boldsymbol{\tau})\}\|_F^2. \tag{4.22}$$

Periodogram can be adopted to solve this problem.

2) $\mathbf{P},\mathbf{t}$ *subproblem*: By fixing the other variables, the subproblem of L with respect to $\mathbf{P}$ and $\mathbf{t}$ is

$$\min_{\mathbf{P},\mathbf{t}}\frac{\rho}{2}(\|D(\mathbf{P})-\mathbf{y}_1-\mathbf{t}+\frac{\mathbf{\Gamma}_1}{\rho}\|_2^2+\|G(\mathbf{t})-\mathbf{y}_2+\frac{\mathbf{\Gamma}_2}{\rho}\|_2^2+\|\mathbf{Z}-\mathbf{P}+\frac{\mathbf{\Gamma}_3}{\rho}\|_F^2). \tag{4.23}$$

By utilizing Karush–Kuhn–Tucker (KKT) condition, this least square problem can be first rewritten as the following multivariable linear system:

$$\begin{bmatrix}\rho\mathbf{I}+\rho D^*D & -\rho D^*\\ -\rho D & \rho\mathbf{I}+\rho G^*G\end{bmatrix}\begin{bmatrix}\mathbf{P}\\ \mathbf{t}\end{bmatrix}=\begin{bmatrix}\rho\mathbf{Z}+\rho D^*(\mathbf{y}_1-\frac{\mathbf{\Gamma}_1}{\rho})+\mathbf{\Gamma}_3\\ -\rho(\mathbf{y}_1-\frac{\mathbf{\Gamma}_1}{\rho})+\rho G^*(\mathbf{y}_2-\mathbf{\Gamma}_2)\end{bmatrix}, \tag{4.24}$$

where

$$D^*D=\mathbf{D}_h^T\mathbf{D}_h+\mathbf{D}_v^T\mathbf{D}_v=\mathbf{\Delta},\quad G^*G=\begin{bmatrix}\mathbf{\Delta} & \mathbf{D}_v\mathbf{D}_h^T\\ \mathbf{D}_h\mathbf{D}_v^T & \mathbf{\Delta}\end{bmatrix}. \tag{4.25}$$

To conveniently manipulate the above system, other variables can be separated accordingly as:

$$\mathbf{t}:=\begin{bmatrix}\mathbf{t}_h\\ \mathbf{t}_v\end{bmatrix},\quad \mathbf{y}_1:=\begin{bmatrix}\mathbf{y}_{1h}\\ \mathbf{y}_{1v}\end{bmatrix},\quad \mathbf{\Gamma}_1:=\begin{bmatrix}\mathbf{\Gamma}_{1h}\\ \mathbf{\Gamma}_{1v}\end{bmatrix},\quad \mathbf{y}_2:=\begin{bmatrix}\mathbf{y}_{2h}\\ \mathbf{y}_{2d}\\ \mathbf{y}_{2v}\end{bmatrix},\quad \mathbf{\Gamma}_2:=\begin{bmatrix}\mathbf{\Gamma}_{2h}\\ \mathbf{\Gamma}_{2d}\\ \mathbf{\Gamma}_{2v}\end{bmatrix}. \tag{4.26}$$

Then, the final multivariable linear system is formulated:

$$\begin{bmatrix} \rho\mathbf{I}+\rho\boldsymbol{\Delta} & -\rho\mathbf{D}_h^T & -\rho\mathbf{D}_v^T \\ -\rho\mathbf{D}_h & \rho\mathbf{I}+\rho\boldsymbol{\Delta} & \rho\mathbf{D}_v\mathbf{D}_h^T \\ -\rho\mathbf{D}_v & \rho\mathbf{D}_h\mathbf{D}_v^T & \rho\mathbf{I}+\rho\boldsymbol{\Delta} \end{bmatrix} \begin{bmatrix} \mathbf{P} \\ \mathbf{t}_h \\ \mathbf{t}_v \end{bmatrix} = \begin{bmatrix} \rho\mathbf{Z}+\rho\mathbf{D}_h^T(\mathbf{y}_{1h}-\frac{\boldsymbol{\Gamma}_{1h}}{\rho})+\rho\mathbf{D}_v^T(\mathbf{y}_{1v}-\frac{\boldsymbol{\Gamma}_{1v}}{\rho})+\boldsymbol{\Gamma}_3 \\ -\rho(\mathbf{y}_{1h}-\frac{\boldsymbol{\Gamma}_{1h}}{\rho})+\rho\mathbf{D}_h(\mathbf{y}_{2h}-\frac{\boldsymbol{\Gamma}_{2h}}{\rho})+\rho\mathbf{D}_v(\mathbf{y}_{2d}-\frac{\boldsymbol{\Gamma}_{2d}}{\rho}) \\ -\rho(\mathbf{y}_{1v}-\frac{\boldsymbol{\Gamma}_{1v}}{\rho})+\rho\mathbf{D}_h(\mathbf{y}_{2d}-\frac{\boldsymbol{\Gamma}_{2d}}{\rho})+\rho\mathbf{D}_v(\mathbf{y}_{2v}-\frac{\boldsymbol{\Gamma}_{2v}}{\rho}) \end{bmatrix}. \tag{4.27}$$

It can be efficiently solved by adjugate method in the frequency domain [SO14].

3) $\mathbf{Z}$ *subproblem*: By fixing the other variables, the subproblem of L with respect to $\mathbf{Z}$ is:

$$\min_{\mathbf{Z}} \alpha\|\mathcal{G}-\exp\{-j(\frac{4\pi}{\lambda r}\mathbf{S}\otimes\mathbf{b}+\frac{4\pi}{\lambda}\mathbf{Z}\otimes\boldsymbol{\tau})\}\|_F^2+\frac{\rho}{2}\|\mathbf{Z}-\mathbf{P}+\frac{\boldsymbol{\Gamma}_3}{\rho}\|_F^2. \tag{4.28}$$

Similarly with Algorithm 1, Quasi-Newton method [1] is employed to solve this problem.

4) $\mathbf{y}_1,\mathbf{y}_2$ *subproblem*: By fixing the other variables, the subproblem of L with respect to $\mathbf{y}_1,\mathbf{y}_2$ is:

$$\begin{aligned} &\min_{\mathbf{y}_1} \beta_1\|\mathbf{y}_1\|_{1,2}^{(2,N)}+\frac{\rho}{2}\|D(\mathbf{P})-\mathbf{y}_1-\mathbf{t}+\frac{\boldsymbol{\Gamma}_1}{\rho}\|_2^2, \\ &\min_{\mathbf{y}_2} \beta_2\|\mathbf{y}_2\|_{1,2}^{(3,N)}+\frac{\rho}{2}\|G(\mathbf{t})-\mathbf{y}_2+\frac{\boldsymbol{\Gamma}_2}{\rho}\|_2^2. \end{aligned} \tag{4.29}$$

Such problems can be solved by applying soft-thresholding operator defined by:

$$\mathcal{S}_\gamma(\mathbf{a})_k := a_k \max\{1-\gamma(\sum_{m=0}^{M-1} a_{k+mN}^2)^{-\frac{1}{2}},0\}. \tag{4.30}$$

6) Multiplier updating: All the dual variables can be updated by:

$$\begin{aligned} \boldsymbol{\Gamma}_1 &:= \boldsymbol{\Gamma}_1+\rho(D(\mathbf{P})-\mathbf{t}-\mathbf{y}_1), \\ \boldsymbol{\Gamma}_2 &:= \boldsymbol{\Gamma}_2+\rho(G(\mathbf{t})-\mathbf{y}_2), \\ \boldsymbol{\Gamma}_3 &:= \boldsymbol{\Gamma}_3+\rho(\mathbf{Z}-\mathbf{P}). \end{aligned} \tag{4.31}$$

The detailed ADMM pseudocode for solving Equation (4.19) is summarized in Algorithm 2.

In order to clarify high-order components of the original signals can be preserved by TGV, the results of 1000 Monte-Carlo simulations are reported in Figure 4.7 based on the experiment of sine function approximation. An InSAR stack with a linear deformation rate from −1 (mm/y) to 1 (mm/y) is simulated and SNR is imposed as 5dB. The dashed black lines indicate the ground truth value of linear deformation rates. Expected values of the estimates from the two methods are plotted in blue and the shaded areas denote the ± standard deviations around the expected values.

It can be clearly seen that object-based approach with TGV can better approximate the nonlinear function than TV. When comes to the high-order variation, e.g. around the trough and crest areas of the sine function, bias is existed in the result based on TV regularization, which does not happen in the result of TGV regularization. The proposed TGV based approach can be considered as the complementary method to the last one. In the experiments of real dataset, object-based approach with TV can achieve decent performance in most cases.

[1] https://de.mathworks.com/help/optim/ug/unconstrained-nonlinear-optimization-algorithms.html

Algorithm 2 Object-based approach (TGV) solved by ADMM

Require: $\mathcal{G}, \rho, \alpha, \beta_1, \beta_2$

1: Initialize $\mathbf{S}$, $\mathbf{P}$, $\mathbf{Z}$, $\mathbf{y}_1$, $\mathbf{y}_2$, $\mathbf{\Gamma}_1$, $\mathbf{\Gamma}_2$, $\mathbf{\Gamma}_3$
2: **for** $k = 0$ to maxIter **do**
3: Fix other variables to update $\mathbf{S}$ in Equation (4.22) by utilizing periodogram.
4: Fix other variables to update $\mathbf{P}$ and $\mathbf{t}$ in Equation (4.22) by solving the problem of Equation (4.27) in Fourier domain.
5: Fix other variables to update $\mathbf{Z}$ in Equation (4.28) by utilizing Quasi-Newton method.
6: Fix other variables to update $\mathbf{y}_1$ and $\mathbf{y}_2$ by element-wise soft-thresholding,

$$\mathbf{y}_1^{(k+1)} \leftarrow \mathscr{S}_{\frac{\beta_1}{\rho}}(D(\mathbf{P}^{(k+1)}) - \mathbf{t}^{(k+1)} + \frac{\mathbf{\Gamma}_1^{(k)}}{\rho})$$

$$\mathbf{y}_2^{(k+1)} \leftarrow \mathscr{S}_{\frac{\beta_2}{\rho}}(G(\mathbf{t}^{(k+1)}) + \frac{\mathbf{\Gamma}_2^{(k)}}{\rho})$$

7: Multiplier update by

$$\mathbf{\Gamma}_1^{(k+1)} \leftarrow \mathbf{\Gamma}_1^{(k)} + \rho(D(\mathbf{P}^{(k+1)}) - \mathbf{t}^{(k+1)} - \mathbf{y}_1^{(k+1)}),$$
$$\mathbf{\Gamma}_2^{(k+1)} \leftarrow \mathbf{\Gamma}_2^{(k)} + \rho(G(\mathbf{t}^{(k+1)}) - \mathbf{y}_2^{(k+1)}),$$
$$\mathbf{\Gamma}_3^{(k+1)} \leftarrow \mathbf{\Gamma}_3^{(k)} + \rho(\mathbf{Z}^{(k+1)} - \mathbf{P}^{(k+1)}).$$

8: **if** convergence **then**
9: break
10: **end if**
11: **end for**

Ensure: $(\hat{\mathbf{S}}, \hat{\mathbf{P}})$

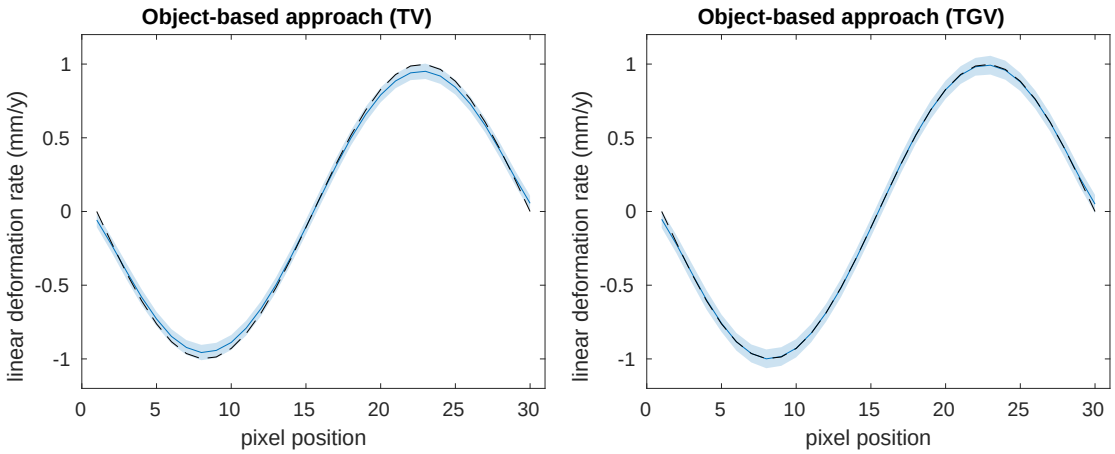

Figure 4.7: Monte-Carlo simulations for analyzing the performance of TV and TGV regularizations on sine signals. It can be clearly seen that object-based approach with TGV can better approximate the nonlinear function than TV. When comes to the high-order variation, e.g. around the trough and crest areas of the sine function, bias is existed in the result based on TV regularization, which does not happen in the result of TGV regularization.

4.4 Robust object-based phase recovery

In real data, the observed data stack $\mathscr{G}$ may contain outliers. The proposed MAP is based on Gaussian noise that cannot robustly reconstruct the deformation matrix. To deal with such circumstance, the abovementioned approach is extended to a robust version in case outliers exist. A robust object-based phase recovery step to the observed phase stack $\mathscr{G}$, prior to the object-based parameter reconstruction, is proposed in this section.

The basic idea is simple: the observed phase tensor $\mathscr{G}$ can be decomposed into two parts: the low-rank tensor part $\mathscr{X}$ and the sparse outlier tensor part $\mathscr{E}$, as the outlier-free complex phase stack $\mathscr{X}$ can be considered as a low rank tensor compared to the observed phase tensor $\mathscr{G}$. Estimating $\mathscr{X}$ leads to the following optimization problem, which is also termed as High order Robust Principal Component Analysis (HoRPCA) [GQ14]:

$$\min_{\mathscr{X},\mathscr{E}} \|\mathscr{X}\|_* + \gamma\|\mathscr{E}\|_1 \quad s.t.\ \mathscr{X}+\mathscr{E}=\mathscr{G}, \tag{4.32}$$

where $\|\mathscr{X}\|_*$ denotes the tensor nuclear norm, $\|\mathscr{E}\|_1$ is the tensor L_1 norm of sparse outliers, and γ is the regularization parameter. $\|\mathscr{X}\|_*$ can be calculated by the sum of the N nuclear norm $\sum_n \|\mathbf{X}_{(n)}\|_*$ of the mode-n unfoldings of $\mathscr{X}$, i.e. $\|\mathscr{X}\|_* = \sum_n \|\mathbf{X}_{(n)}\|_*$.

Such convex optimization problem can also be solved by ADMM. Specifically, the constraint optimization problem Equation (4.32) is converted to its augmented Lagrangian function:

$$L(\mathscr{X},\mathscr{E},\mathscr{Y}) = \|\mathscr{X}\|_* + \gamma\|\mathscr{E}\|_1 - \langle\mathscr{Y},\mathscr{X}+\mathscr{E}-\mathscr{G}\rangle + \frac{1}{2\rho}\|\mathscr{X}+\mathscr{E}-\mathscr{G}\|_F^2, \tag{4.33}$$

where $\mathscr{Y}$ denotes the introduced dual variable and ρ is the penalty parameter. Accordingly, the minimization of L, with respect to each variable, can be solved by the following optimization subproblems:

1) $\mathscr{X}$ subproblem: The subproblem of L, with respect to $\mathscr{X}$, can be rewritten as:

$$\min_{\mathscr{X}} \|\mathscr{X}\|_* + \frac{1}{2\rho}\|\mathscr{X}+\mathscr{E}-\mathscr{G}-\rho\mathscr{Y}\|_F^2 \tag{4.34}$$

It can be solved by the Singular Value Thresholding (SVT) operator [CCS10; GRY11] of mode-$n(n=1,2,\cdots,N)$ unfolding of the tensor $\mathscr{E}-\mathscr{G}-\rho\mathscr{Y}$, where SVT operator is defined as $\mathcal{T}_\mu(\mathbf{A}) := \mathbf{U}\text{diag}(\max(\sigma_i-\mu,0))\mathbf{V}$ with $\mathbf{U}$, $\mathbf{V}$ and σ_i obtained from SVD from the matrix $\mathbf{A}$.

2) $\mathscr{E}$ subproblem: The subproblem of L, with respect to the outlier tensor $\mathscr{E}$, has the following form:

$$\min_{\mathscr{E}} \gamma\|\mathscr{E}\|_1 + \frac{1}{2\rho}\|\mathscr{X}+\mathscr{E}-\mathscr{G}-\rho\mathscr{Y}\|_F^2 \tag{4.35}$$

This L_1-norm-induced subproblem can be efficiently solved by applying the soft-thresholding operator defined as $\mathcal{S}_\gamma(\mathscr{A}) := \text{sign}(\mathscr{A})\odot\max(|\mathscr{A}|-\gamma,0)$, where $\odot$ denotes the element-wise product (Hadamard product) of two tensors, and $|\mathscr{A}| = \text{sign}(\mathscr{A})\odot\mathscr{A}$.

3) Multiplier updating: The multiplier $\mathscr{Y}$ can be updated by:

$$\mathscr{Y} = \mathscr{Y} - \frac{1}{\rho}(\mathscr{X}+\mathscr{E}-\mathscr{G}) \tag{4.36}$$

Table 4.1: Numerical performance of the results shown in Figure 4.8

	PSI	w/o robust phase recovery	w/robust phase recovery
standard deviation (mm/y)	1.27	1.10	**0.08**
mean (mm/y)	0.02	0.03	**0.003**

The detailed ADMM pseudocode for solving Equation (4.32) is summarized in Algorithm 3.By the pre-defined convergence condition, the optimal solution $\hat{\mathcal{X}}, \hat{\mathcal{E}}$ can be obtained. Then, $\mathcal{G}$ in Equation (4.7) can be replaced by the outlier-free tensor $\hat{\mathcal{X}}$ for deformation parameter retrieval.

Algorithm 3 Equation (4.32) solved by ADMM

Require: $\mathcal{G}, \gamma, \rho, N$

1: Initialize $\mathcal{X} = \mathcal{E} = \mathcal{Y} = 0$
2: **for** $k = 0$ to maxIter **do**
3: SVT for mode-n unfolding of $\mathcal{G} + \mu\mathcal{Y} - \mathcal{E}$, mode-$n$ folding as N tensors, and then average them by N:
$\mathcal{X}^{(k+1)} \leftarrow \frac{1}{N}\sum_{n=1}^{N} \mathcal{T}_{n,\rho N}(\mathbf{G}_{(n)} + \rho\mathbf{Y}_{(n)}^{(k)} - \mathbf{E}_{(n)}^{(k)})$,
where $\mathcal{T}_{n,\rho N}(\cdot) := \text{fold}_n(\mathcal{T}_{\rho N}(\cdot))$
4: Element-wise soft-thresholding of tensor $\mathcal{G} + \rho\mathcal{Y}^{(k)} - \mathcal{X}^{(k+1)}$:
$\mathcal{E}^{(k+1)} \leftarrow \mathcal{S}_{\rho\gamma}(\mathcal{G} + \rho\mathcal{Y}^{(k)} - \mathcal{X}^{(k+1)})$
5: $\mathcal{Y}^{(k+1)} \leftarrow \mathcal{Y}^{(k)} - \frac{1}{\rho}(\mathcal{X}^{(k+1)} + \mathcal{E}^{(k+1)} - \mathcal{G})$
6: **end for**

Ensure: $(\mathcal{X}, \mathcal{E})$

To investigate the proposed object-based approach with the robust phase recovery, outliers are simulated by replacing 30% randomly selected pixels of the simulated data (SNR=5dB) used in Figure 4.3 with uniformly distributed phases. The deformation estimates of the methods including PSI and object-based approach with and without robust phase recovery are illustrated in Figure 4.8. It can be seen that most noisy points can be suppressed in the result of object-based approach. However, as shown in the plots of residual values, outliers are persisted, since the TV regularization tends to preserve sparse changes in signals. As a comparison, the proposed robust phase recovery step can effectively remove outliers at first and the second stage of object-based approach can efficiently recover the deformation parameters. Quantitatively, mean and standard deviations of the residuals between the corresponding results and the ground truth are given in Table 4.1. The existed outliers severely influence the estimation of standard deviations, while with the robust phase filtering, the proposed approach can robustly estimate the geophysical parameters.

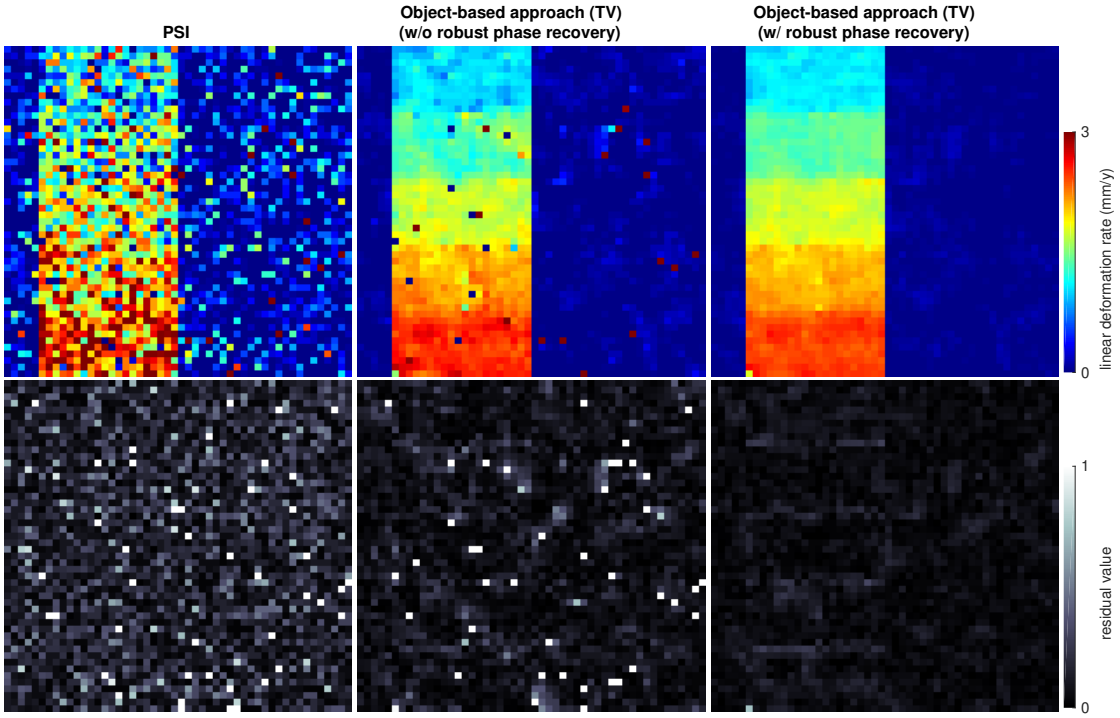

Figure 4.8: Visualized comparison with/without robust filter on the simulated dataset corrupted by outliers. It can be seen that most noisy points can be suppressed in the result of object-based approach. However, as shown in the plots of residual values, outliers are persisted, since the TV regularization tends to preserve sparse changes in signals. As a comparison, the proposed robust phase recovery step can effectively remove outliers at first and the second stage of object-based approach can efficiently recover the deformation parameters.

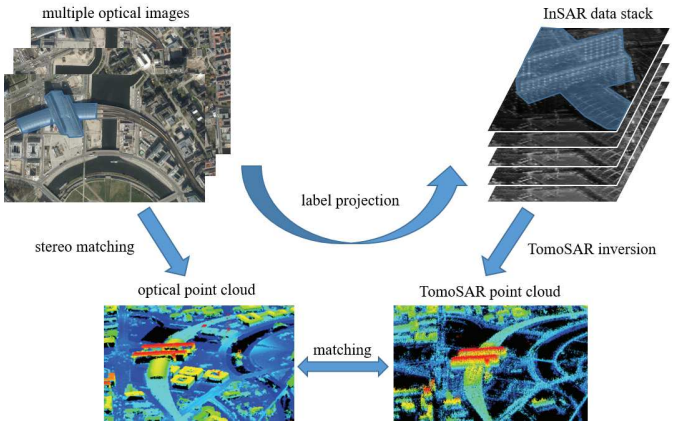

Figure 4.9: SARptical processing steps [Wan+17].

4.5 Object detection in SAR images

Due to the complex scattering mechanism and the layover effect in SAR images, the detection and the semantic classification of objects in SAR images present a greater challenge than in optical images. Still, several papers have been published in this regard. For example, [Dek03; TTM07; Tis+04; GHS00; Voi+13] provided a classification of large urban areas in SAR images, but they did not achieve the classification for each object instance. In [Thi+07; WZS14], the extraction of buildings and the estimation of their heights were well studied, with the assumptions that the buildings were following specific models or with flat roofs. In [SZ16b], models of individual buildings were reconstructed that required high quality TomoSAR point clouds as input, however. Only until recently, the 'SARptical' technique [Wan+17] has provided a promising solution. Instead of using SAR images alone, it combines the semantic classification labels obtained from optical images with SAR images via a 3D geometric coregistration.

4.5.1 SARptical processing

Object masks in interest are first derived from optical images and then projected to SAR images using the SARptical method [Wan+17]. SARptical links the pixels between SAR images and the corresponding optical images. A schematic drawing of SARptical is shown in Figure 4.9. The basic idea is to co-register the 3D models independently derived from two data sources, in order to establish a link between the 2D SAR and optical images. Its key steps are briefly listed as follows:

1. Retrieve 3D point cloud from SAR image stacks, i.e. using PSI or TomoSAR, not necessarily object-based. In this chapter, it has been done by Tomo-GENESIS - Deutsches Zentrum für Luft- und Raumfahrt (engl. German aerospace center) (DLR)'s tomographic SAR processing system [Zhu+13; ZB10b].

2. Retrieve 3D point cloud from optical images using stereo matching.

3. Co-register the TomoSAR and optical point clouds, and correct the camera positions of the optical images w.r.t. the TomoSAR 3D point cloud.
4. Estimate an average height of the target object label from the matched point cloud.
5. Project the object label to SAR image coordinate (range-azimuth).

4.5.2 Bridge extraction in optical images

Based on the above-mentioned pipeline of object detection in SAR images, the corresponding objects are firstly detected in optical images. In this chapter, as the case study of bridges in Berlin, bridge extraction approach in optical image is introduced here. For the study of other objects in urban areas, such as roads, roofs and façades, the associated methods are extensively established in the papers [Mat+15; LL14; Mar+15] and the survey [CH16].

The proposed bridge detection algorithm is based on the following prior knowledge of bridges:

1. Bridges are above rivers.
2. One bridge should completely cross and divide the river.

4.5.2.1 Texture feature for river classification

For the first step, considering the homogenous texture of river, the river and the rest pixels can be classified by using local binary pattern (LBP) [OPH96] as the feature. LBP describes the local structure within a certain neighborhood. Compared to the intensity of the center pixel, the neighboring pixels are thresholded and multiplied by the binomial weights. The rotation-invariant uniform LBP is adopted [OPM02] to describe the texture and generate the LBP histogram feature for each patch created by a sliding window through the whole image. A Support Vector Machine (SVM) is employed as the supervised classifier, which is trained with dozens of training patches.

4.5.2.2 Retrieval of river segments by Active Contour

With the above method, a coarse classification of the river regions can be obtained. It is not sufficient to precisely determine the discontinuous regions of the rivers (which are bridges). Therefore, given the initial river mask, the Chan-Vese segmentation [CV99] is then employed to refine the river segments.

By using the level set formulation $C = \{(x,y)|\phi(x,y) = 0\}$ introduced in [OS88], where C represents the closed curve and $\phi(x,y) = 0$ is the zero-level set function. It basically solves the following minimization function [CV99]:

$$F(c_1,c_2,\phi) = \mu \int_\Omega \|\nabla H(\phi)\| + \int_\Omega (I(x,y)-c_1)^2 H(\phi)\,dx\,dy + \int_\Omega (I(x,y)-c_2)^2 (1-H(\phi))\,dx\,dy \tag{4.37}$$

where c_1, c_2 are the two unknown constants, $I(x,y)$ is the image pixel intensity with the spatial coordinate (x,y), Ω denotes the domain to be segmented, and $H(\cdot)$ is the Heaviside step

function. By setting the partial derivatives with respect to the unknown constants c_1, c_2, ϕ to be zeros and updating them recursively, the minimization problem can be solved. More detailed introductions about Chan-Vese segmentation and implementation can be seen in [Get12].

4.5.3 Bridge extraction

For bridge extraction, the centroid position of each river segment in the obtained river binary mask is determined at first. Based on this, a graph of the centroids can be built. By exploiting the minimum spanning tree (MST), each pair of river segments with bridges located in between can be determined.

Then, an α-shape contour approximation [EKS83] can be exploited to obtain the contours of river segments and each small piecewise line segment on the α-shape contour can be represented in a parametric way. The parameters chosen here are the normal direction $\mathbf{d}$ and the coordinate $\mathbf{c}$ of the middle point of the line segment. As a result, the bridge edges can be retrieved based on the following assumptions:

- The pair of line segments is parallel or approximately parallel.
- The pair of line segments is relatively close to each other.

A similarity function expressed in Equation (4.38) is introduced to incorporate the two above-mentioned criteria.

$$sim_{i,j} = \exp(-|\frac{\langle \mathbf{d}_1(i), \mathbf{d}_2(j) \rangle}{\|\mathbf{d}_1(i)\| \|\mathbf{d}_2(i)\|}|) \times \exp(\frac{\|\mathbf{c}_1(i) - \mathbf{c}_2(j)\|_2^2}{\max(\|\mathbf{c}_1(i) - \mathbf{c}_2(j)\|_2^2)}) \tag{4.38}$$

where $\mathbf{d}_1(i)$ denotes the normal direction of the ith line piece of river segment 1, $\mathbf{d}_2(j)$ is the normal direction of the jth line piece of river segment 2, and the first exponential term measures the normalized similarity of the normal directions of the two line pieces. Similarly, $\mathbf{c}_1(i)$ represents the coordinate vector of the middle point of the ith line piece of river segment 1, $\mathbf{c}_2(j)$ denotes the coordinate vector of the middle point of the jth line piece of river segment 2, $\|\mathbf{c}_1(i) - \mathbf{c}_2(j)\|_2^2$ is the Euclidean distance of the two points and the second exponential term in Equation (4.38) calculates the distance similarity normalized by the maximum distance of the two line pieces from the pair-wise river segment. Finally, based on the similarity function, the pair of line pieces under a certain similarity threshold th_{sim} can be selected as the bridge edges.

4.6 Deformation retrieval of real data based on object-based approach

In this test, the central area in Berlin is studied as shown in Figure 4.10, which contains the target bridges for the proposed object-based deformation reconstruction. Given the bridge masks obtained based on the proposed pipeline in the optical image, the corresponding bridge areas in the SAR image can be generated by the 'SARptical' framework. For example, the top bridge mask in Figure 4.10 projected in the SAR image is shown in Figure 4.11.

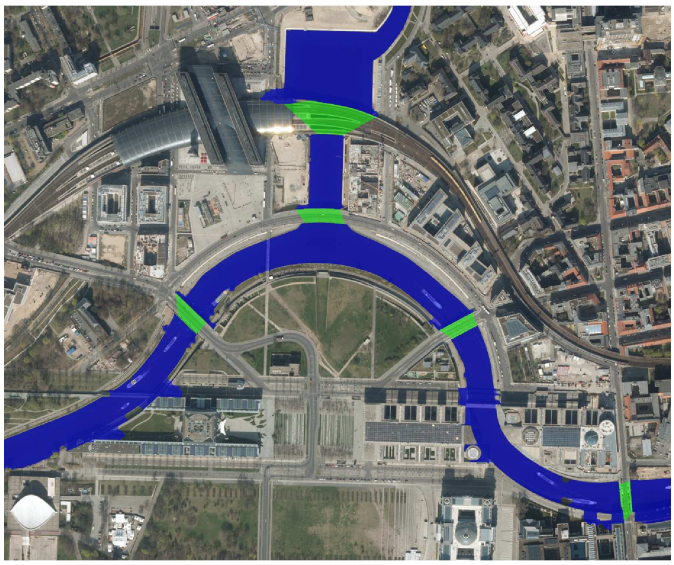

Figure 4.10: The classifications of the rivers and bridges by the proposed approach covered with blue and green masks, respectively. As shown from the result, some building shadows are also classified as rivers, since they share similar RGB values with those of rivers. Some bridges do show irregular shapes, especially the top one, since the bridge mask depends on the boundary of the river segments. Yet, this does not affect the bridge monitoring too much, since the bridge masks cover most parts of the bridges.

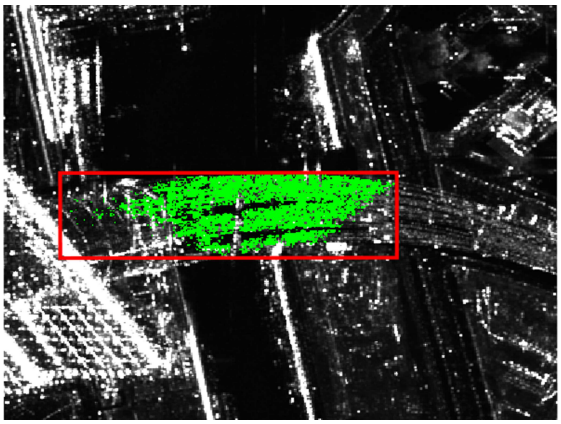

Figure 4.11: The bridge mask (green) in the SAR image obtained by projecting the corresponding mask from the optical image (SARptical), which is the top bridge shown in Figure 4.10, and the red rectangular area is used for the robust object-based deformation reconstruction.

The area extracted for the deformation reconstruction is chosen by the bounding box of the bridge mask, as indicated by the red rectangle. This area undergoes a seasonal periodic motion that is primarily caused by the thermal dilation of the steel railways on the bridge. The estimated amplitudes of this periodic motion using the proposed method and other state-of-the-art methods are shown in Figure 4.12. The result obtained by the pixel-wise periodogram (PSI) is at the top-left. Below it is the result from the TV post-processing. The SqueeSAR [Fer+11] result is located at the top-right.

The PSI shows the most noisy estimates of the amplitude of seasonal motion than the other methods. SqueeSAR utilizes the similar statistic behaviors of multiple pixels, which indeed obtains the less noisy result by averaging those pixels, especially in the left part of the bridge. However, some prominent noise still persists, without exploiting the geometric or semantic information to jointly reconstruct the deformations. Both the TV post-processing and the proposed method incorporate geometric information. Consistent with the analysis in the simulation, the separate TV filtering does filter out the majority of the noise, but it heavily depends on the results of the pixel-wise periodogram, which can be corrupted by outliers. Thereby, some large outliers still exist in the left part of the bridge. The separate TV filtering also tends to over-smooth and underestimate the deformation pattern. As a comparison, the proposed object-based approach can both mitigate the noise and the outliers, which outperforms the other methods.

The estimated amplitudes of the seasonal motion of all the bridges in central Berlin are shown in Figure 4.13. Except for the top one, the motions of all other bridges are not significant enough to draw any obvious conclusions. Interesting to note, however, is that the motion of the left-most bridge tends to be increasing from the left side to the right side. Its corresponding orthorectified optical image, with a pixel spacing of 7 cm, is shown at the left (image is provided by DLR Institute of Robotics and Mechatronics produced by semi-global matching [Hir08]). As shown by the two highlighted positions with red ellipses, the bridge is separated from the roads. In this case, there may be one reason that the motion allowances of the bridge on the two sides are different, i.e. its right side is higher than the left.

4.7 Discussion

In this chapter, a general framework for object-based multibaseline InSAR parameter estimation, i.e. introducing a spatial regularization term based on given object labels. Moreover, considering the significant amount of outliers existing in real data, a robust InSAR stack filtering approach is introduced by minimizing the rank of the InSAR stack tensor. To demonstrate the application of the proposed method for bridge monitoring, a bridge detection method in optical images is also proposed.

The simulation demonstrates that the proposed approach has an outstanding performance. The experiments show that the regularization parameter does not sensitively influence the efficiency of the reconstruction result, especially higher than SNR with 5 dB (Figure 4.6). Besides, any post-processing based on the pixel-wised reconstruction method, such as TV filtering on the result, can still carry large bias to the final result. The joint optimization of the data fidelity and the regularization term is superior to the former approaches by

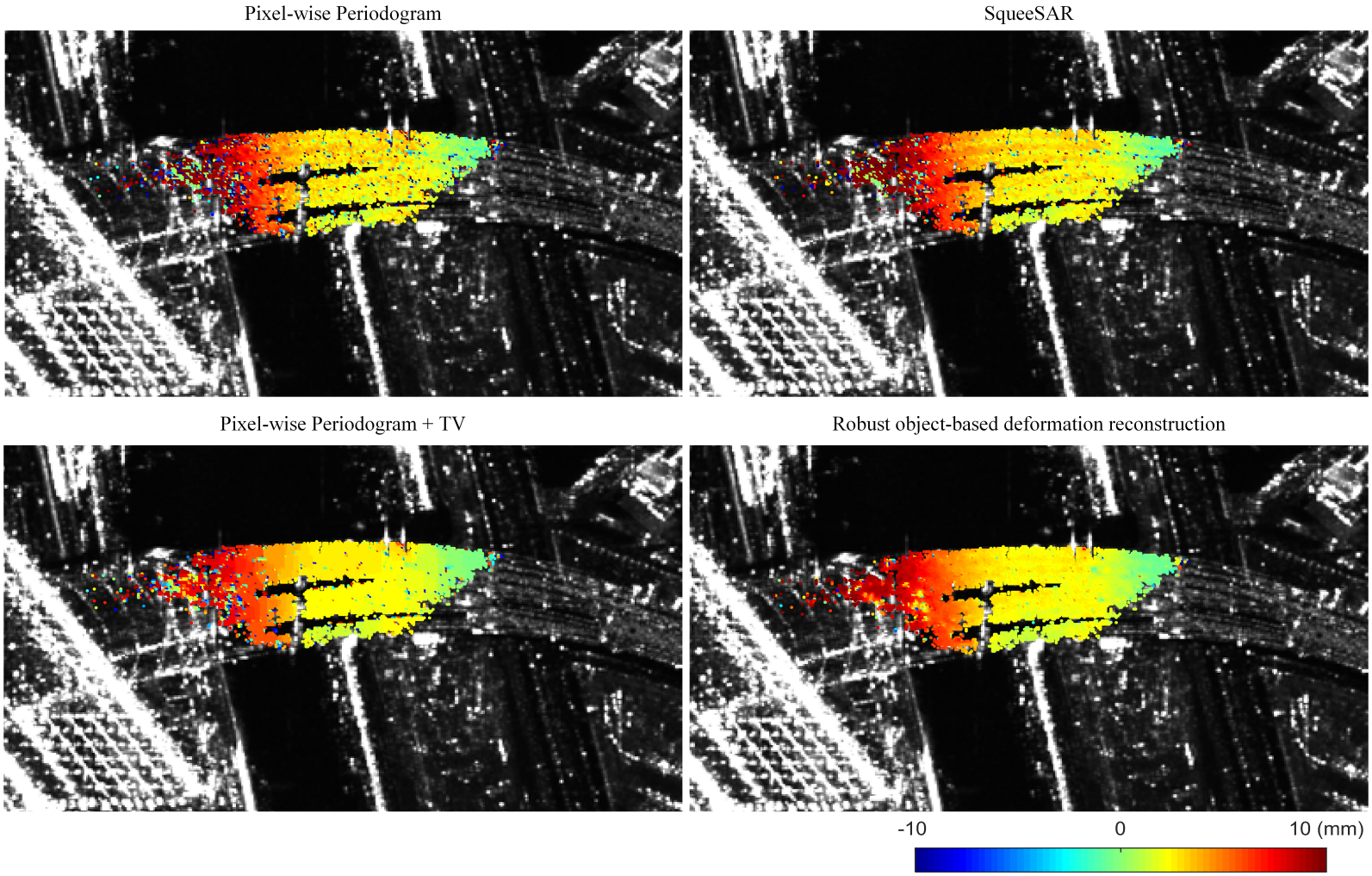

Figure 4.12: The seasonal periodic motion amplitudes of the classified bridge area shown in Figure 4.11. The pixel-wise periodogram result shows the most noisy estimates of the amplitude of seasonal motion than the other methods. SqueeSAR utilizes the similar statistic behaviors of multiple pixels, which indeed obtains the less noisy result by averaging those pixels, especially in the left part of the bridge. However, some prominent noise still persists, without exploiting the geometric or semantic information to jointly reconstruct the deformations. Both the TV post-processing and the proposed method incorporate geometric information. The separate TV filtering does filter out the majority of the noise, but it heavily depends on the results of the pixel-wise periodogram, which can be corrupted by outliers. It also tends to over-smooth and underestimate the deformation pattern. As a comparison, the proposed approach can both mitigate the noise and the outliers, which outperforms the other methods.

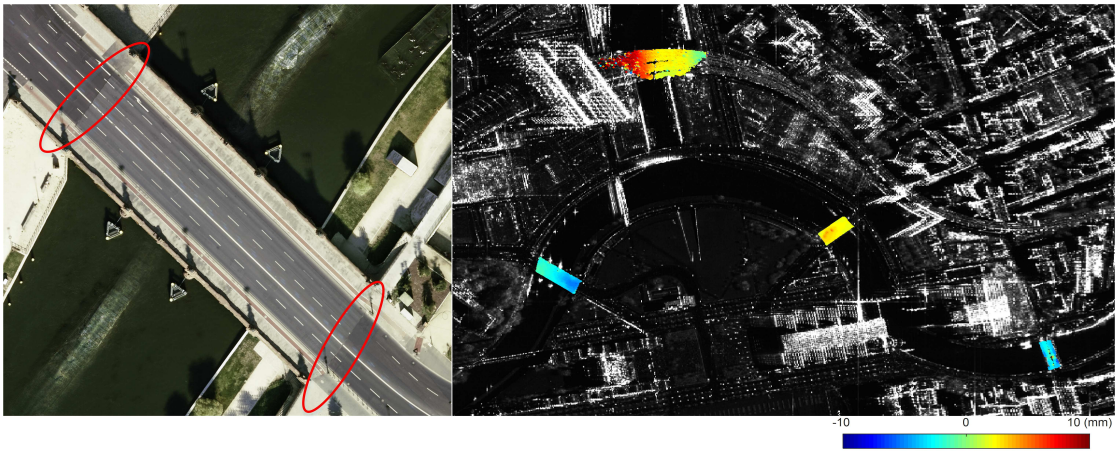

Figure 4.13: The estimated amplitudes of the seasonal motion of all the bridges in central Berlin by the proposed robust object-based deformation reconstruction. Except for the top one, the motions of all other bridges are not significant enough to draw any obvious conclusions. Interesting to note, however, is that the motion of the left-most bridge tends to be increasing from the left side to the right side. Its corresponding orthorectified optical image, with a pixel spacing of 7 cm, is shown to the left (image is provided by DLR Institute of Robotics and Mechatronics produced by semi-global matching [Hir08]). As shown by the two highlighted positions of the red ellipses, the bridge is separated from the roads. In this case, there may be one reason that the motion allowances of the bridge on the two sides are different, i.e. its right side is higher than the left.

simultaneously balancing the two terms. It achieves a better efficiency and detail preservation, which in turn can reduce the number of images required for a reliable estimation. The proposed approach with robust phase recovery is also proven to be effective against outliers. It outperforms the non-robust pixel-wise approach by a factor of twenty in terms of the standard deviation of the estimates, at 5 dB SNR with an outliers percent of 30%. Also, it achieves more reliable results than the one without the robust phase recovery step. Therefore, in case outliers exist, this step is necessary for the object-based deformation reconstruction.

To summarize, the proposed robust object-based approach is a novel framework that combines geometric information and multibaseline InSAR methods. It is suited for areas with homogenous pixels, like SqueeSAR, as well as for urban areas where the pixels are highly nonergodic. The proposed approach can be efficiently solved by ADMM optimization framework, which renders it suitable for operational processing. It also demonstrates the advantage of fusing optical and SAR images, especially for the monitoring of urban areas.

5 Low-rank analysis in object-based multibaseline InSAR

As an alternative to the typical single-pixel methods, an object-based multibaseline InSAR framework is introduced in the last chapter, which enables the exploitation of inherent properties of InSAR phase stacks on an object level. In this chapter, low-rank modeling technique and its associated application in research fields are first introduced in Section 5.1. Then, low-rank property inherent in InSAR phase stacks is studied in Section 5.2. In order to robustly reconstruct object-based InSAR phase stacks, RoMIO method is proposed in Section 5.3. Moreover, by jointly exploiting low-rank and variational prior knowledge, a TV regularized robust low rank tensor decomposition method is investigated in Section 5.4. Without requiring the precise segmentation of object masks, the proposed tensor-decomposition based methods can be efficiently exploited for object-based geophysical parameter estimation. A short discussion for this chapter is finally presented in Section 5.5.Most materials in this chapter have been published in [Kan+18].

5.1 Low-rank modeling

Data in many research fields, such as image processing, natural language processing and remote sensing, often have high dimensionality which brings challenges for the analysis. It is fortunate that such high-dimensional data are often embedded in low-dimensional subspace [Zho+15]. In mathematics, such low dimensionality is usually described by the rank of data matrix, i.e. $\text{rank}(\mathbf{D}) << \min(m,n)$, where each data point is m-dimensional vector $\mathbf{d}_i$ and the data matrix $\mathbf{D}$ is represented by $[\mathbf{d}_1,\cdots,\mathbf{d}_n]$. As demonstrated in Figure 5.1, there are just several dominant singular values of Lena image with the size of 512×512 and most of them are near zero. By reconstructing the image based on only 50 singular values, it can be observed in Figure 5.2 that the main information can be preserved. For a detailed introduction of low-rank modeling theory, the readers are referred to [MU12; Zho+15].

One of the best known low rank modeling approaches is Principal Component Analysis (PCA) [WEG87], which finds a low rank version of the matrix by minimizing the approximation error to the original data matrix in a least-squares sense. It has been utilized for tackling various problems in remote sensing, such as SAR-image-based change detection [YB13], hyperspectral image denoising [CQ11], data feature extraction [YT03], and so on. For applications in the InSAR field, PCA has recently been utilized for decomposing the scatterer covariance matrix in CAESAR [For+15], in order to separate layovered scatterers within individual pixels.

However, due to the assumption of independent and identically distributed (i.i.d.) Gaussian samples, PCA is sensitive to the existence of outliers. To robustly recover the low rank

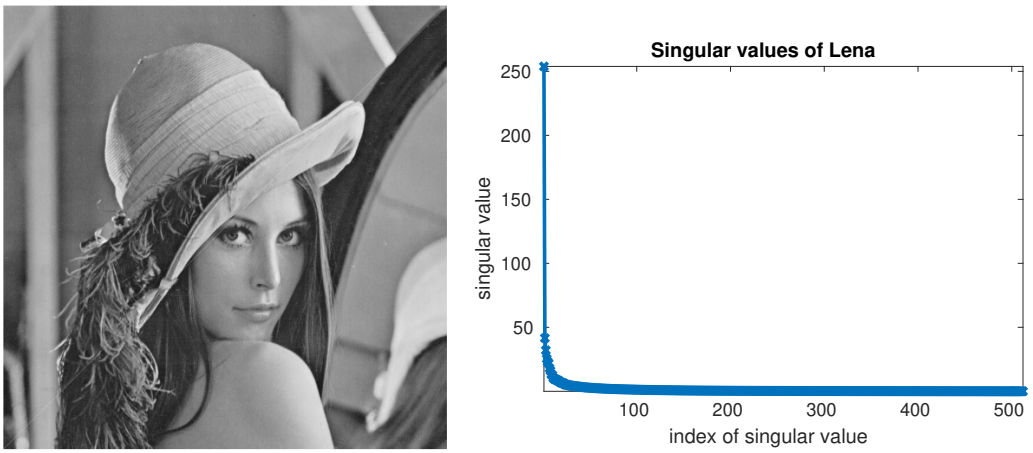

Figure 5.1: Singular values of Lena image. It can be observed that there are just several dominant singular values and most of them are near zero.

Figure 5.2: (Left) Original image. (Middle) Reconstructed image based on 50 singular values. (Right) The residuals. By reconstructing the image based on only 50 singular values, it can be observed in Figure 5.2 that the main information can be preserved.

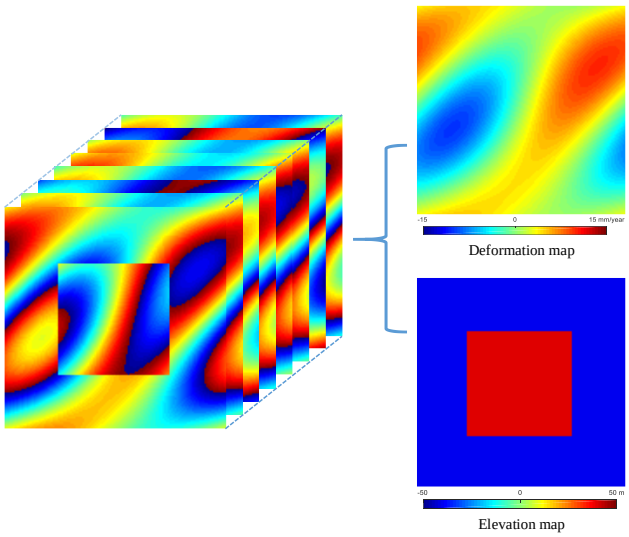

Figure 5.3: One example of an object-based InSAR phase stack, which can be represented by the tensor model in Equation (4.4). It shows the wrapped phase stack, simulated by the synthetic linear deformation rates and elevations present on its right. The pattern of the simulated elevation map is comparable to that of urban objects in real scenarios. The simulated deformation map shows a more complex pattern, which represents continuously varying displacement in the scene. The elevation and deformation maps are designed to be spatially uncorrelated.

data matrix, [Can+11] proposed Robust Principal Component Analysis (RPCA) to decompose the original matrix into a low rank data matrix and a sparse outlier matrix. For instance, RPCA was deployed for hyperspectral image restoration in [Zha+14], and a RPCA-based approach for separating stationary and moving targets in SAR imaging was investigated in [BCP13]. To deal with the data in a multidimensional case, [GQ14] proposed a robust low-rank tensor recovery method called HoRPCA, which has been employed in the previous work [Kan+17] as an outlier filtering step for object-based InSAR deformation reconstruction.

5.2 Low-rank study of InSAR phase stacks

Base on the tensor model of multibaseline InSAR data proposed in Equation (4.4), a simulated example of such a phase stack is illustrated in Figure 5.3. It shows the wrapped phase stack, and the simulated linear deformation rates and elevations from which the phase stack is constructed. The pattern of the simulated elevation map is comparable to that of urban objects in real scenarios. The simulated deformation map shows a more complex pattern, which represents continuously varying displacement in the scene. The elevation and deformation maps are designed to be spatially uncorrelated.

Such phase tensors in urban areas usually experience an inherent low rank nature, since it can be generally assumed that $\mathbf{S}$ and $\mathbf{P}$ follow certain regular structure or homogeneous

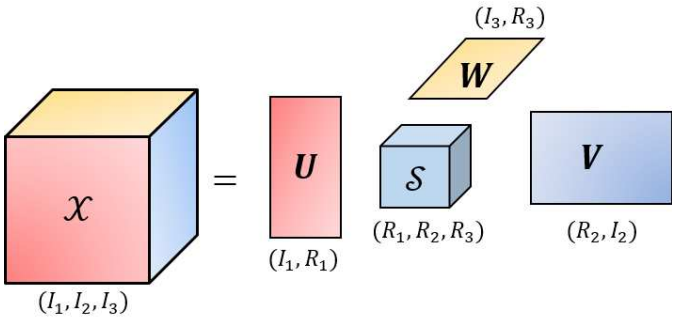

Figure 5.4: Illustration of Higher order Singular Value Decomposition (HoSVD) of a 3-mode tensor [Cic+15]

pattern, because of the regular man-made structures in urban areas. Moreover, the observed SAR images of urban object areas are usually highly correlated along the temporal dimension.

Since PCA is the most basic low rank decomposition method for matrices, it will be employed in this section to demonstrate the low rank property of InSAR phase tensor. PCA is usually realized by SVD [DL+94]. Given a matrix $\mathbf{X} \in \mathbb{C}^{I_1 \times I_2}$ and its SVD, i.e. $\mathbf{USV}^H$, the rank R approximation of $\mathbf{X}$ by truncating $\mathbf{S}$ up to R dominant singular values is the matrix $\mathbf{X}_R = \mathbf{U}_R \mathbf{S}_R \mathbf{V}_R^H$, where the $R \times R$ diagonal matrix $\mathbf{S}_R$ satisfies $\mathbf{S}_R(i,i) = \mathbf{S}(i,i), i = 1,2,\cdots,R$, $\mathbf{U}_R$ is composed by the first R columns of $\mathbf{U}$, and $\mathbf{V}_R^H$ consists of the first R rows of $\mathbf{V}^H$. This is also known as truncated SVD.

As a higher-dimensional extension of SVD, HoSVD, also known as Tucker decomposition [DLDMV00], can provide a tensor data compression based on the low rank approximation, as illustrated in Figure 5.4. It decomposes a tensor into a core tensor multiplied by a matrix along each mode. Specifically, for a 3-mode tensor, $\mathscr{X}^{I_1 \times I_2 \times I_3}$, it has

$$\mathscr{X} = \mathscr{S} \times_1 \mathbf{U} \times_2 \mathbf{V} \times_3 \mathbf{W}, \tag{5.1}$$

where $\mathbf{U}^{I_1 \times R_1}$, $\mathbf{V}^{I_2 \times R_2}$, and $\mathbf{W}^{I_3 \times R_3}$ are the factor matrices that can be considered as the principle components in each mode [KB09], $\mathscr{S}^{R_1 \times R_2 \times R_3}$ is the so-called *core tensor*, and symbol $\times_n$ is mode-n multiplication between tensor and matrix [Cic+15]. (R_1, R_2, R_3) is the so-called *multilinear rank* of $\mathscr{X}$. They fulfill the inequalities $R_1 \leqslant \min(I_1, I_2 I_3), R_2 \leqslant \min(I_2, I_1 I_3)$, and $R_3 \leqslant \min(I_3, I_1 I_2)$.

A low rank approximation of $\mathscr{X}$ can be realized by the truncated HoSVD. Take $\mathscr{X}^{I_1 \times I_2 \times I_3}$ as an example, its tensor approximation can be defined with multilinear rank (K_1, K_2, K_3), where $K_1 \leqslant R_1, K_2 \leqslant R_2, K_3 \leqslant R_3$, by the following truncated HoSVD:

$$\mathscr{X}^{I_1 \times I_2 \times I_3} \approx \mathscr{S}^{K_1 \times K_2 \times K_3} \times_1 \mathbf{U}^{I_1 \times K_1} \times_2 \mathbf{V}^{I_2 \times K_2} \times_3 \mathbf{W}^{I_3 \times K_3}, \tag{5.2}$$

where $\mathbf{U}^{I_1 \times K_1}, \mathbf{V}^{I_2 \times K_2}$ and $\mathbf{W}^{I_3 \times K_3}$ are created by storing the first $K_i (i = 1,2,3)$ singular vectors of $\mathbf{U}, \mathbf{V}$ and $\mathbf{W}$ and replacing the left $R_i - K_i (i = 1,2,3)$ vectors by zeros, and $\mathscr{S}^{K_1 \times K_2 \times K_3}$ is created in a similar way. Such truncated HoSVD finds a low rank tensor approximation of the original tensor $\mathscr{X}$ in a least-squares sense.

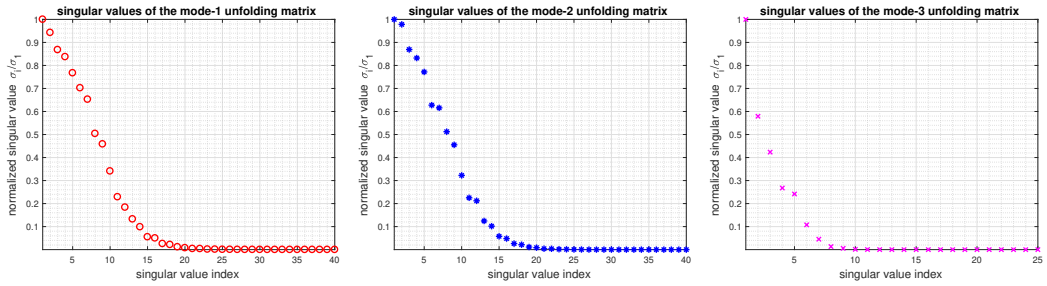

Figure 5.5: Plots of the normalized singular values of mode-1, -2 and -3 unfolding matrices of the simulated example of the complex-valued InSAR phase stack shown in Figure 5.3. For visualization, the first 40 out of all the 128 normalized singular values of mode-1 and -2 unfolding matrices are plotted. It is demonstrated that the singular values of the three unfolding matrices decay rapidly, which indicates the low rank structure of the original tensor.

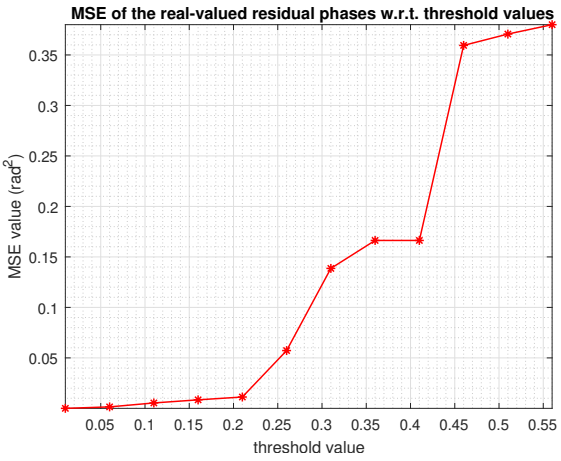

Figure 5.6: The mean squared error (MSE) values of the real-valued residual phases between the low rank approximated tensor $\hat{\mathcal{G}}$ and the original tensor $\overline{\mathcal{G}}$ i.e. MSE(angle($\hat{\mathcal{G}} \odot \text{conj}(\overline{\mathcal{G}})$)) w.r.t different threshold values.

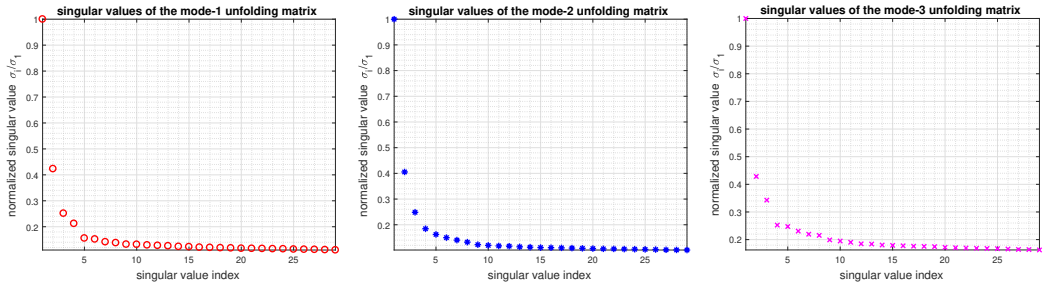

Figure 5.7: Plots of the normalized singular values of mode-1, -2 and -3 unfolding matrices of the complex-valued InSAR phase stack shown in Figure 4.1. For visualization, the first 29 normalized singular values of mode-1 and -2 unfolding matrices are plotted. It is demonstrated that the normalized singular values of the three unfolding matrices decay rapidly, and most of them are below 0.2, which indicates low rank structures of InSAR phase tensors in real cases.

In order to investigate the low rank property of an InSAR phase tensor, the normalized singular values ($\sigma_i / \max(\sigma_i)$) of the mode-1, -2 and -3 unfolding matrices of a simulated noise-free complex-valued phase tensor $\overline{\mathcal{G}} \in \mathbb{C}^{100\times100\times50}$ (shown in Figure 5.3) are plotted in Figure 5.5. It can be observed that the singular values of the three unfolding matrices decay rapidly, which indicates the low rank nature of the original tensor. The low rank tensor approximation $\tilde{\mathcal{G}}$ of $\overline{\mathcal{G}}$ can be obtained by the truncated HoSVD with a predefined threshold. As shown in Figure 5.6, the MSE values of the real-valued residual phases are calculated based on the approximated tensor $\tilde{\mathcal{G}}$ and the original tensor $\overline{\mathcal{G}}$, i.e. MSE(angle($\tilde{\mathcal{G}} \odot \text{conj}(\overline{\mathcal{G}})$)), with respect to different thresholds, where $\odot$ denotes the element-wise product and conj$(\cdot)$ is the complex conjugate operator. According to the plot, the original InSAR phase stack can be well approximated by the low rank tensor $\tilde{\mathcal{G}}$ with acceptable errors. For example, at the thresholding value of 0.21, the MSE value of the real-valued residual phases between $\tilde{\mathcal{G}}$ (its multilinear rank is $(11,12,5)$) and $\overline{\mathcal{G}}$ is around $0.01(\text{rad}^2$, which is equivalent to an uncertainty of $0.2(\text{mm/year})$ in linear deformation rate or $0.69(\text{m})$ in elevation at the baseline configuration of the simulated data. Such low rank property is often embedded in images. This is especially true in urban areas where man-made objects with regular shapes are abundant.

Such low rank property also exists in real data which usually contains full rank noise. To this end, the normalized singular values of an experimental TerraSAR-X phase tensor with a roof area (Figure 4.1) are demonstrated in Figure 5.7. The associated phase tensor has the dimensions of $256 \times 320 \times 29$. It can be seen that the normalized singular values decay rapidly and most of them are below 0.2, which indicates the low rank structure of the InSAR phase tensor.

5.3 Robust iteratively reweighted tensor decomposition

Different from HoSVD where the approximation error is minimized in a least-squares sense, robust low rank tensor decomposition minimizes the rank with L_0 norm of the approximation

error

$$\{\hat{\mathcal{X}},\hat{\mathcal{E}}\} = \underset{\mathcal{X},\mathcal{E}}{\operatorname{argmin}} \operatorname{rank}(\mathcal{X}) + \gamma\|\mathcal{E}\|_0, \quad s.t.\ \mathcal{X}+\mathcal{E} = \mathcal{G}, \tag{5.3}$$

where $\mathcal{G}$ is the observed InSAR phase tensor, $\mathcal{E}$ models the tensor of sparse outliers, $\hat{\mathcal{X}},\hat{\mathcal{E}}$ are the recovered outlier-free phase tensor and the estimated outlier tensor, respectively, $\operatorname{rank}(\mathcal{X})$ refers to the multilinear rank of $\mathcal{X}$, $\|\mathcal{E}\|_0$ denotes the L_0 norm of $\mathcal{E}$, i.e. $\|\mathcal{E}\|_0 = \|\operatorname{vec}(\mathcal{E})\|_0$, and γ is the regularization parameter.

This problem is non-deterministic polynomial-time (NP) hard, due to the minimization of the multilinear rank and the L_0 norm. Regarding this, [GQ14] suggested to replace (5.3) by HoRPCA demonstrated in Equation (4.32).

In order to better approximate the rank of a matrix and the L_0 norm of a vector, [CWB08; Pen+14] proposed a reweighted nuclear norm and L_1 minimization scheme by enhancing the low rank and sparsity simultaneously during the optimization. The reweighted L_1 norm is defined as $\|\mathbf{w}\odot\mathbf{x}\|_1$, where $\mathbf{w}$ is the weight vector that updates adaptively for enhancing the sparsity of $\mathbf{x}$. It is worth noting that if each element of $\mathbf{w}$ is exactly the inverse absolute value of the corresponding element of $\mathbf{x}$, i.e. $w_i = \frac{1}{|x_i|}$, the reweighted L_1 norm equals the L_0 norm of $\mathbf{x}$, i.e. $\|\frac{1}{|\mathbf{x}|}\odot\mathbf{x}\|_1 = \|\mathbf{x}\|_0$. For the low rank enhancement, the nuclear norm for matrix X is replaced by a reweighted version $\|\mathbf{w}\odot\boldsymbol{\sigma}(\mathbf{X})\|_1$. Likewise, if it is $w_i = \frac{1}{\sigma_i(\mathbf{X})}$, then the rewighted nuclear norm turns into the rank of the matrix $\mathbf{X}$, i.e. $\|\mathbf{w}\odot\boldsymbol{\sigma}(\mathbf{X})\|_1 = \operatorname{rank}(\mathbf{X})$.

Inspired by this, the reweighting scheme can be exploited into the tensor case. By introducing the weights for enhancing the low rank of $\mathcal{X}$ and the sparsity $\mathcal{E}$. The optimization problem is

$$\{\hat{\mathcal{X}},\hat{\mathcal{E}}\} = \underset{\mathcal{X},\mathcal{E}}{\operatorname{argmin}} \sum_{n=1}^{N} \|\mathbf{w}_{\mathcal{L},n}\odot\boldsymbol{\sigma}(\mathbf{X}_{(n)})\|_1 + \gamma\|\mathcal{W}_{\mathcal{E}}\odot\mathcal{E}\|_1 s.t. \quad \mathcal{X}+\mathcal{E} = \mathcal{G}, \tag{5.4}$$

where $\mathbf{w}_{\mathcal{L},n}$ is the weight vector for the singular values of the mode-n unfolding matrix $\mathbf{X}_{(n)}$ of $\mathcal{X}$, and $\mathcal{W}_{\mathcal{E}}$ is the weight tensor for $\mathcal{E}$. Note that if all weights are set to 1, Equation (5.4) will be equivalent to Equation (4.32).

The optimization problem Equation (5.4) can be solved by the ADMM framework. Correspondingly, such constraint optimization problem is firstly converted to its augmented Lagrangian function, yielding

$$L(\mathcal{X},\mathcal{E},\mathcal{Y}) = \sum_{n=1}^{N} \|\mathbf{w}_{\mathcal{L},n}\odot\boldsymbol{\sigma}(\mathbf{X}_{(n)})\|_1 + \gamma\|\mathcal{W}_{\mathcal{E}}\odot\mathcal{E}\|_1 - \langle\mathcal{Y},\mathcal{X}+\mathcal{E}-\mathcal{G}\rangle + \frac{1}{2\rho}\|\mathcal{X}+\mathcal{E}-\mathcal{G}\|_F^2, \tag{5.5}$$

where $\mathcal{Y}$ denotes the introduced dual variable and ρ is the penalty parameter. Accordingly, the minimization of L with respect to each variable can be solved by optimizing the following subproblems:

1) $\mathcal{X}$ subproblem: By fixing $\mathcal{E}$ and $\mathcal{Y}$, the subproblem of L with respect to $\mathcal{X}$ can be rewritten as

$$\min_{\mathcal{X}} \sum_{n=1}^{N} \|\mathbf{w}_{\mathcal{L},n}\odot\boldsymbol{\sigma}(\mathbf{X}_{(n)})\|_1 + \frac{1}{2\rho}\|\mathcal{X}+\mathcal{E}-\mathcal{G}-\rho\mathcal{Y}\|_F^2. \tag{5.6}$$

This subproblem can be solved by the Nonuniform Singular Value Thresholding (NSVT) operator [Pen+14; Gu+14]. Taking matrix $\mathbf{A}$ as an example, given the thresholding weight vector

$\mathbf{w}$, NSVT is defined as $\mathcal{T}_{\mathbf{w}}(\mathbf{A}) := \mathbf{U}\text{diag}(\max(\sigma_i - w_i, 0))\mathbf{V}$, with $\mathbf{U}$, $\mathbf{V}$ and σ_i calculated by SVD of $\mathbf{A}$.

2) $\mathcal{E}$ subproblem: By fixing $\mathcal{X}$ and $\mathcal{Y}$, the subproblem of L with respect to $\mathcal{E}$ has the following form

$$\min_{\mathcal{E}} \gamma \|\mathcal{W}_{\mathcal{E}} \odot \mathcal{E}\|_1 + \frac{1}{2\rho}\|\mathcal{X} + \mathcal{E} - \mathcal{G} - \rho\mathcal{Y}\|_F^2. \tag{5.7}$$

This weighted L_1-norm optimization subproblem can be solved by the Nonuniform Soft Thresholding (NST) operator, which is defined as $\mathcal{S}_{\mathcal{W}}(\mathcal{A}) := \text{sign}(\mathcal{A}) \odot \max(|\mathcal{A}| - \mathcal{W}, 0)$, with $|\mathcal{A}| = \text{sign}(\mathcal{A}) \odot \mathcal{A}$.

3) $\mathcal{Y}$ updating: The dual variable $\mathcal{Y}$ can be updated by

$$\mathcal{Y} = \mathcal{Y} - \frac{1}{\rho}(\mathcal{X} + \mathcal{E} - \mathcal{G}). \tag{5.8}$$

4) Weight updating: The weight vector $\mathbf{w}_{\mathcal{L},n}, n = 1, \ldots, N$ and the weight tensor $\mathcal{W}_{\mathcal{E}}$ can be updated by

$$\mathbf{w}_{\mathcal{L},n} = \frac{1}{\boldsymbol{\sigma}(\mathbf{X}_{(n)}) + \epsilon_{\mathcal{L}}}, \qquad \mathcal{W}_{\mathcal{E}} = \frac{1}{|\mathcal{E}| + \epsilon_{\mathcal{E}}}, \tag{5.9}$$

where $\epsilon_{\mathcal{L}}$ and $\epsilon_{\mathcal{E}}$ are the predetermined positive constants.

The detailed ADMM pseudocode for solving Equation (5.4) is summarized in Algorithm 4.

Using a predefined convergence condition, the solution $(\hat{\mathcal{X}}, \hat{\mathcal{E}})$ can be obtained, i.e. the outlier-free InSAR phase tensor and the sparse outlier tensor, respectively. To this end, by applying conventional multipass InSAR techniques, e.g. PSI [FPR01], on $\hat{\mathcal{X}}$, the geophysical parameters can be robustly retrieved.

Algorithm 4 RoMIO solved by ADMM

Require: $\mathcal{G}, \gamma, \mu, N, \epsilon_{\mathcal{L}} = \epsilon_{\mathcal{E}} = 1 \times 10^{-3}$

1: Initialize $\mathcal{X}^{(0)} = \mathcal{E}^{(0)} = \mathcal{Y}^{(0)} = 0$
2: **for** $k = 0$ to $k_{\max}$ **do**
3: NSVT on the mode-n, $n = 1, \ldots, N$ unfolding of $\mathcal{G} + \mu\mathcal{Y}^{(k)} - \mathcal{E}^{(k)}$, then, folding mode-$n$ tensors and averaging them by N $\mathcal{X}^{(k+1)} \leftarrow \frac{1}{N}\sum_{n=1}^{N} \mathcal{T}_{n,\mu N\mathbf{w}_{\mathcal{L},n}^{(k)}}(\mathbf{G}_{(n)} + \mu\mathbf{Y}_{(n)}^{(k)} - \mathbf{E}_{(n)}^{(k)})$, where $\mathcal{T}_{n,\mu N\mathbf{w}_{\mathcal{L},n}^{(k)}}(\cdot) := \text{fold}_n(\mathcal{T}_{\mu N\mathbf{w}_{\mathcal{L},n}^{(k)}}(\cdot))$,
4: NST on the the tensor $\mathcal{G} + \mu\mathcal{Y}^{(k)} - \mathcal{X}^{(k+1)}$: $\mathcal{E}^{(k+1)} \leftarrow \mathcal{S}_{\mu\gamma\mathcal{W}_{\mathcal{E}}^{(k)}}(\mathcal{G} + \mu\mathcal{Y}^{(k)} - \mathcal{X}^{(k+1)})$,
5: $\mathcal{Y}^{(k+1)} \leftarrow \mathcal{Y}^{(k)} - \frac{1}{\mu}(\mathcal{X}^{(k+1)} + \mathcal{E}^{(k+1)} - \mathcal{G})$,
6: Updating weights: $\mathbf{w}_{\mathcal{L},n}^{(k+1)} = \frac{1}{\boldsymbol{\sigma}(\mathbf{X}_{(n)}^{(k+1)}) + \epsilon_{\mathcal{L}}}$, $\mathcal{W}_{\mathcal{E}}^{(k+1)} = \frac{1}{|\mathcal{E}^{(k+1)}| + \epsilon_{\mathcal{E}}}$,
7: **if** convergence **then**
8: break
9: **end if**
10: **end for**

Ensure: $(\hat{\mathcal{X}}, \hat{\mathcal{E}})$

Note that the objective function of Equation (5.4) is not a convex optimization problem and the convergence of the algorithm is not theoretically guaranteed. However, its convergence on the simulated data is experimentally analyzed and displayed in Figure 5.8.

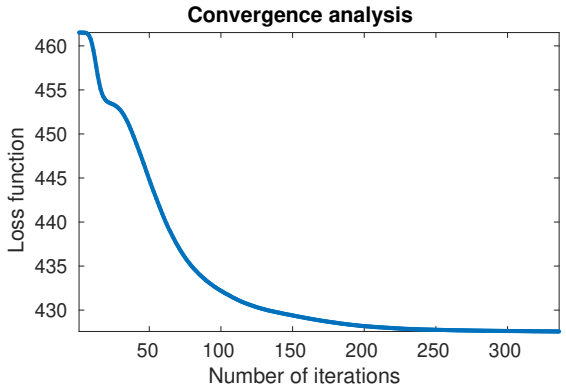

Figure 5.8: Convergence analysis of Algorithm 4.

5.3.1 Performance analysis on simulations

Two multibaseline InSAR phase stacks of 128×128 pixels by 25 images with different spatial patterns are simulated. The corresponding linear deformation and elevation maps are shown in Figure 5.11. Note that the two geophysical maps of Simulation 1 are spatially uncorrelated, while those of Simulation 2 are highly correlated. Their linear deformation rates both range from -15(mm/year) to 15(mm/year) and elevation values are from -50(m) to 50(m). The spatial baseline and the temporal baseline were chosen to be comparable to those of TerraSAR-X. Uncorrelated complex circular Gaussian noise was added to the two simulated stacks with an SNR of 5 dB, i.e. according to PS model. To simulate sparse outliers in the stacks, 30% of pixels randomly selected from the phase tensor were replaced with uniformly distributed phases.

For visualizing the performance of the proposed method, one interferogram from the recovered phase tensor $\hat{\mathscr{X}}$ is chosen and visually compared it with those obtained by NL-InSAR [DDT11] and HoRPCA [Kan+17] in Figure 5.9. Since NL-InSAR is designed for denoising one interferogram, whereas the others make use of the full image stack, to achieve a relatively fair comparison, the NL-InSAR result was obtained by averaging the results from 25 simulations of InSAR phase stacks. In the proposed method, the spatial size of the tensor is set as 128×128 (i.e. the whole stack as one tensor), γ is set to be 4.4×10^{-4} and ρ is kept constant at the value $10 \times \text{std}(\text{vec}(\mathscr{G}))$. The experiments for the associated parameter setting will be introduced in the following subsection. The search window size and the patch size in NL-InSAR is 21×21 and 5×5, respectively. In addition, the phase profile marked by the short yellow line segment in Figure 5.9, are plotted in Figure 5.10. For a quantitative evaluation, the MSE values of the real-valued residual phases between the recovered phase tensor and the ground truth, i.e. $\text{MSE}(\text{angle}(\hat{\mathscr{X}} \odot \text{conj}(\mathscr{X})))$, in cases of 30%, 40% and 50% percentages of outliers, are listed in Table 5.1.

Furthermore, the estimated results of geophysical parameters by PSI and the proposed RoMIO + PSI, using the simulated data are compared. The outlier percentage was set to 30% and SNR was 5 dB. α was set to 5×10^{-3}. The results are illustrated in Figure 5.11. The first two rows are the estimates of linear deformation rates of the two simulations and the last two rows are the corresponding elevation estimates. In addition to the experiments based on the full

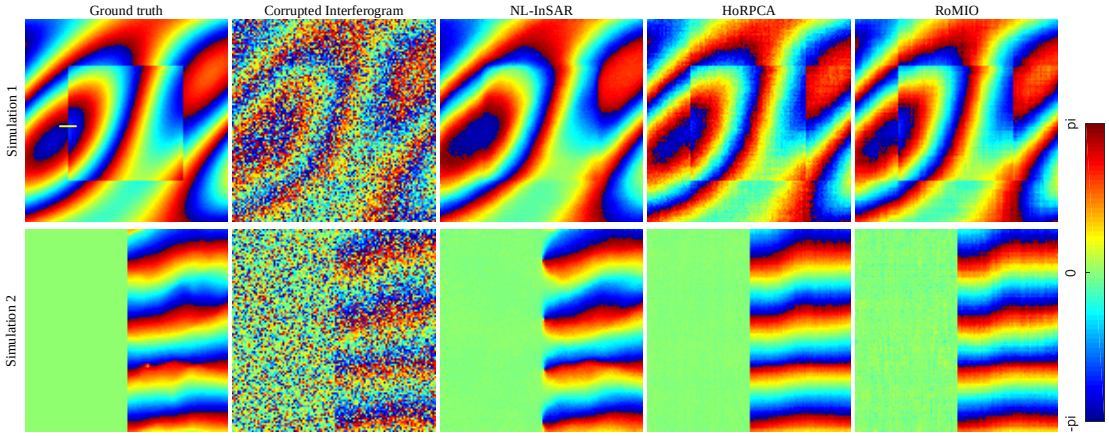

Figure 5.9: Plots of one interferogram in the two simulated InSAR phase stacks, generated by the corresponding geophysical parameters shown in Figure 5.11, as well as the corrupted phases with an SNR of 5dB and 30% outliers, and the recovered results by three methods. Although the NL-InSAR result can maintain the smooth fringes very well, the edges of rectangle in the middle are more blurred compared to the other two results. This can be clearly observed at the two cropped parts in Figure 5.10. Compared to HoRPCA, the proposed method can better keep the original structure of the interferogram, since it can better capture the low rank structure of the data and model the sparse outliers by enhancing the low rank and the sparsity.

Table 5.1: MSE performances of NL-InSAR, HoRPCA and RoMIO on the simulations shown in Figure 5.9

		Simulation 1			Simulation 2		
		NL-InSAR	HoRPCA	RoMIO	NL-InSAR	HoRPCA	RoMIO
MSE (rad^2)	30% outliers	**0.03**	0.04	**0.03**	**0.03**	0.04	0.04
	40% outliers	0.05	0.07	**0.04**	**0.05**	0.06	**0.05**
	50% outliers	0.12	0.12	**0.06**	0.07	0.12	**0.06**

stack of 25 SAR images, experiments using only 9 images were conducted in order to test the RoMIO's capability to handle small stacks. For the associated quantitative evaluation, both bias and standard deviations of the results are calculated and displayed in Table 5.2. To study the minimum number of images for RoMIO to achieve a reliable estimation, the standard deviations of the deformation estimates obtained by RoMIO + PSI are displayed in Figure 5.12, with respect to a decreasing number of SAR images down to 7.

According to the results shown in Figure 5.9, although the NL-InSAR result can maintain the smooth fringes very well, the edges of the rectangle in the middle are more blurred compared to the other two results. This can be clearly observed by the plots in Figure 5.10. Compared to HoRPCA, the proposed method can better keep the original structure of the interferogram, since it can better capture the low rank structure of the data and model the sparse outliers by enhancing the low rank and the sparsity. Consistently, the evaluation in Table 5.1 shows

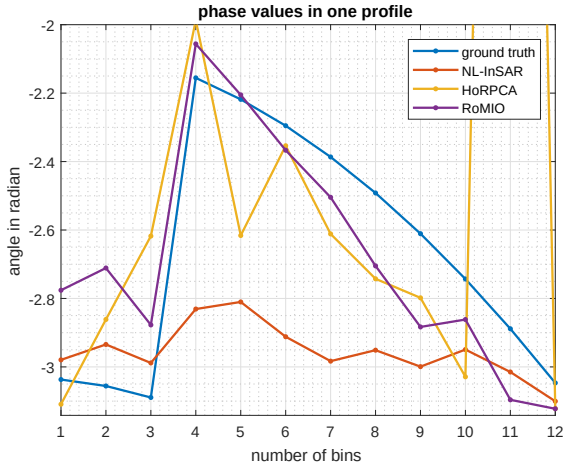

Figure 5.10: Profiles of the estimated phases marked by the short yellow line segment in Figure 5.9. It is obvious to show that the estimations of this area are blurred in the NL-InSAR result compared with the others.

Table 5.2: Quantitative study of the results in Figure 5.11

		Deformation [mm/year]		Elevation [m]	
		SD	bias	SD	bias
simulation 1	PSI (25 images)	2.68	−0.01	8.18	0.42
	PSI (9 images)	7.41	−0.04	31.56	7.02
	RoMIO+PSI (25 images)	0.27	0.01	0.39	−0.05
	RoMIO+PSI (9 images)	0.29	−0.02	1.59	0.01
simulation 2	PSI (25 images)	2.76	0.02	7.27	0.07
	PSI (9 images)	9.16	0.05	21.12	0.21
	RoMIO+PSI (25 images)	0.31	0.01	0.98	0.02
	RoMIO+PSI (9 images)	0.31	−0.01	1.17	0.13

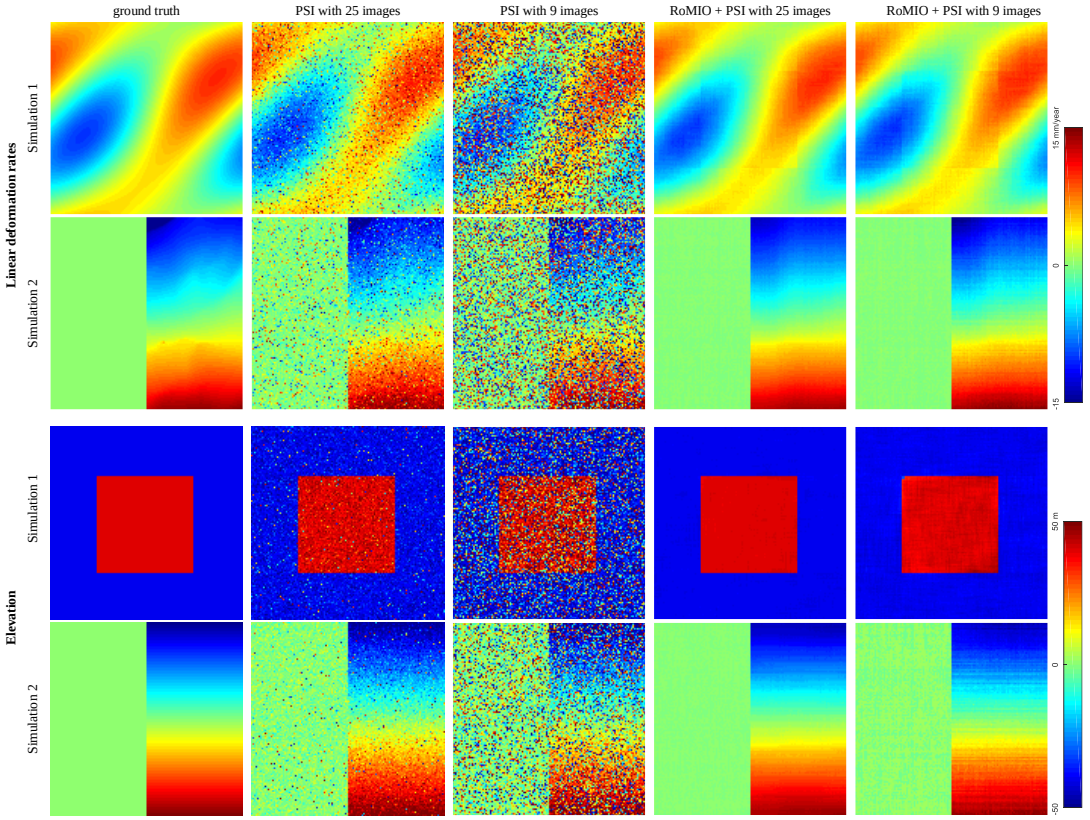

Figure 5.11: The simulated ground truth linear deformation rates and elevations of the two simulations, along with the estimated results by PSI and RoMIO + PSI with 25 and 9 SAR images. The results of PSI contain outliers. This is especially true for the result from a subset of the stack. The reason is that periodogram method in PSI is only asymptotically optimal, which means large bias is very likely to occur at low number of images. In contrast, the proposed method can robustly recover the parameters both using the full stack and a subset of the stack. That is to say the proposed method can in turn effectively reduce the number of images required for a reliable estimation.

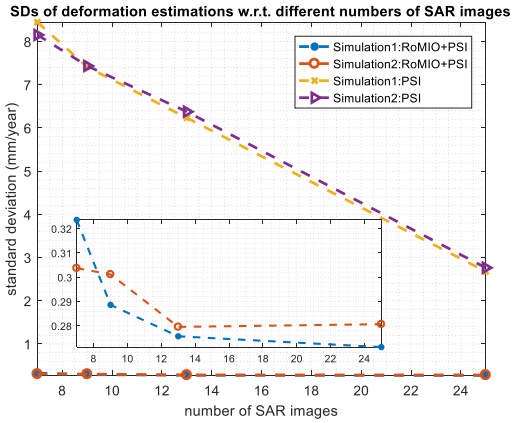

Figure 5.12: Plot of SDs of deformation estimations with respect to different numbers of SAR images for reconstruction. The proposed method can achieve a SD around 0.3[mm/year], which can improve the estimation accuracy of PSI more than ten times. It shows the accuracy of RoMIO + PSI can maintain at a better and more constant level compared to the PSI whose efficiency decreases linearly w.r.t. the number of images. At the number of images down to 7, the accuracy of RoMIO + PSI still keeps at a sub millimeter range which is about 30 times better than PSI. This creates an opportunity of multipass InSAR geophysical parameter reconstruction using very small stacks.

that under 30% percentage of outliers, both NL-InSAR and RoMIO can achieve reliable results. However, when the data is severely corrupted by outliers, e.g. 50% outliers, RoMIO can achieve a more robust performance than NL-InSAR.

Combining multibaseline InSAR techniques, e.g. PSI, with RoMIO can greatly improve the accuracy of parameter estimates. As illustrated in Figure 5.11, the results of PSI contain outliers. This is especially true for the result from a subset of the stack. The reason is that the periodogram used PSI is only asymptotically optimal, which means large bias is very likely to occur at low number of images. In contrast, the proposed method can robustly recover the parameters both using the full stack and using a subset of the stack. That is to say the proposed method can in turn effectively reduce the number of images required for a reliable estimation. For the quantitative performance, as illustrated in Table 5.2, it can be seen that the proposed geophysical parameter retrieval method — RoMIO + PSI — can improve the accuracy by a factor of ten to thirty comparing to PSI. This is also transferable to real data, as the simulation closely resembles real TerraSAR-X data. However, some artifacts are observed in the middle of the deformation estimates, which may be caused by choosing a large patch size (128×128) for optimization. Since the spatial information of phase tensors is utilized in the proposed approach, it is experimentally found that with large patch sizes, over-smoothing artifacts may exist, especially in geometrically complex areas.

As shown in Figure 5.12, according to the results of the deformation reconstruction with decreasing numbers of SAR images, the proposed method can achieve a standard deviation around 0.3(mm/year), which can improve the estimation accuracy of PSI more than ten

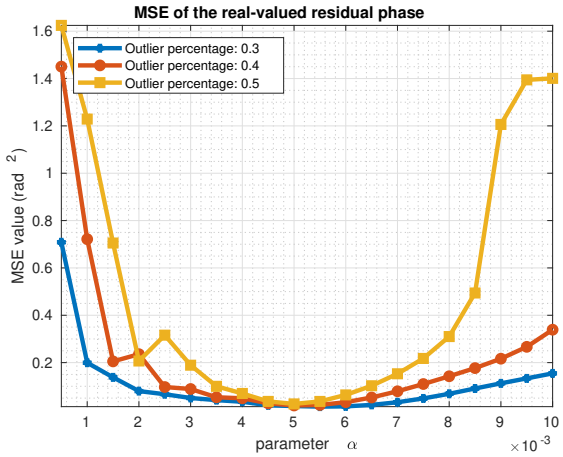

Figure 5.13: Plot of the MSE values of the real-valued residual phases between the phase tensor (Simulation 1) recovered by RoMIO and its ground truth, with respect to different parameter (α) values. As shown in the figure, even under a high percentage of outliers, e.g. 30%, the operative range of α still keeps relatively wide. Of course, this range decreases as the percentage of outliers increases. Also, the parameter can also be tuned using the L-curve method [HO93; Kan+17]. Still, for a particular dataset, the optimal α for different percentages of outliers is similar (around 5×10^{-3} in the simulation), which means that no assumptions about the amount of outliers is required.

times. Figure 5.12 shows the accuracy of RoMIO + PSI can maintain at a better and more constant level compared to the PSI whose efficiency decreases linearly w.r.t. the number of images. As the number of images down to 7, the accuracy of RoMIO + PSI still keeps at a sub millimeter range which is about 30 times better than PSI. This creates an opportunity of multibaseline InSAR geophysical parameter reconstruction using very small stacks.

5.3.2 Parameter selection

The two parameters of RoMIO are ρ and γ, where ρ comes with the introduced Lagrange multiplier term, and γ controls the balance between the low rank tensor $\mathcal{X}$ and the outlier tensor $\mathcal{E}$. As introduced in [GQ14], ρ can be set constantly with the value $10 \times \text{std}(\text{vec}(\mathcal{G}))$. For tuning γ, γ is first rewritten as $\gamma = \alpha \times \lambda_*$, where a good choice for λ_* can be set as $\frac{1}{\sqrt{\max(I_1, I_2, \cdots, I_N)}}$ according to [Can+11; GQ14], and α is a factor for tuning. To show the influence of α, Figure 5.13 presents MSE values of the real-valued residual phases of the phase stack recovered by RoMIO with respect to α (from 0.5×10^{-3} to 1×10^{-2}), under different percentages of outliers. As shown in the plot, even under a high percentage of outliers, e.g. 30%, the operable range of α still keeps relatively wide. Of course, this range decreases as the percentage of outliers increases. Still, the parameter can be tuned using the L-curve method [HO93; Kan+17]. For a particular dataset, the optimal α for different percentages of outliers is similar (around 5×10^{-3} in the simulation), which means that no assumptions about the amount of outliers is required.

Figure 5.14: (Left) The TerraSAR-X test image of one bridge area in Berlin as cropped by the yellow rectangle. The red point is the reference point for the elevation and seasonal motion reconstruction in this area. (Middle) The associated orthorectified optical image, generated using semi-global matching [Hir08]. (Right) The streetview image from Google StreetView.

Table 5.3: Lamppost height estimations of the two methods with 20 SAR images, along with the reference of LiDAR point cloud.

Unit (m)	Lamppost1	Lamppost2	Lamppost3	Lamppost4
LiDAR height	7.42			
PSI mean	6.76	7.70	8.82	10.03
PSI SD	1.39	2.17	0.26	2.56
RoMIO+PSI mean	7.13	7.69	8.91	8.01
RoMIO+PSI SD	1.30	1.74	0.28	0.46

5.3.3 Validation on real data

The first TerraSAR-X test area is a bridge in Berlin which is marked by the yellow rectangle shown in Figure 5.14 (Left), where the reference point for the elevation and seasonal motion reconstruction is plotted in red. To its right, the corresponding orthorectified optical image [Hir08] and a streetview image from Google StreetView are also displayed. The InSAR stack contains over a hundred images. However, in order to test the performance under low number of images, 20 and 9 SAR images were selected from the full stack, respectively. They were selected to be similar in their distributions and spans of the temporal and spatial baselines, so that the Cramér-Rao bounds of the estimates are comparable. The baselines were also chosen to be close to uniform distribution. The 2D baseline distribution of the selected images can be seen in Figure 5.15. The estimated amplitudes of the seasonal motion and the elevation by PSI and RoMIO + PSI are demonstrated in Figure 5.16.

As shown in Figure 5.16, consistent with the simulations, the proposed method can achieve a more robust estimation result than the classical PSI. In particular, in case of limited number of images, the interpretation of the parameters retrieved by PSI is severely influenced by outliers. The results of the proposed method are more interpretable. One can observe that the

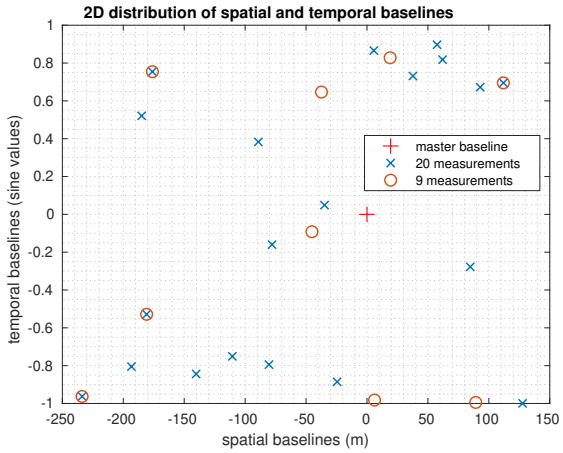

Figure 5.15: The 2D distribution of spatial and temporal baselines of the selected 20 and 9 measurements for reconstruction. The baselines were also chosen to be close to uniform distribution.

amplitudes of the motion tend to increase from one side to the other. One plausible reason is that the deformation allowances on the two sides of the bridge are different. To verify this, a very high resolution image of the bridge is shown in Figure 5.14 (Middle). The yellow ellipses in the image show that there exists certain mechanical clearance between the bridge body and the road it attaches to. Interesting to note is that in the elevation maps in Figure 5.16, there are four elevated regions which correspond to the four lampposts on the bridge. The corresponding profiles of height estimates from the results of PSI and RoMIO + PSI are plotted in Figure 5.18. Obviously, the four lampposts are well distinguishable in the result of the proposed method. In order to quantitatively evaluate the performance of the proposed method, the result in Figure 5.18 is compared to a centimeter-accuracy LiDAR point cloud shown in Figure 5.17. As InSAR is relative measurement, the height of bridge surface to match that in the LiDAR point cloud are robustly adjusted, and then the height of lampposts to those in the LiDAR point cloud can be compared. To obtain the height of bridge surface as well as the height of lampposts in the two InSAR point clouds and the LiDAR point cloud, the points within the yellow polygons shown in Figure 5.16 are robustly averaged. According to the incidence angle ($\theta = 36.1^\circ$), the estimated heights of the four lampposts based on the two methods are shown in Table 5.3. On one hand, for such high SNR areas, PSI can achieve a reliable estimation result, while the proposed method indeed increases the height estimates with smaller bias and standard deviation. On the other hand, as illustrated in Figure 5.18 and Figure 5.16, for those areas with low SNR such as bridge surface, the proposed method can also obtain much more robust estimates than PSI.

Another TerraSAR-X test dataset is the Las Vegas convention center, as shown in Figure 5.19. The total number of SAR images is 29. Since the building structure is complex and its spatial area is relatively large (800×850 pixels), the four parts of the whole InSAR phase stack as cropped with the red dashed rectangles shown in Figure 5.19 (Left) are separately processed. To its right, the associated optical image from Google Earth is also provided. Similar to the

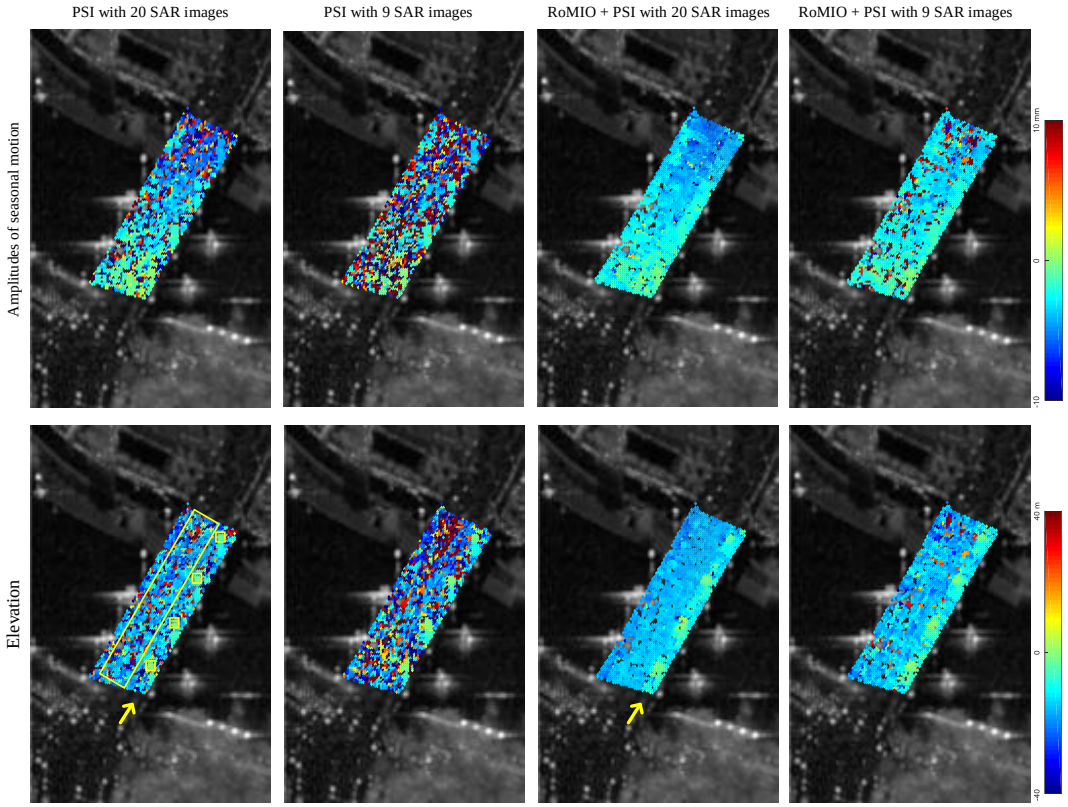

Figure 5.16: Geophysical parameter estimations (amplitudes of the seasonal motion and elevations) of the area by PSI and RoMIO + PSI with 20 and 9 SAR images. Consistent with the simulations, the proposed method can achieve a more robust estimation result than the classical PSI. In particular, under limited number of images, the interpretation of the parameters retrieved by PSI is severely influenced by outliers. The results of the proposed method are more interpretable. One can observe that the amplitudes of the motion tend to increase from one sider to the other. One plausible reason is that the deformation allowances on the two sides of the bridge are different. To verify this, a very high resolution image of the bridge is shown in Figure 5.14 (Middle). Interesting to note is that there are four elevated regions which correspond to the four lampposts on the bridge. The corresponding two profiles from the results of PSI and RoMIO + PSI are plotted in Figure 5.18.

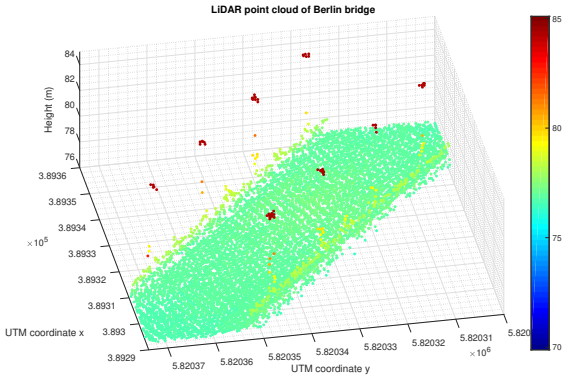

Figure 5.17: light detection and ranging (LiDAR) point cloud of the study Berlin bridge

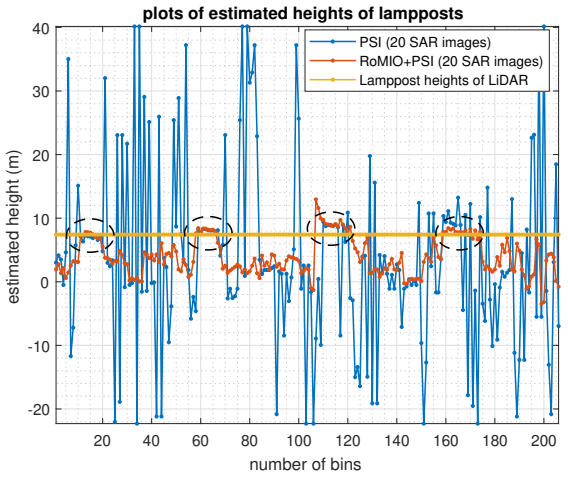

Figure 5.18: The extracted two profiles of height estimates located at the yellow arrow positions of the results of PSI and RoMIO + PSI, along with the lamppost height profile of LiDAR. Obviously, the four lampposts (shown by the black dash ellipses) are well distinguishable in the result of the proposed method.

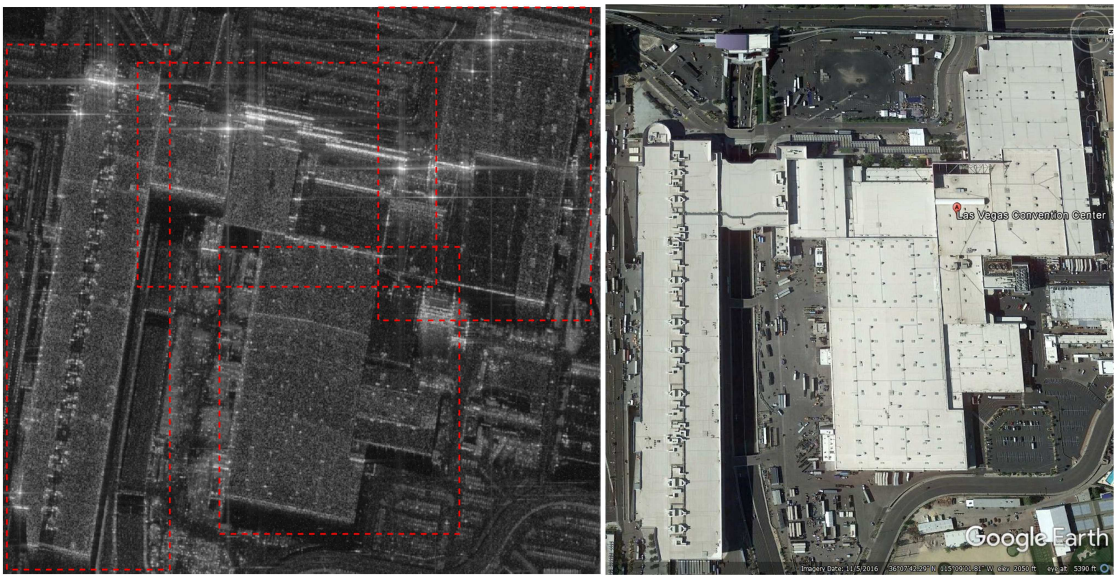

Figure 5.19: (Left) The TerraSAR-X test image of the Las Vegas convention center. Since the building structure is complex and its spatial area is large (800 × 850 pixels), the four parts of the whole InSAR phase stack as cropped with the red dashed rectangles in the figure are separately processed. (Right) The associated optical image from Google Earth.

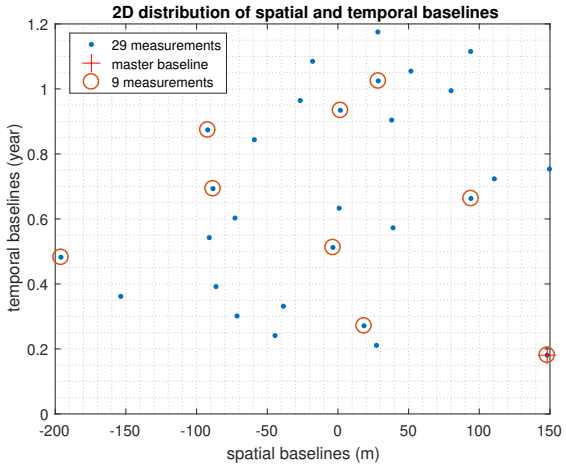

Figure 5.20: The 2D distribution of spatial and temporal baselines of the total 29 measurements is demonstrated, along with those of the selected 9 measurements for reconstruction. The baselines were also chosen to be close to uniform distribution.

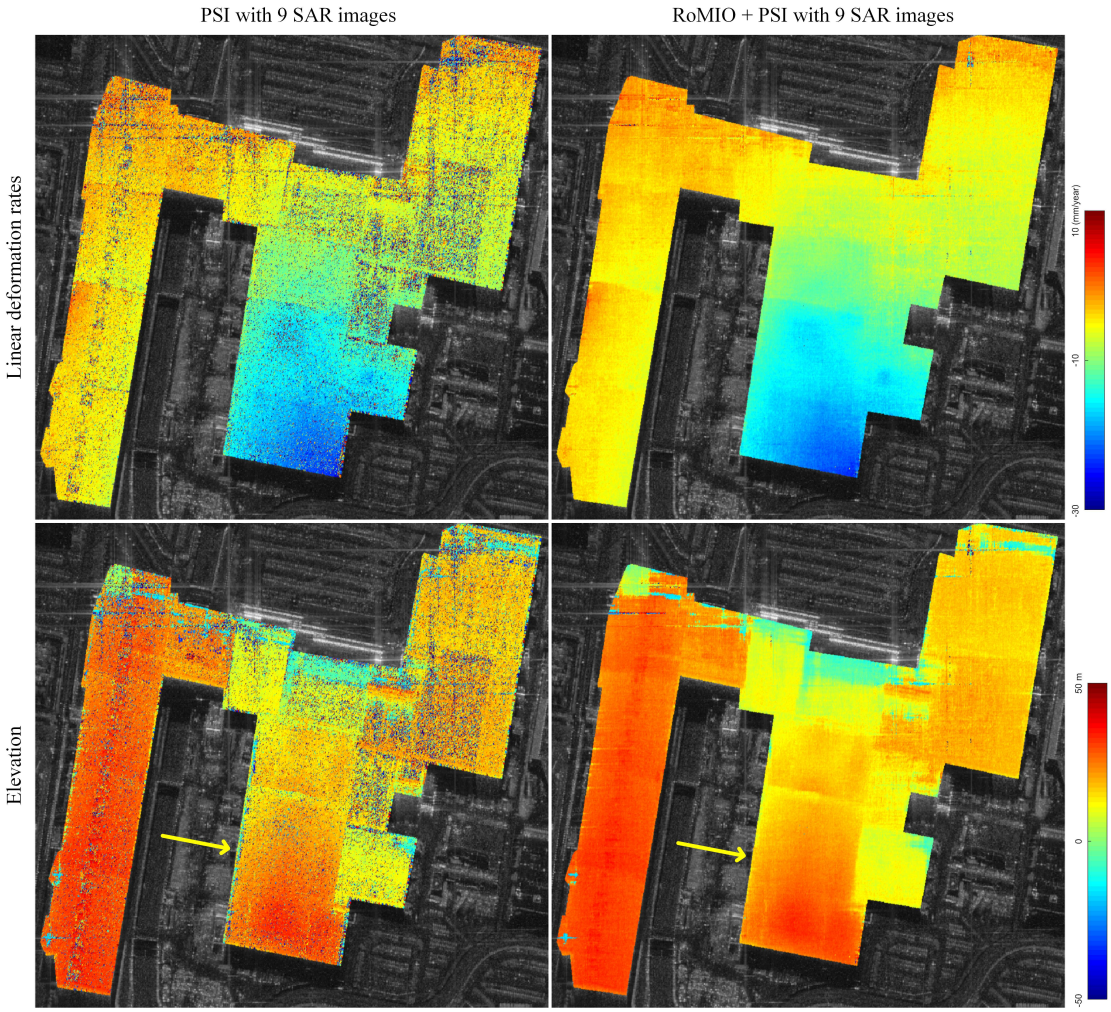

Figure 5.21: Geophysical parameter estimations (linear deformation rates and elevations) of Las Vegas convention center by PSI and RoMIO + PSI with 9 SAR images (29 images in total). The proposed method can mitigate incorrectly estimated geophysical parameters much better than PSI. Meanwhile, it is worth noting that geometric structures of the building can be preserved well.

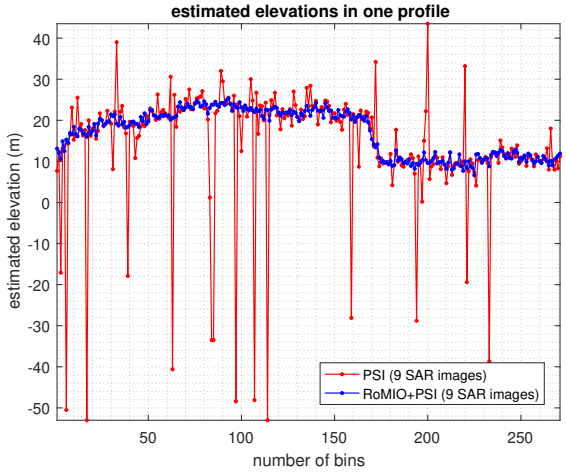

Figure 5.22: The estimated elevation profiles of the two methods, which are selected by the yellow arrows in Figure 5.21. The proposed method can preserve resolution by demonstrating a more obvious elevation step jumping than PSI, and simultaneously mitigate incorrectly estimated points.

previous experiment, the geophysical parameters are estimated by PSI and by the proposed method with a substack (9 SAR images), which were selected according to the same baseline criteria described in the previous paragraph. In Figure 5.20, the 2D distribution of spatial and temporal baselines of the total 29 measurements is demonstrated, along with those of the selected 9 measurements for reconstruction. The results are shown in Figure 5.21. Besides, 50% outliers are manually added to the stack and the parameters retrieved by PSI and RoMIO + PSI with 29 SAR images are displayed in Figure 5.23.

In the results of Las Vegas convention center shown in Figure 5.21, the proposed method can mitigate the incorrectly estimated geophysical parameters much better than PSI, under limited SAR images. Besides, it is worth noting that the geometric structure of the object can be well preserved. For instance, as shown in Figure 5.22, the elevation profiles indicated by the yellow arrows from the two results are plotted in Figure 5.21. The proposed method can preserve resolution by displaying a more obvious elevation step jumping than PSI, and simultaneously mitigates outliers. Moreover, when the data is synthetically corrupted by 50% of outliers, the geometric structures of the building cannot be well interpreted by the results of PSI as shown in Figure 5.23. In contrast, the proposed method can achieve much more reliable results.

In order to demonstrate the superior performance of the proposed method in façade area, TerraSAR-X test area of Bellagio hotel is exploited for the experiment, as illustrated in Figure 5.24. For the elevation reconstruction in this area, both PSI and the proposed method based on only 9 images are utilized. The corresponding baselines are also chosen to be close to uniform distribution. As the spatial size of this area is 500×500 pixels, a sliding window manner with the patch size of 100×100 pixels is adopted for the reconstruction based on RoMIO + PSI. Furthermore, the estimated profiles on the facade area of the two methods are plotted in Figure 5.25. As illustrated in the results, by utilizing just 9 images, much more

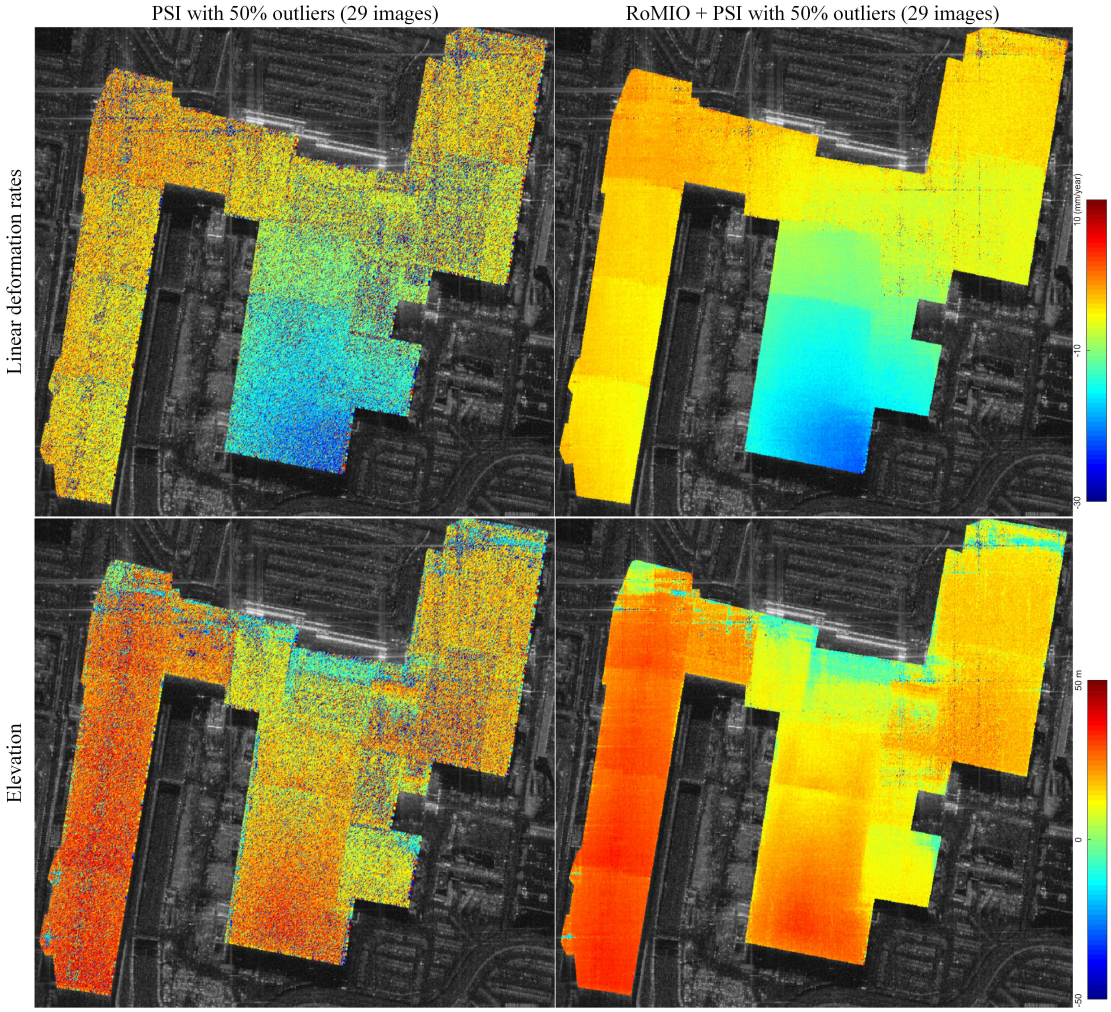

Figure 5.23: Geophysical parameter estimations (linear deformation rates and elevations) of Las Vegas convention center by PSI and RoMIO + PSI under the stack corrupted by 50% outliers. The geometric structures of the building cannot be well interpreted by the results of PSI. In contrast, the method can achieve much more reliable results than PSI.

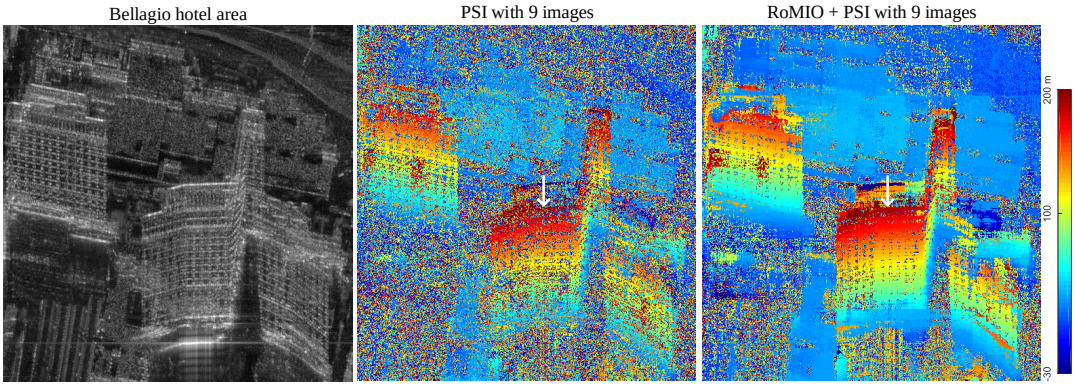

Figure 5.24: Elevation estimation of Bellagio hotel area by PSI and the proposed algorithm with 9 PSI images. By utilizing just 9 images, much more wrongly estimated points exist in the result of PSI, especially on the façades. As a comparison, the façade structures can be more easily interpreted in the result of the proposed method.

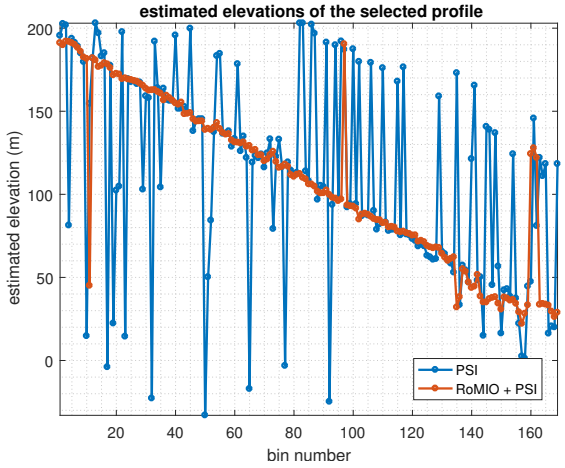

Figure 5.25: The two selected profiles of the results shown in Figure 5.24 (white arrows). Compared with PSI, most incorrectly estimated points can be mitigated by the proposed method.

wrongly estimated points exist in the result of PSI, especially on the façades. As a comparison, the façade structures can be more easily interpreted in the result of RoMIO + PSI.

5.4 Total variation regularized robust low rank tensor decomposition

As introduced before, a general framework for object-based InSAR deformation reconstruction based on a tensor-model with a regularization term is proposed in Chapter 4, which makes use of external semantic labels of various objects like bridges, roofs and façades, as an input for the support of the TV regularizer. However, it requires explicit and fairly accurate semantic labels for a reliable performance. Therefore, the inherent low rank property of multipass InSAR phase tensors is first investigated in this chapter, which allows loose semantic labels, such as a rectangle covering major part of an object, for object-based geophysical parameter reconstruction in urban areas.

As a follow-on work, a novel method for parameter retrieval from multipass InSAR data stacks by jointly considering the variational prior and the low rank property of InSAR stacks is developed. Correspondingly, a TV regularized robust low rank tensor decomposition method in complex domain is proposed in this section, in order to recover outlier-free InSAR data stacks.

Given the observed InSAR data tensor $\mathcal{G}$, it can be decomposed into two parts: a low rank tensor $\mathcal{X}$ and a sparse outlier tensor $\mathcal{E}$. To maintain smoothness structure of InSAR stacks, the decomposition can be regularized by a TV term. Correspondingly, the proposed TV regularized robust low rank tensor decomposition method is described by:

$$\{\hat{\mathcal{X}},\hat{\mathcal{E}}\} = \underset{\mathcal{X},\mathcal{E}}{\operatorname{argmin}} \alpha\|\mathcal{X}\|_{3DTV} + \beta\|\mathcal{X}\|_* + \gamma\|\mathcal{E}\|_1 \, s.t. \quad \mathcal{G} = \mathcal{X} + \mathcal{E}, \tag{5.10}$$

where $\|\mathcal{X}\|_{3DTV}$ is the 3D TV term for the three-mode tensor, $\|\mathcal{X}\|_*$ denotes the tensor nuclear norm, $\|\mathcal{E}\|_1$ is the tensor L_1 norm of sparse outliers and α, β and γ are the associated parameters for controlling the balance of the three terms. $\|\mathcal{X}\|_*$ can be calculated by the sum of the N nuclear norms of the mode-n unfoldings of $\mathcal{X}$, i.e. $\|\mathcal{X}\|_* = \sum_n \|\mathbf{X}_{(n)}\|_*$. The 3D TV term can be defined as:

$$\|\mathcal{X}\|_{3DTV} := \sum_{i_1,i_2,i_3} |x_{i_1,i_2,i_3} - x_{i_1,i_2,i_3-1}| + |x_{i_1,i_2,i_3} - x_{i_1,i_2-1,i_3}| + |x_{i_1,i_2,i_3} - x_{i_1-1,i_2,i_3}|. \tag{5.11}$$

In order to solve the optimization problem with a TV term, auxiliary variables $\mathcal{Z}$ and $\mathcal{F}$ are first introduced, and Equation (5.10) can be rewritten as:

$$\begin{aligned} \{\hat{\mathcal{X}},\hat{\mathcal{E}}\} = &\underset{\mathcal{X},\mathcal{E}}{\operatorname{argmin}} \alpha\|\mathcal{F}\|_1 + \beta\|\mathcal{X}\|_* + \gamma\|\mathcal{E}\|_1 \\ &s.t. \quad \mathcal{G} = \mathcal{X} + \mathcal{E}, \\ &\mathcal{X} = \mathcal{Z}, \; D(\mathcal{Z}) = \mathcal{F}, \end{aligned} \tag{5.12}$$

where $D(\cdot) = [D_{i_1}(\cdot); D_{i_2}(\cdot); D_{i_3}(\cdot)]$ is the three-dimensional difference operator and $D_{i_n}(\cdot)(n = 1,2,3)$ is the first-order difference operator with respect to the i_n dimension of InSAR data stack.

The corresponding constraint optimization problem can be converted into an augmented Lagrangian function, yielding

$$\begin{aligned} L(\mathcal{X},\mathcal{E},\mathcal{F},\mathcal{Z},\mathcal{T}_1,\mathcal{T}_2,\mathcal{T}_3) = \alpha\|\mathcal{F}\|_1 + \beta\|\mathcal{X}\|_* + \gamma\|\mathcal{E}\|_1 + \\ \langle\mathcal{T}_1,\mathcal{G}-\mathcal{X}-\mathcal{E}\rangle + \langle\mathcal{T}_2,\mathcal{X}-\mathcal{Z}\rangle + \langle\mathcal{T}_3,D(\mathcal{Z})-\mathcal{F}\rangle + \\ \frac{\rho}{2}(\|\mathcal{G}-\mathcal{X}-\mathcal{E}\|_F^2 + \|\mathcal{X}-\mathcal{Z}\|_F^2 + \|D(\mathcal{Z})-\mathcal{F}\|_F^2), \end{aligned} \tag{5.13}$$

where $\mathcal{T}_1,\mathcal{T}_2,\mathcal{T}_3$ are the introduced dual variables and ρ is the penalty parameter. Accordingly, the minimization of $L(\mathcal{X},\mathcal{E},\mathcal{F},\mathcal{Z},\mathcal{T}_1,\mathcal{T}_2,\mathcal{T}_3)$ with respect to each variable can be solved by optimizing the following subproblems: $\mathcal{X}$ *subproblem*: By fixing the other variables, the subproblem of L with respect to $\mathcal{X}$ is:

$$\min_{\mathcal{X}} \beta\|\mathcal{X}\|_* + \frac{\rho}{2}\|\mathcal{X} - \frac{1}{2}(\mathcal{G}-\mathcal{E}+\mathcal{Z}+\frac{\mathcal{T}_1-\mathcal{T}_2}{\rho})\|_F^2, \tag{5.14}$$

which can be solved by the SVT operator.

$\mathcal{Z}$ *subproblem*: By fixing the other variables, the subproblem of L with respect to $\mathcal{Z}$ has the following form:

$$\begin{aligned} \min_{\mathcal{Z}} \langle\mathcal{T}_2,\mathcal{X}-\mathcal{Z}\rangle + \langle\mathcal{T}_3,D(\mathcal{Z})-\mathcal{F}\rangle + \\ \frac{\rho}{2}(\|\mathcal{X}-\mathcal{Z}\|_F^2 + \|D(\mathcal{Z})-\mathcal{F}\|_F^2). \end{aligned} \tag{5.15}$$

Then, by calculating the gradient of L with respect to $\mathcal{Z}$ and setting it as zero, it has:

$$(\rho\mathbf{I}+\rho D^*D)\mathcal{Z} = \mathcal{T}_2 - D^*(\mathcal{T}_3) + \rho\mathcal{X} + \rho D^*(\mathcal{F}), \tag{5.16}$$

where $D^*(\cdot)$ is the adjoint operator of $D(\cdot)$. According to the block-circulant structure of the matrix D^*D, this inverse problem can be efficiently solved by exploiting 3D FFT and its inverse transform.

$\mathcal{F}$ *subproblem*: By fixing the other variables, the subproblem of L with respect to $\mathcal{F}$ can be written as:

$$\min_{\mathcal{F}} \alpha\|\mathcal{F}\|_1 + \frac{\rho}{2}\|\mathcal{F} - D(\mathcal{Z}) - \frac{\mathcal{T}_3}{\rho}\|_F^2. \tag{5.17}$$

This L_1-norm-induced subproblem can be efficiently solved by applying the soft-thresholding operator.

$\mathcal{E}$ *subproblem*: By fixing the other variables, the subproblem of L with respect to $\mathcal{E}$ is:

$$\min_{\mathcal{E}} \gamma\|\mathcal{E}\|_1 + \frac{\rho}{2}\|\mathcal{E} - \mathcal{G} + \mathcal{X} - \frac{\mathcal{T}_1}{\rho}\|_F^2. \tag{5.18}$$

Likewise, this subproblem can also be solved by soft-thresholding operator.

Multiplier Updating: All the dual variables can be updated by:

$$\begin{aligned} \mathcal{T}_1 &= \mathcal{T}_1 + \rho(\mathcal{G}-\mathcal{X}-\mathcal{E}), \\ \mathcal{T}_2 &= \mathcal{T}_2 + \rho(\mathcal{X}-\mathcal{Z}), \\ \mathcal{T}_3 &= \mathcal{T}_3 + \rho(D(\mathcal{Z})-\mathcal{F}). \end{aligned} \tag{5.19}$$

Using a predefined convergence condition, the solution ($\hat{\mathscr{X}}$ and $\hat{\mathscr{E}}$) can be obtained, i.e. the outlier-free InSAR data tensor and the sparse outlier tensor, respectively. To this end, by applying conventional multipass InSAR techniques, e.g. periodogram, on $\hat{\mathscr{X}}$, the geophysical parameters can be robustly retrieved.

Algorithm 5 Problem Equation (5.12) solved by ADMM

Require: $\mathscr{G}, \alpha, \beta, \gamma, N$

1: Initialize $\mathscr{X} = \mathscr{E} = \mathscr{Z} = \mathscr{F} = \mathscr{T}_1 = \mathscr{T}_2 = \mathscr{T}_3 = 0$, $\mu_{\max} = 10^{10}$, $\eta = 1.1$, $\mu = 10^{-2}$

2: **for** $k = 0$ to maxIter **do**

3: Update $\mathscr{X}^{(k+1)}$ by SVT for mode-n unfolding matrix of $\frac{1}{2}(\mathscr{G} - \mathscr{E}^{(k)} + \mathscr{Z}^{(k)} + \frac{\mathscr{T}_1^{(k)} - \mathscr{T}_2^{(k)}}{\mu})$, then mode-$n$ folding of the results as N tensors and average them by N:
$\mathscr{X}^{(k+1)} \leftarrow \frac{1}{N}\sum_{n=1}^{N} \mathscr{S}_{n,\beta N/\mu}(\frac{1}{2}(\mathbf{G}_{(n)} - \mathbf{E}_{(n)}^{(k)} + \mathbf{Z}_{(n)}^{(k)} + \frac{\mathbf{T}_{1(n)}^{(k)} - \mathbf{T}_{2(n)}^{(k)}}{\mu}))$, where $\mathscr{S}_{n,\beta N/\mu}(\cdot) := \text{fold}_n(\mathscr{S}_{\beta N/\mu}(\cdot))$.

4: Update $\mathscr{Z}^{(k+1)}$ by calculating $H_{\mathscr{Z}}$ and $T_{\mathscr{Z}}$, where
$H_{\mathscr{Z}} = \mathscr{T}_2^{(k)} - D^*(\mathscr{T}_3^{(k)}) + \mu\mathscr{X}^{(k+1)} + \mu D^*(\mathscr{F}^{(k)})$ and
$T_{\mathscr{Z}} = |\text{fftn}(D_1)|^2 + |\text{fftn}(D_2)|^2 + |\text{fftn}(D_3)|^2$,
$\mathscr{Z}^{(k+1)} \leftarrow \text{ifftn}(\frac{\text{fftn}(H_{\mathscr{Z}})}{\mu\mathbf{I} + \mu T_{\mathscr{Z}}})$.

5: Update $\mathscr{F}^{(k+1)}$ by element-wise soft-thresholding of tensor $D(\mathscr{Z}^{(k+1)}) + \mathscr{T}_3^{(k)}/\mu$:
$\mathscr{F}^{(k+1)} \leftarrow \mathscr{R}_{\alpha/\mu}(D(\mathscr{Z}^{(k+1)}) + \mathscr{T}_3^{(k)}/\mu)$.

6: Update $\mathscr{E}^{(k+1)}$ by element-wise soft-thresholding of tensor $\mathscr{G} + \mathscr{T}_1^{(k)}/\mu - \mathscr{X}^{(k+1)}$:
$\mathscr{E}^{(k+1)} \leftarrow \mathscr{R}_{\gamma/\mu}(\mathscr{G} + \mathscr{T}_1^{(k)}/\mu - \mathscr{X}^{(k+1)})$.

7: Update $\mathscr{T}_1^{(k+1)}$, $\mathscr{T}_2^{(k+1)}$ and $\mathscr{T}_3^{(k+1)}$ by
$\mathscr{T}_1^{(k+1)} \leftarrow \mathscr{T}_1^{(k)} + \mu(\mathscr{G} - \mathscr{X}^{(k+1)} - \mathscr{E}^{(k+1)})$,
$\mathscr{T}_2^{(k+1)} \leftarrow \mathscr{T}_2^{(k)} + \mu(\mathscr{X}^{(k+1)} - \mathscr{Z}^{(k+1)})$,
$\mathscr{T}_3^{(k+1)} \leftarrow \mathscr{T}_3^{(k)} + \mu(D(\mathscr{Z}^{(k+1)}) - \mathscr{F}^{(k+1)})$.

8: Update μ by $\mu \leftarrow \min(\eta\mu, \mu_{\max})$.

9: **if** convergence **then**

10: break

11: **end if**

12: **end for**

Ensure: $(\hat{\mathscr{X}}, \hat{\mathscr{E}})$

5.4.1 Validation on real data

One study area is in Berlin, as shown in Figure 5.26. The InSAR stack totally contains in total 41 TerraSAR-X interferograms, with the spatial dimension of 3000 × 2500 pixels. A substack with 15 interferograms were selected from the full stack and the associated baselines were plotted in Figure 5.27. Likewise, the patch size used in the sliding-window processing is chosen as 200 × 200 pixels. For this area, the parameters of the proposed method were set as $\alpha = 0.12$, $\beta = 3$ and $\gamma = 0.5$. The estimated elevations and amplitudes of seasonal motions by PSI, RoMIO and the proposed method are displayed in Figure 5.28 and Figure 5.30, respec-

Figure 5.26: The study area of Berlin shown by the mean amplitude (log scale) of a TerraSAR-X InSAR stack.

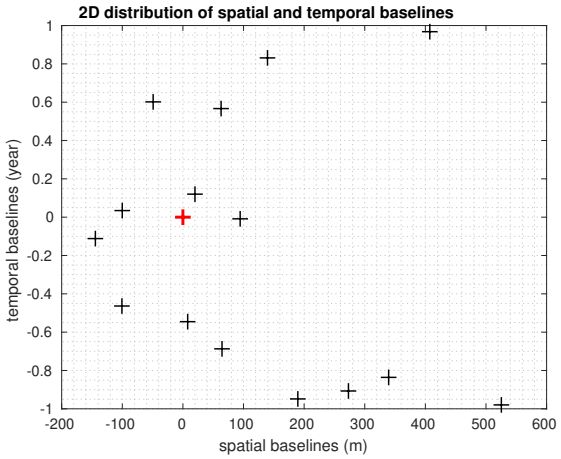

Figure 5.27: The 2D distribution of spatial and temporal baselines of the selected 15 interferograms for reconstruction. The master baseline is shown in red.

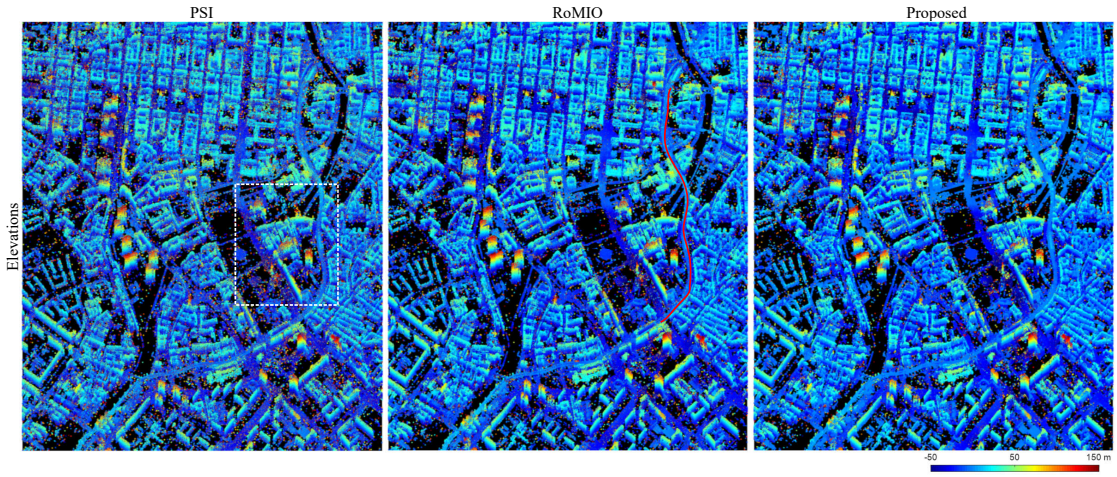

Figure 5.28: Estimated elevation maps by PSI, RoMIO and the proposed method with 15 interferograms of one area in Berlin. Besides the reconstruction of flat areas as Las Vegas, the proposed method can also achieve the robust retrieval of this complex area composed by building blocks and high-rise buildings. For a better comparison of the three methods, one zoom-in area and one road profile are displayed in Figure 5.29 and 5.31, respectively.

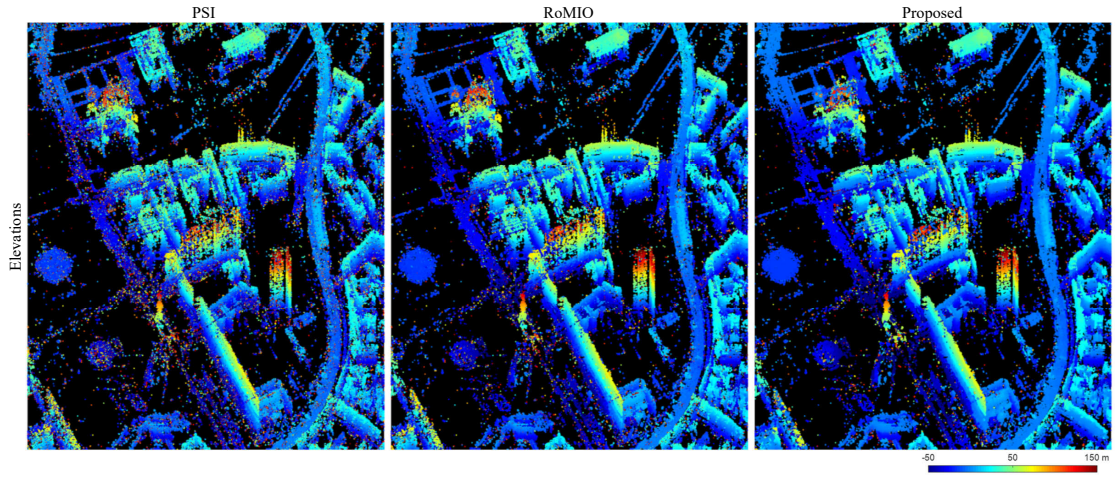

Figure 5.29: The cropped zoom-in areas of the results in Figure 5.28 by the dashed white rectangular. Compared to PSI, most outliers can be mitigated by the tensor-decomposition-based methods.

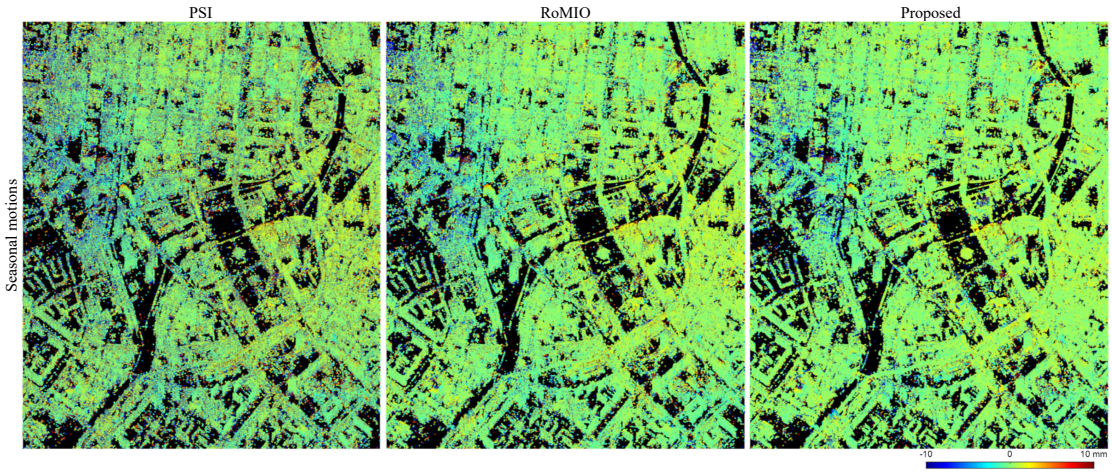

Figure 5.30: Estimated amplitudes of seasonal motions by PSI, RoMIO and the proposed method with 15 interferograms of one area in Berlin. Smoothness structure can be well maintained in the reconstructed deformation map by the proposed method.

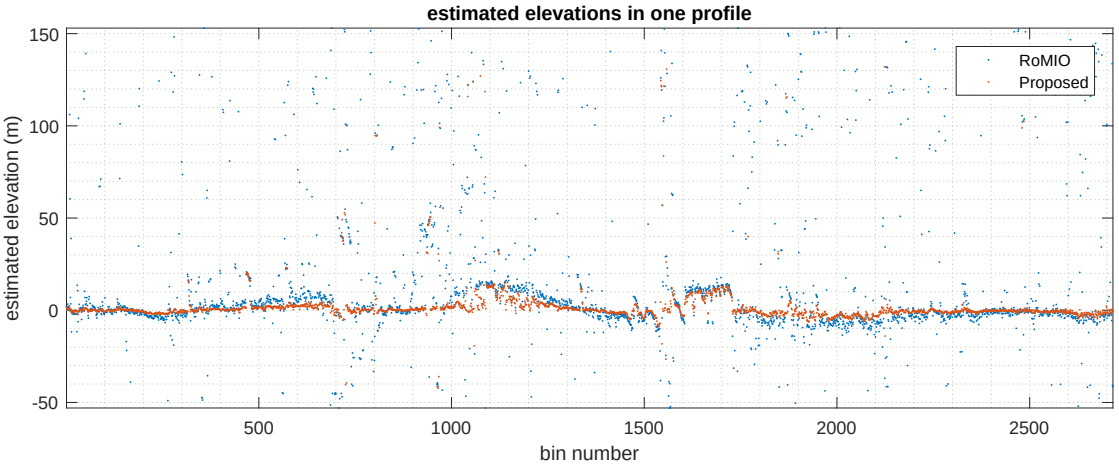

Figure 5.31: The extracted elevation profiles from the results shown in 5.28 (indicated by red curve). Obviously, the proposed TV regularized tensor decomposition method can better preserve piecewise smoothness for the 3D reconstruction of roads than RoMIO.

Table 5.4: Quantitative study for the results of Berlin data. The parameters estimated by the proposed method on the full InSAR stack were regarded as the reference, in order to compare the results of the three methods applying on a smaller InSAR stack with 15 interferorgams.

	Deformation [mm]		Elevation [m]	
	SD	bias	SD	bias
PSI	4.45	−0.06	36.04	10.94
RoMIO	2.87	**0.02**	23.66	4.30
Proposed	**0.80**	0.03	**5.26**	**−0.06**

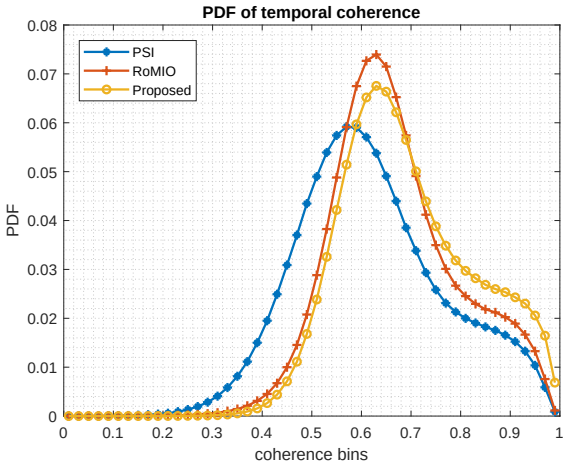

Figure 5.32: PDF of temporal coherence based on the estimated results by PSI and the proposed methods

tively.

From the study area shown in Figure 5.26, it is mainly composed by building blocks and high-rise buildings. As demonstrated in Figure 5.28 and one zoom-in area in Figure 5.29, more outliers appear in the 3D reconstruction by PSI than RoMIO and the proposed method. Compared to RoMIO, the proposed method can better reconstruct road areas, since smoothness structure is able to be preserved by TV regularization. As an example shown in Figure 5.28 (Middle), one road profile indicated by the red curve is extracted from the results of RoMIO and the proposed method, respectively, and displayed in Figure 5.31. Obviously, piecewise smooth property can be better maintained in the proposed method than RoMIO. Moreover, Figure 5.30 shows that the proposed method can produce the smoothest map of deformations than RoMIO and PSI, which indicates that incorrectly estimates can be mitigated by the proposed method. Consistent with the previous experiment, the filtered InSAR stack by the proposed method can best fit the model among the three comparing methods, which is displayed by the histograms of temporal coherences in Figure 5.32. Besides, the numerical analysis is done in the same manner as the above experiment. As illustrated in Table 5.4, the estimates from the proposed method are much closer than the other two methods given the estimates from the full stack.

5.5 Discussion

This chapter studied the low rank property of object-based InSAR phase stacks and proposed RoMIO. RoMIO can be combined with conventional multibaseline InSAR techniques to improve the estimation accuracy of geophysical parameters. Taking PSI as an example, the chapter demonstrated that in typical condition of very high resolution spaceborne InSAR data, e.g. object size of 10m, 5dB SNR and $10-20$ SAR images, the proposed approach can improve the estimation accuracy of geophysical parameters by a factor of ten to thirty, especially in the presence of outliers. These merits can in turn efficiently reduce the number of

SAR images for a reliable estimation.

Based on the experiments, the spatial sizes of tensors can influence the efficiency of the proposed method. On one hand, with large spatial sizes, the low rank property of the phase tensor is generally more prominent, which gives a wide operable range of the regularization parameters in the optimization. But, over-smoothing artifacts may exist, especially in some geometrically complex areas. On the other hand, with small spatial sizes, although it can be a benefit for preserving small detail, the regularization parameters must be carefully tuned. Otherwise, the reconstructed phase tensor may have the risk to be turned into a rank-1 tensor. Therefore, the tensor size should be large enough to promote low-rankness of the true phase and the sparsity of outliers, but small enough to exclude complicated structures. According to the experiments in the chapter, the typical patch size utilized is around 100×100 pixels, and this can be improved by exploiting adaptive window.

Besides, the proposed approach is suitable for operational processing, as the only parameter that needs to be tuned, i.e. α, was shown to usually lie in the range from 1×10^{-3} to 1×10^{-1} based on both the simulated and real data experiments. Besides, the approach can easily be parallelized by carrying it out patch-wisely.

Furthermore, a novel tensor decomposition method in complex domain based on the prior knowledge of the low rank property and smoothness structure in multibaseline InSAR data stacks is also proposed in this chapter. By integrating TV into the tensor decomposition model, the estimation of geophysical parameters based on the proposed method can be future improved than RoMIO. The proposed method introduces three parameters to be set, i.e. α, β and γ. They do not need to be tuned simultaneously, since one parameter can be set as a constant and adjust the other two with respect to it. Based on the experiments, γ can be selected as a constant of $100/\sqrt{I_1 I_2}$, the optimal α lies in the range from 0 to 10, and the optimal β can be selected from 0 to 0.2. From the results of the real data, the proposed method is not only favorable for 3D reconstruction of flat urban areas, such as Las Vegas, but also promising for complicated European cities, such as Berlin. Moreover, for large-scale processing, the proposed method can be easily parallelized and operated in a sliding window manner.

6 Robust low rank tensor decomposition for Distributed Scatterer

Multibaseline InSAR techniques, such as PSI and TomoSAR, have been the workhorse for deformation monitoring and 3-D reconstruction. However, because of the moderate SNR of spaceborne SAR images, as well as the property of the estimators, e.g. periodogram, employed in those techniques, they usually require a fairly large stack of SAR images (usually in the order of tens), in order to achieve a reliable estimate of the parameters. This renders them costly and sometimes infeasible for large-area processing. This challenge has been tackled by low rank phase tensor decomposition in the previous chapters. However, when it comes to DS, its stochastic nature and the correlation among interferograms are not considered in low rank decomposition. Directly applying low rank decomposition on DS InSAR phase stacks does not lead to the reliable results as applying on PS. Therefore, in this chapter, an extension of robust low rank tensor decomposition to DS InSAR phase tensors is proposed. In Section 6.1, optimal phase history retrieval for DS based on phase linking technique is first introduced. Then, the proposed pipeline for DS processing is demonstrated in Section 6.2. Simulated and real experiments are conducted in Section 6.3. At last, a short discussion of this chapter is in Section 6.4.

6.1 Phase linking

In non-urban areas, such as mountains, multibaseline SAR data vector at a given pixel can be modeled with the zero-mean, multi-dimensional circular complex Gaussian distribution as introduced in Equation (2.9). Typically, in order to estimate the corresponding covariance matrix $\mathbf{C}$, SHP are adaptively selected via statistical similarity test such as KS [Fer+11] or AD test [WZB12]. Then, $\mathbf{C}$ can be estimated by the sample mean of SHPs:

$$\hat{\mathbf{C}} = \frac{1}{M} \sum_{p \in \Omega} \mathbf{g}_p \mathbf{g}_p^H, \tag{6.1}$$

where Ω denotes the set of SHPs with respect to the pixel. In order to retrieve the absolute phase history with respect to the master image given $\hat{\mathbf{C}}$, phase triangulation methods, such as MLE or eigenvalue-decomposition, have been proposed in [CLJ16; Fer+11; For+15; ADZB17].

Recently, a phase triangulation method based on ILS estimator was proposed in [SE+16]. As pointed out by [SE+16], ILS can achieve more accurate performance than MLE, given the estimated covariance matrix $\hat{\mathbf{C}}$, since the small numerical biases in coherence matrix estimation can be amplified during the matrix inversion required by MLE [ADZB17]. By introducing integer ambiguity term $a_{nm} \in \{-1, 0, 1\}$, all the $\frac{N(N-1)}{2}$ wrapped interferometric phases ϕ_{nm}

of $\hat{\mathbf{C}}$ can be modeled in a linear form by:

$$\mathbb{E}(\phi_{nm}) = \begin{cases} \varphi_{0m} - \varphi_{0n} + a_{nm}(2\pi) & \text{if } n,m \neq 0 \\ \varphi_{0m} & \text{if } n = 0 \\ -\varphi_{0n} & \text{if } m = 0 \end{cases}, \tag{6.2}$$

and its matrix notation can be represented as:

$$\begin{aligned} \mathbb{E}\left\{ \underbrace{\begin{bmatrix} \varphi_{01} \\ \vdots \\ \varphi_{0(N-1)} \\ \vdots \\ \varphi_{nm} \\ \vdots \\ \varphi_{(N-2)(N-1)} \end{bmatrix}}_{\mathbf{y}} \right\} &= \underbrace{\begin{bmatrix} 0 & \dots & 0 \\ \vdots & \ddots & \vdots \\ 0 & \dots & 0 \\ 2\pi & & \\ & \ddots & \\ & & 2\pi \end{bmatrix}}_{\mathbf{A}} \underbrace{\begin{bmatrix} a_{12} \\ \vdots \\ a_{nm} \\ \vdots \\ a_{(N-2)(N-1)} \end{bmatrix}}_{\mathbf{a}} \\ &+ \underbrace{\begin{bmatrix} 1 & & & \\ & \ddots & & \\ & & 1 & \\ & \vdots & & \\ & -1 \dots 1 & & \\ & \vdots & & \\ & & -1 & 1 \end{bmatrix}}_{\mathbf{B}} \underbrace{\begin{bmatrix} \varphi_{01} \\ \vdots \\ \varphi_{0(N-1)} \end{bmatrix}}_{\mathbf{b}} \end{aligned}, \tag{6.3}$$

where n and m ($n = 1 \dots (N-2),\ m = 2 \dots (N-1)$) denote the radar image indices, $\mathbb{E}(\mathbf{y}) \in \mathbb{R}^{\frac{N(N-1)}{2}}$ is the vector of all multi-look wrapped interferometric phases φ_{nm} , $\mathbf{A}$ and $\mathbf{B}$ are the two design matrices, $\mathbf{a} \in \mathbb{Z}^{\frac{N^2-3N+2}{2}}$ and $\mathbf{b} \in \mathbb{R}^{N-1}$ are the integer and real unknown parameters to be estimated. The solution of (6.3) can be given by solving the following weighted ILS problem:

$$\hat{\mathbf{a}}, \hat{\mathbf{b}} = \underset{\mathbf{a}\in\mathbb{Z}, \mathbf{b}\in\mathbb{R}}{\operatorname{argmin}} \|\mathbb{E}(\mathbf{y}) - \mathbf{A}\mathbf{a} - \mathbf{B}\mathbf{b}\|^2_{\mathbf{W}}, \tag{6.4}$$

where $\mathbf{W}$ denotes the weight matrix and $\|\cdot\|^2_{\mathbf{W}} := (\cdot)^H \mathbf{W} (\cdot)$ is the associated quadratic norm. $\mathbf{W}$ can be selected as a generic weight matrix defined by the *Fisher information* index [Ric03].

Based on such procedure, the deterministic signal can be retrieved from SHPs. Afterwards, the optimal complex phase history $\hat{\mathbf{g}}$, i.e. $\hat{\mathbf{g}} = \exp(j\hat{\mathbf{b}})$ can be exploited as the input for robust low rank tensor decomposition.

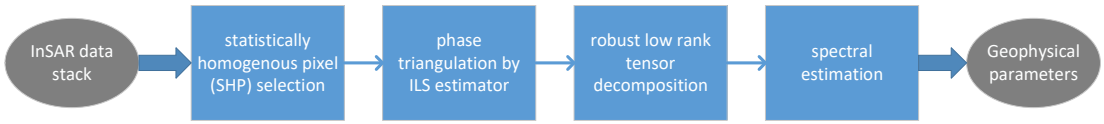

Figure 6.1: The overall workflow for applying robust tensor low rank tensor decomposition on DS.

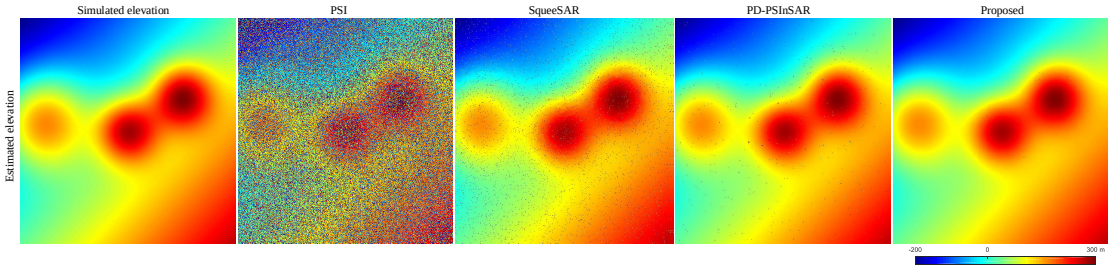

Figure 6.2: Simulated ground truth elevation map and the estimated results by PSI, SqueeSAR and the proposed method. By performing adaptive filtering, SqueeSAR can mitigate most of the incorrectly estimated points. This is mainly because of the pixels are simulated according to a perfect DS model which allows an optimal performance of the homogeneous sample selection via AD test. However, it can be still seen that noisy points exist in the result from SqueeSAR, which is mainly due to the outliers. By exploiting likelihood ratio test of coherence matrices for identifying homogeneous patches, PD-PSInSAR can also take effect on mitigating outliers, while some outliers still present in the result. As a comparison, most pixels can be correctly estimated and around 87% estimates can reach errors less than $1(m)$.

6.2 Processing pipeline for Distributed Scatterer

To this end, as extension of the proposed method to DS, a novel framework for geophysical parameter reconstruction based on robust low rank tensor decomposition is introduced. It mainly contains two parts: optimal phase history retrieval for DS by multi-looking and phase-linking, and the follow-up robust phase tensor decomposition. In particular, the proposed workflow can be illustrated in Figure 6.1 and described as follows:

1) SHP utilized for multi-looking are selected by AD test to calculate the sample covariance matrix.

2) The phase history of each pixel can be then retrieved by ILS estimator.

3) Apply robust low rank tensor decomposition to the retrieved phase tensor.

4) Reconstruct geophysical parameters based on the outlier-free InSAR phase stacks via spectral estimation methods, such as periodogram.

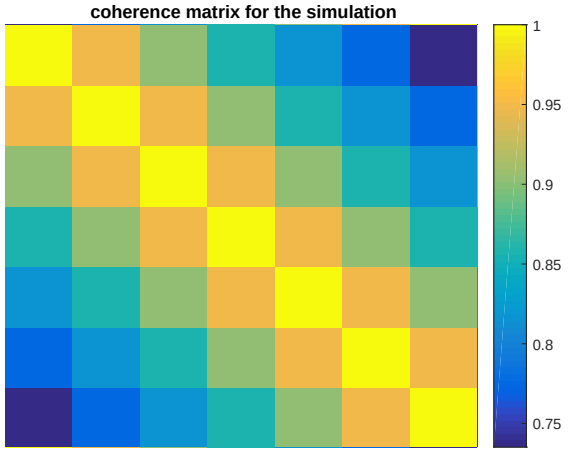

Figure 6.3: Coherence matrix for DS simulation.

Table 6.1: Percentages of reliable estimates shown in Figure 6.2

Residual error <= 1m	PSI	SqueeSAR	PD-PSInSAR	Proposed
Percentages	20.76%	61.63%	80.91%	87.15%

Table 6.2: Numerical analysis of the results shown in Figure 6.2

	PSI	SqueeSAR	PD-PSInSAR	Proposed
SD [m]	195.90	32.06	10.76	2.50
mean [m]	-31.36	-1.13	-0.16	-0.02

6.3 Validation

6.3.1 Simulation

A multibaseline InSAR phase stack of 512 × 512 pixels by 7 images with the elevation pattern shown in Figure 6.2 (Left) is simulated. The spatial baseline was chosen to be similar as TanDEM-X bistatic interferograms used for DEM generation, i.e. 40-60m. DS were generated from the ground truth phase with the coherence matrix as illustrated in Figure 6.3. Also, sparse outliers were added to the stack by randomly replacing 30% of pixels from the stack with uniformly distributed phases. The elevations were estimated by PSI, SqueeSAR, PD-PSInSAR [CLJ16] and the proposed method. A visual comparison of their results are shown in Figure 6.2. In both SqueeSAR and the proposed method, the threshold of AD test and boundary size for SHP selection were kept identically. For identifying homogeneous patches in PD-PSInSAR, the threshold for log likelihood ratio test is designed as -18. The low rank decomposition in the proposed method was processed in a sliding window manner with the patch size of 200 × 200 pixels. For setting γ, γ can be rewritten as $\gamma = \alpha \times \lambda_*$, where a good choice for λ_* can be set as $\frac{1}{\sqrt{\max(W,N)}}$ according to [Can+11; GQ14], and α is a factor for tuning. α was set as 0.75 for this experiment. The detailed parameter setting of α is discussed in the following subsection. For a quantitative analysis, the percentages of the reliable estimates (residual error <= 1m) are displayed in Table 6.1. Moreover, the standard deviations and mean values of the residuals are calculated, given the ground truth elevation map and the associated numerical analysis is demonstrated in Table 6.2.

According to the results shown in Figure 6.2 and Table 6.1, only around 20% pixels can be correctly estimated. By performing adaptive filtering, SqueeSAR can mitigate most of the incorrectly estimated points. This is mainly because of the pixels are simulated according to a perfect DS model which allows an optimal performance of the homogeneous sample selection via statistical test. However, it can be still seen that noisy points exist in the result from SqueeSAR, which is mainly due to the outliers. By exploiting likelihood ratio test of coherence matrices for identifying homogeneous patches, PD-PSInSAR can also take effect on mitigating outliers, while some outliers still present in the result. As a comparison, most pixels can be correctly estimated and around 87% estimates can reach errors less than 1m. As demonstrated by the performance analysis in Table 6.2, the proposed method can outperform other methods by more than a factor of three to ten in the accuracy of the elevation estimates.

6.3.1.1 Parameter Selection

There are three parameters to be set in the proposed method, i.e. the window size W, the penalty parameter α and the introduced Lagrange multiplier parameter ρ in (4.33). As studied in [GQ14], ρ can be kept constant with the value $10 \times \text{std}(\text{vec}(\mathcal{G}))$, where $\text{std}(\cdot)$ is the standard deviation calculator. For testing the efficiency of the proposed method with respect to W and α, standard deviations of the elevation estimates with respect to different W (ranging from 16 to 256) and α (ranging from 0 to 1) are calculated and shown in Figure 6.4. It can be seen that the optimal α stably lies in between 0.7 and 0.8 for most patch sizes, which means that it does not need to be tuned much with different parameters of patch size. Moreover,

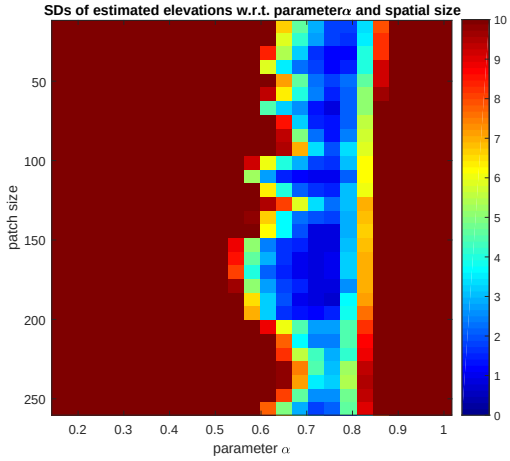

Figure 6.4: The efficiency study of the proposed method with respect to the choices of patch size and α. It can be seen that the optimal α stably lies in between 0.7 and 0.8 for most patch sizes, which means that it does not need to be tuned much with different parameters of patch size.

optimal patch size is around 200 for this simulation.

6.3.2 Application on 3D reconstruction of mountainous areas

For testing the proposed method on real data, experiments of two TanDEM-X InSAR stacks with 7 interferograms were performed. As illustrated in Figure 6.5, the first study area is shown by the mean amplitude image (log-scale) with the size of 900×1000 pixels and the corresponding optical image from Google Earth. It can be seen that this area mainly composes of big mountains and a long valley in-between. The reconstructed results of the heights by PSI, SqueeSAR, PD-PSInSAR and the proposed method are present in Figure 6.6. The parameter setting of AD test utilized in SqueeSAR and the proposed method was the same with the simulation. The threshold for log likelihood ratio test was set to -30 in PD-PSInSAR. For the proposed approach, the patch size and α were 300×300 pixels and 0.85, respectively. For a detailed comparison, the results of the zoom-in area on one mountain are displayed at the bottom row of Figure 6.6. Besides, the height profiles from the results are extracted and the associated zoom-in areas are shown in Figure 6.7 and Figure 6.8, correspondingly.

A larger mountainous area for testing is shown by the mean amplitude image (log-scale) and the corresponding optical image from Google Earth in Figure 6.9. The spatial size of this area is 1659×2000 pixels. This area is mainly composed of one relatively flat part on the left and rugged mountains on the right. Based on the elevations retrieved from the proposed method, the associated 3D model of this area can be constructed and displayed in Figure 6.10.

6.3.2.1 Performance Analysis

As shown in Figure 6.6, the performance of the three algorithm on real data is consistent with the simulation in the previous section. For most parts in the scene, PSI cannot reconstruct re-

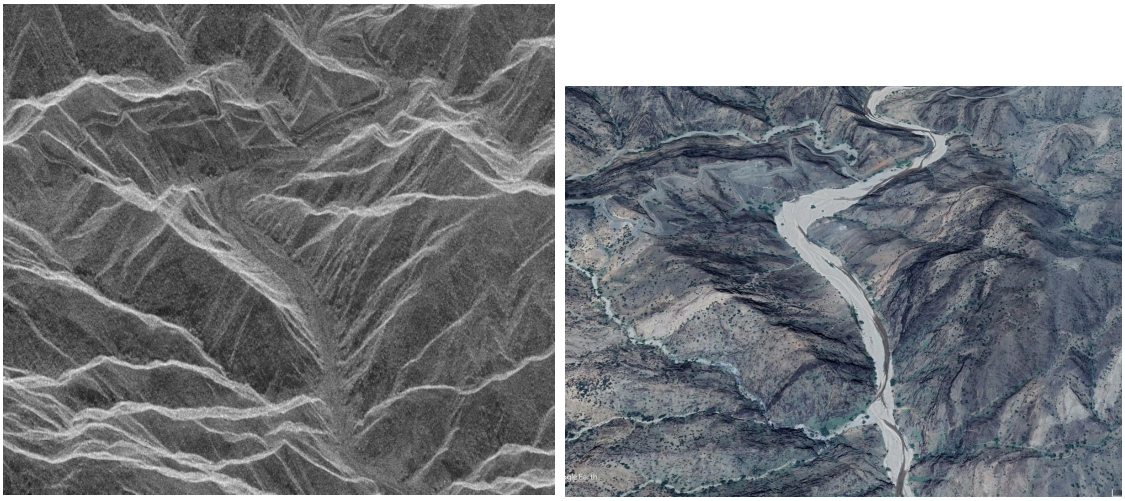

Figure 6.5: The first study mountain area of TanDEM-X dataset shown by the mean amplitude (log scale) and the corresponding optical image from Google Earth.

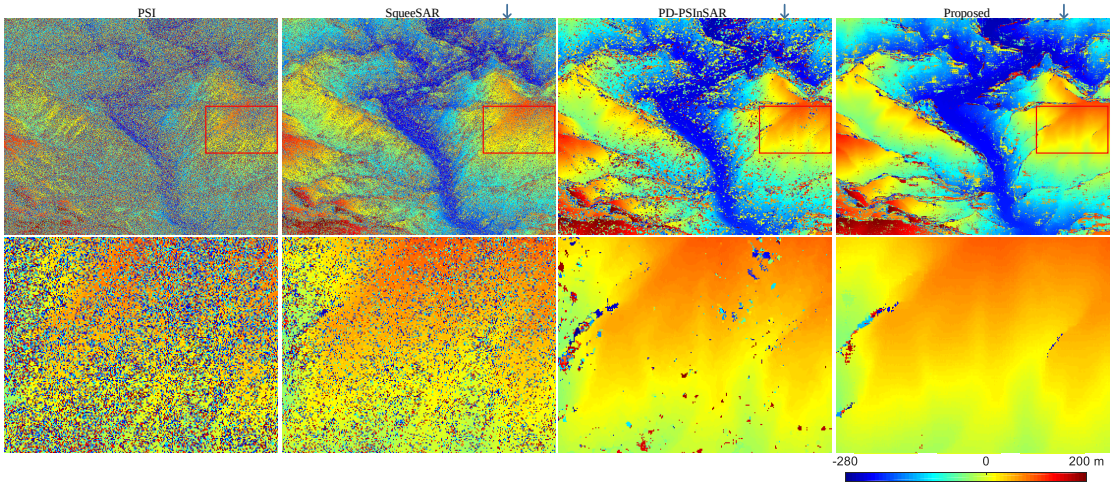

Figure 6.6: The elevation reconstruction results by PSI, SqueeSAR, PD-PSInSAR and the proposed method. For most parts in the scene, PSI cannot reconstruct reliable elevations from DSs. Although SqueeSAR can retrieve the elevations of most parts in the scene, many points are still incorrectly estimated. Not surprisingly, SqueeSAR does not perform as ideally as in the simulation, because many pixels do not perfectly follow a DS model. In comparison, the proposed method can robustly recover the height map of nearly the whole scene by efficiently exploit the neighborhood information using low rank tensor decomposition. Improvements are particularly prominent for the pixels on large slopes and on the valley. As shown from the zoom-in parts, the proposed method can demonstrate clearer pattern of height variation than the other methods.

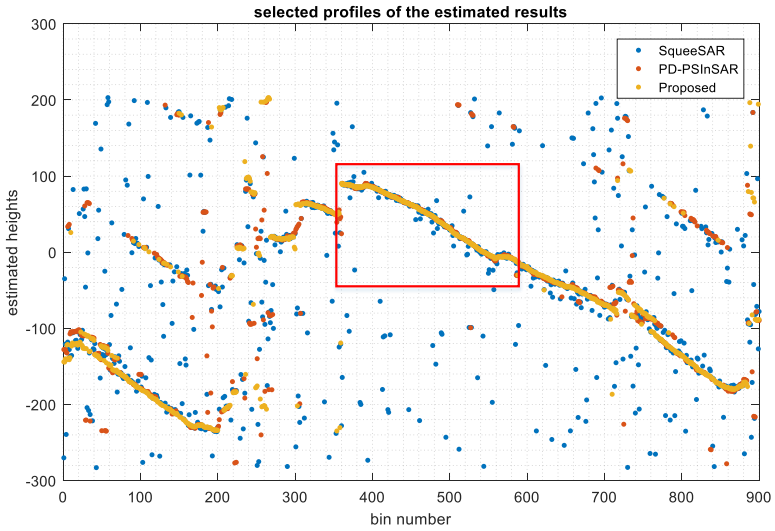

Figure 6.7: Plot of selected height profiles from the estimated results shown in Figure 6.6. It can be observed that the proposed method shows obviously much fewer outliers.

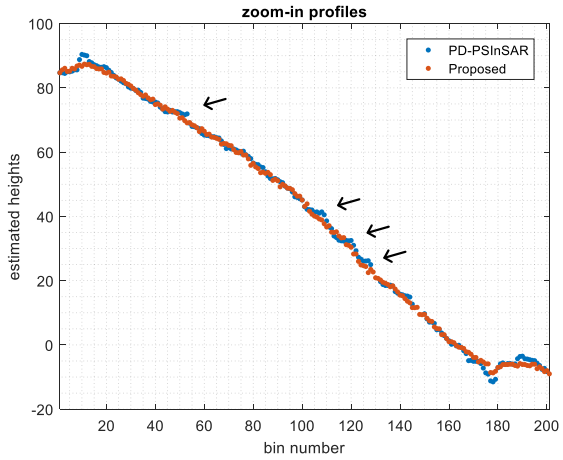

Figure 6.8: Zoom-in plot of the profiles from PD-PSInSAR and the proposed approach shown in Figure 6.7. In a detailed comparison with PD-PSInSAR, it can be indicated that staircasing may exist in the result of PD-PSInSAR, as pointed out by the black arrows. As a comparison, the proposed method can better avoid that phenomenon.

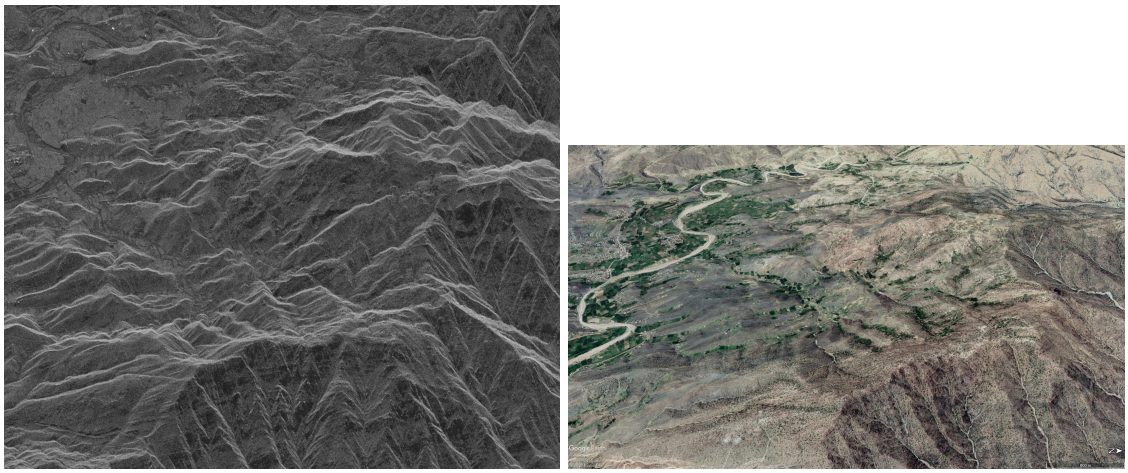

Figure 6.9: The second study mountain area of TanDEM-X dataset shown by the mean amplitude (log scale) and the corresponding optical image from Google Earth.

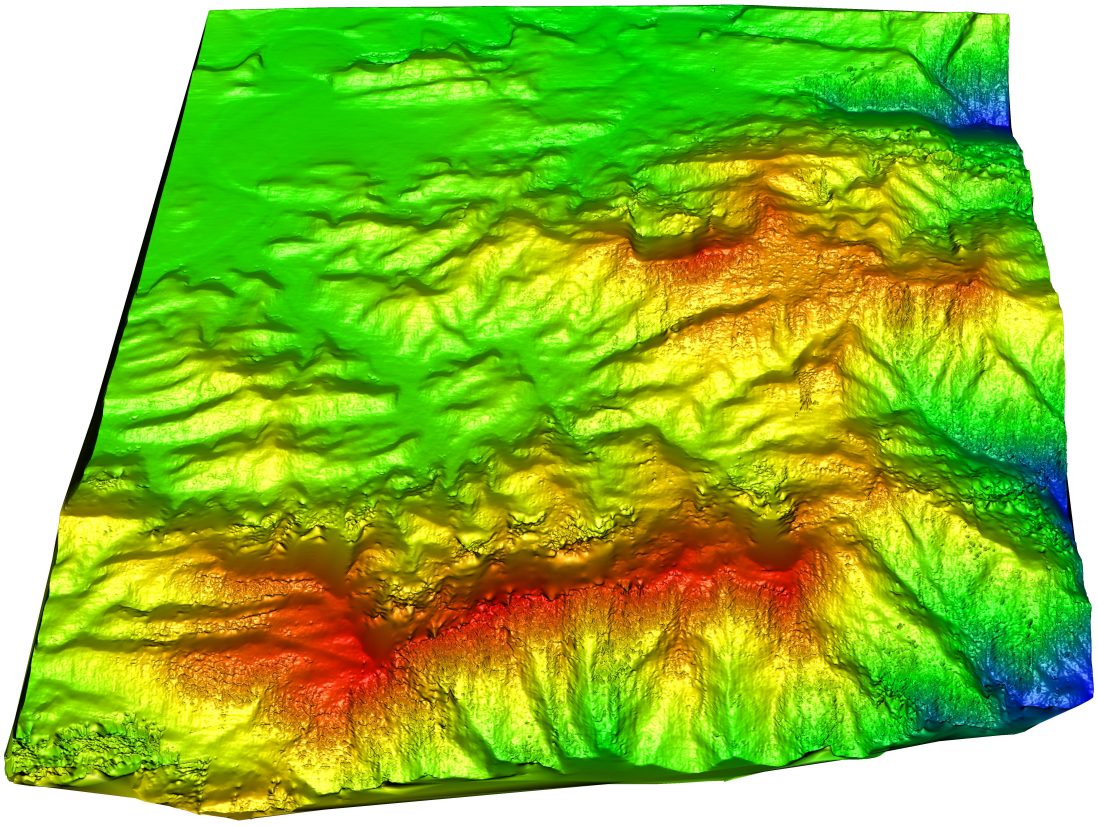

Figure 6.10: The final 3D reconstruction based on the result of the proposed method for the area of the second dataset. Contours of mountainous areas and the sinuous river lying on the plain area can be clearly seen in the result, which indicates that the over-smoothness does not happen in the proposed method.

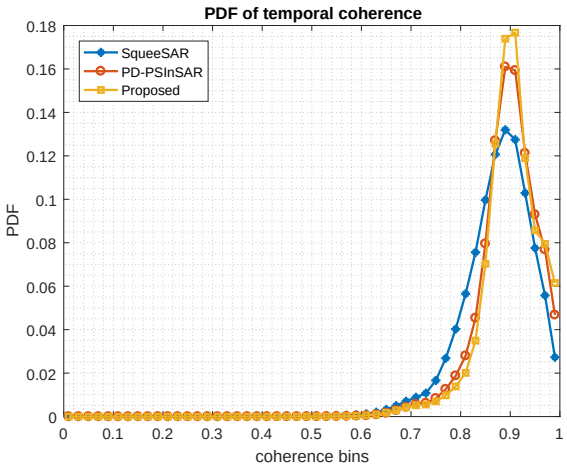

Figure 6.11: Probability density functions of temporal coherences obtained from the three comparing methods. Most points can achieve a temporal coherence above 0.8 in all the three methods. The proposed method sightly outperforms the other two methods.

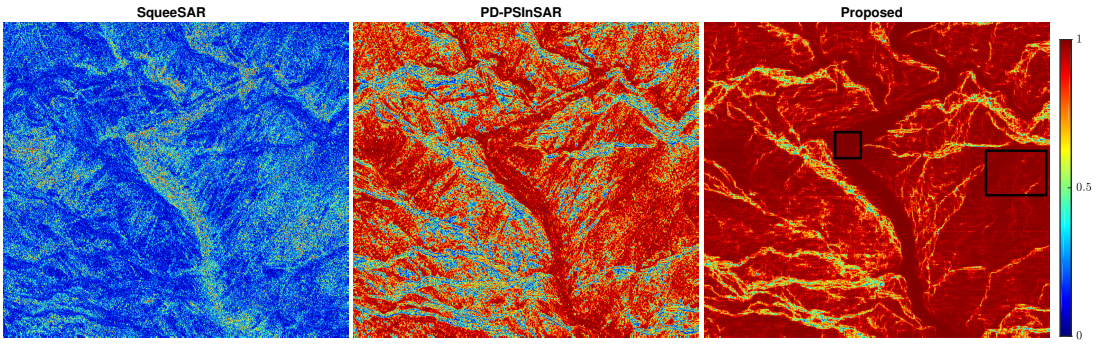

Figure 6.12: Temporal colinearity maps of the comparing methods. As the cropped areas (black rectangles) for example, the proposed method can achieve the best homogeneity among the comparing methods. Correspondingly, it can be observed that the elevation changes of such areas in the optical image (Figure 6.5) are smooth. In turn, to some extent, temporal colinearity can reflect the quality of the filtered multibaseline InSAR phases.

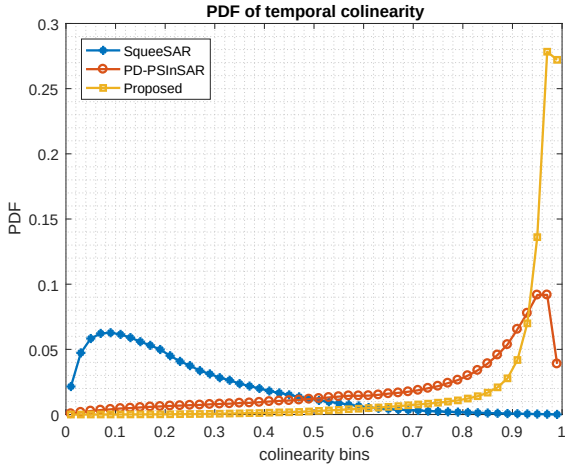

Figure 6.13: Probability density functions of temporal colinearity from the three methods. The best homogeneity of the filtered InSAR phase time-series can be obtained by the proposed method. In consistence with the height reconstruction in Figure 6.6, the incorrectly estimated points can severely influence the quality of temporal colinearity assessment.

liable elevations from DSs. Although SqueeSAR can retrieve the elevations of most parts in the scene, many points are still incorrectly estimated. Not surprisingly, SqueeSAR does not perform as ideally as in the simulation, because many pixels do not perfectly follow a DS model. In comparison, the proposed method can robustly recover the height map of nearly the whole scene by efficiently exploit the neighborhood information using low rank tensor decomposition. Improvements are particularly prominent for the pixels on large slopes and on the valley. As shown from the zoom-in parts, the proposed method can demonstrate clearer pattern of height variation than the other methods. In addition, Figure 6.7 shows two height profiles (pointed out by the blue arrow in Figure 6.6 from the three comparing results. It can be observed that the proposed method shows obviously much fewer outliers. In a detailed comparison with PD-PSInSAR, the zoom-in profiles illustrated in Figure 6.8 indicate that staircasing may exist in the result of PD-PSInSAR, as pointed out by the black arrows. As a comparison, the proposed method can better avoid that phenomenon.

Besides the visual inspection, two metrics are furthermore explored for the analysis of the comparing reconstruction results: *Temporal Coherence* and *Temporal Colinearity* proposed in this chapter.

1) Temporal Coherence: Temporal coherence [FPR01; Fer+11; ADZB17] is widely exploited for measuring the fitness between the observed and estimated InSAR phase time-series.

As shown in Figure 6.11, the histograms of temporal coherence based on the comparing methods for the first study area are displayed.

2) Temporal Colinearity: Based on the colinearity criterion introduced in [PPMA12], it can be extended from evaluating one interferogram to InSAR phase time-series, called as *Tempo-*

ral Colinearity. The corresponding formula is as represented as follows:

$$C_i = \frac{|\sum_{p\in M_i} \exp(j\boldsymbol{\phi}_i)^H \exp(j\boldsymbol{\phi}_p)|}{N(M^2-1)} \times \frac{\sum_{p\in M_i} |\exp(j\boldsymbol{\phi}_i)^H \exp(j\boldsymbol{\phi}_p)|}{N(M^2-1)}, \tag{6.5}$$

where i is the index of the pixel to be assessed, $p \in M_i$ denotes the close neighborhood pixels surrounding the ith pixel, the local window size M is set as 3 in this chapter and $|\cdot|$ denotes the absolute value of the complex number. This criterion measures the similarity of the phase history of the study pixel with respect to its surrounding ones. It is a measurement of homogeneity or smoothness given the neighboring pixels of InSAR phase stacks. Higher values indicate the better homogeneity of the filtered InSAR phase time-series. To some extent, it can be regarded as a quality assessment for multibaseline InSAR phase stacks, especially for the areas with homogeneous geophysical parameters.

As presented in Figure 6.11, most points can achieve a temporal coherence above 0.8 in all the three methods. The proposed method sightly outperforms the other two methods. However, the temporal colinearity map and the corresponding histograms of Figure 6.12 and 6.13 show that the best homogeneity of the filtered InSAR phase time-series can be obtained by the proposed method. In consistence with the height reconstruction in Figure 6.6, the incorrectly estimated points can severely influence the quality of temporal colinearity assessment. As the cropped areas (black rectangles) in Figure 6.12 for example, the proposed method can achieve the best homogeneity among the comparing methods. Correspondingly, it can be observed that the elevation changes of such areas in the optical image (Figure 6.5) are smooth. In turn, to some extent, temporal colinearity can reflect the quality of the filtered multibaseline InSAR phases. However, there are still pixels which cannot be correctly estimated in the result of the proposed method, especially along the contour lines of mountains. This is mainly due to the layover effect in those areas and it can be mitigated by using higher order spectral estimator like tomographic inversion.

6.4 Discussion

In this chapter, a novel method for 3D reconstruction in complex mountainous areas based on the low rank property inherent in the complex InSAR data stack is proposed. According to the simulated experiments under typical settings, the proposed method can achieve reliable estimates even with a limited number of SAR images (less than ten) and outperforms the state-of-the-art methods such as PD-PSInSAR and SqueeSAR by a factor of more than two in terms of the accuracy of the height estimates.

According to the experiments, the proposed method is insensitive to the parameter selection. There are totally two parameters to be tuned for performing the proposed low rank tensor decomposition, i.e. the patch size W and the penalty parameter α. According to the simulations, the optimal α is found to be stable in a certain range, regardless of different settings of patch size W. In other words, the two parameters can be independently tuned. Besides, based on the experiments, the proposed approach is suitable for operational processing on large areas, as it can be easily parallelized by carrying out patch-wisely to avoid highly computational costs induced by the low rank decomposition of large 3D tensors.

7 Conclusion

7.1 Summary

In a summary, this thesis investigates the potential possibilities of advanced algorithm development for geophysical parameter retrieval from InSAR data stacks based on object level.

- A general framework for object-based multibaseline InSAR parameter estimation, i.e., introducing a spatial regularization term (TV or TGV) based on given object labels, is proposed. Correspondingly, the optimization ADMM solver is introduced. Moreover, considering the significant amount of outliers existing in real data, a robust InSAR stack filtering approach is introduced by minimizing the rank of the InSAR stack tensor. To demonstrate the application of the proposed method for bridge monitoring, a bridge detection method in optical images is also proposed. The proposed approach with robust phase recovery is proven to be effective against outliers. It outperforms the non-robust pixel-wise approach by a factor of twenty in terms of the standard deviation of the estimates, at 5 dB SNR with an outliers percent of 30%. Also, it achieves more reliable results than the one without the robust phase recovery step.

- Moreover, the low rank property of object-based InSAR phase stacks is investigated and RoMIO is proposed in Chapter 5. RoMIO can be combined with conventional multi-baseline InSAR techniques to improve the estimation accuracy of geophysical parameters. Taking PSI as an example, the thesis demonstrated that in typical condition of very high resolution spaceborne InSAR data, e.g. object size of 10m, 5dB SNR and $10-20$ SAR images, the proposed approach can improve the estimation accuracy of geophysical parameters by a factor of ten to thirty, especially in the presence of outliers. These merits can in turn efficiently reduce the number of SAR images for a reliable estimation. Furthermore, a novel tensor decomposition method in complex domain based on the prior knowledge of the low rank property and smoothness structure in multi-baseline InSAR data stacks is also proposed in this chapter. By integrating TV into the tensor decomposition model, the estimation of geophysical parameters based on the proposed method can be future improved than RoMIO.

- As the extension for DS processing, a novel method for 3D reconstruction in complex mountainous areas based on the low rank property inherent in the complex InSAR data stack is proposed. According to the simulated experiments under typical settings, the proposed method can achieve reliable estimates even with a limited number of SAR images (less than ten) and outperforms the state-of-the-art methods such as PD-PSInSAR and SqueeSAR by a factor of more than two in terms of the accuracy of the height estimates.

7.2 Outlook

There exist several aspects to further the research conducted as part of this thesis.

Atmosphere signal removal

The atmosphere signal behavior is partly satisfied to the proposed tensor-decomposition based models, i.e. spatially correlated and temporally uncorrelated, it would be interesting to systematically investigate the performance of atmosphere signal removal based on such tensor-decomposition based method.

Improvement of land-cover classification based on time-series SAR images

This thesis demonstrates that the proposed methods can effectively improve the geophysical parameter estimation. In other words, the geophysical feature inherent in time-series SAR images can be enhanced by the proposed methods. Moreover, [D+18] systematically investigates specific TomoSAR features can be exploited for land-cover classification. Therefore, it would be interesting to further research on the potential improvement of time-series SAR image filtering methods for land-cover classification.

3D TomoSAR point cloud inpainting

In principle, the methods proposed in this these can be considered as "inpainting" technologies for multidimensional data set. One of the most important advantages of InSAR processing is to reconstruct large-scale 3D point clouds in urban areas. It would be also interesting to research on 3D point cloud inpainting problem based on different kinds of prior knowledge, e.g. smoothness or semantic consistence. Other sources of information, such as the semantic information from optical images can be a plus to tackle this problem.

Joint geophysical parameter reconstruction on graphs

The methods proposed in this thesis are based on tensor model, where similarity between pixels belonged to different objects is not considered. After all, pixels on different urban objects cannot be given the same weight in the optimization procedure. The similarity between pixels of multibaseline InSAR data stacks can be further studied and integrated into the joint geophysical parameter reconstruction, which leads to the optimization problem on graphs, such as graph TV problem.

Bibliography

[Ada+03] Nico Adam, Bert Kampes, Michael Eineder, Jirathana Worawattanamateekul, and Michaela Kircher. "The development of a scientific permanent scatterer system". In: *ISPRS Workshop High Resolution Mapping from Space, Hannover, Germany*. Vol. 2003. 2003, p. 6 (cit. on p. 15).

[ADZB17] Homa Ansari, Francesco De Zan, and Richard Bamler. "Sequential Estimator: Toward Efficient InSAR Time Series Analysis". In: *IEEE Transactions on Geoscience and Remote Sensing* 55.10 (2017), pp. 5637–5652 (cit. on pp. 29, 87, 97).

[ADZB18] Homa Ansari, Francesco De Zan, and Richard Bamler. "Efficient Phase Estimation for Interferogram Stacks". In: *IEEE Transactions on Geoscience and Remote Sensing* (2018) (cit. on p. 30).

[Bai18] Gerald Norbert Baier. "Nonlocal Filtering for Single-and Multibaseline SAR Interferometry". PhD thesis. Technische Universität München, 2018 (cit. on p. 39).

[Bar07] Richard G Baraniuk. "Compressive sensing [lecture notes]". In: *IEEE signal processing magazine* 24.4 (2007), pp. 118–121 (cit. on p. 31).

[BCP13] Liliana Borcea, Thomas Callaghan, and George Papanicolaou. "Synthetic aperture radar imaging and motion estimation via robust principal component analysis". In: *SIAM Journal on Imaging Sciences* 6.3 (2013), pp. 1445–1476 (cit. on p. 57).

[Ber+02] Paolo Berardino, Gianfranco Fornaro, Riccardo Lanari, and Eugenio Sansosti. "A new algorithm for surface deformation monitoring based on small baseline differential SAR interferograms". In: *IEEE Transactions on Geoscience and Remote Sensing* 40.11 (2002), pp. 2375–2383 (cit. on pp. 28, 29).

[BES11] Alessandra Budillon, Annarita Evangelista, and Gilda Schirinzi. "Three-dimensional SAR focusing from multipass signals using compressive sampling". In: *IEEE Transactions on Geoscience and Remote Sensing* 49.1 (2011), pp. 488–499 (cit. on p. 31).

[BH98] Richard Bamler and Philipp Hartl. "Synthetic aperture radar interferometry". In: *Inverse problems* 14.4 (1998), R1 (cit. on pp. 19, 21, 23).

[BKP10] Kristian Bredies, Karl Kunisch, and Thomas Pock. "Total generalized variation". In: *SIAM Journal on Imaging Sciences* 3.3 (2010), pp. 492–526 (cit. on p. 41).

[Boy+11] Stephen Boyd, Neal Parikh, Eric Chu, Borja Peleato, Jonathan Eckstein, et al. "Distributed optimization and statistical learning via the alternating direction method of multipliers". In: *Foundations and Trends® in Machine learning* 3.1 (2011), pp. 1–122 (cit. on pp. 19, 25).

[Buc00] Sean Monroe Buckley. *Radar interferometry measurement of land subsidence*. 2000 (cit. on p. 19).

[Byr+95] Richard H Byrd, Peihuang Lu, Jorge Nocedal, and Ciyou Zhu. "A limited memory algorithm for bound constrained optimization". In: *SIAM Journal on Scientific Computing* 16.5 (1995), pp. 1190–1208 (cit. on p. 36).

[Cal+14] Francesco Caltagirone, A Capuzi, Alessandro Coletta, Giuseppe F De Luca, Edmondo Scorzafava, R Leonardi, Stefano Rivola, Sandro Fagioli, Giuseppe Angino, Michelangelo L'Abbate, et al. "The COSMO-SkyMed dual use Earth observation program: Development, qualification, and results of the commissioning of the overall constellation". In: *IEEE Journal of Selected Topics in Applied Earth Observations and Remote Sensing* 7.7 (2014), pp. 2754–2762 (cit. on pp. 3, 5, 15, 31).

[Can+11] Emmanuel J Candès, Xiaodong Li, Yi Ma, and John Wright. "Robust principal component analysis?" In: *Journal of the ACM (JACM)* 58.3 (2011), p. 11 (cit. on pp. 57, 68, 91).

[CCS10] Jian-Feng Cai, Emmanuel J Candès, and Zuowei Shen. "A singular value thresholding algorithm for matrix completion". In: *SIAM Journal on Optimization* 20.4 (2010), pp. 1956–1982 (cit. on p. 45).

[CH16] Gong Cheng and Junwei Han. "A survey on object detection in optical remote sensing images". In: *ISPRS Journal of Photogrammetry and Remote Sensing* 117 (2016), pp. 11–28 (cit. on p. 49).

[Cic+15] Andrzej Cichocki, Danilo Mandic, Lieven De Lathauwer, Guoxu Zhou, Qibin Zhao, Cesar Caiafa, and Huy Anh Phan. "Tensor decompositions for signal processing applications: From two-way to multiway component analysis". In: *IEEE Signal Processing Magazine* 32.2 (2015), pp. 145–163 (cit. on pp. 19, 23, 34, 58).

[CLJ15] Ning Cao, Hyongki Lee, and Hahn Chul Jung. "Mathematical framework for phase-triangulation algorithms in distributed-scatterer interferometry". In: *IEEE Geoscience and Remote Sensing Letters* 12.9 (2015), pp. 1838–1842 (cit. on p. 29).

[CLJ16] Ning Cao, Hyongki Lee, and Hahn Chul Jung. "A phase-decomposition-based PSInSAR processing method". In: *IEEE Transactions on Geoscience and Remote Sensing* 54.2 (2016), pp. 1074–1090 (cit. on pp. 15, 16, 29, 87, 91).

[Col+03] C Colesanti, A Ferretti, R Locatelli, and G Savio. "Multi-platform permanent scatterers analysis: first results". In: *Remote Sensing and Data Fusion over Urban Areas, 2003. 2nd GRSS/ISPRS Joint Workshop on*. IEEE. 2003, pp. 52–56 (cit. on p. 27).

[Cos+08] Mario Costantini, Salvatore Falco, Fabio Malvarosa, and Federico Minati. “A new method for identification and analysis of persistent scatterers in series of SAR images”. In: *Geoscience and Remote Sensing Symposium, 2008. IGARSS 2008. IEEE International*. Vol. 2. IEEE. 2008, pp. II–449 (cit. on p. 27).

[Cos+14] Mario Costantini, Salvatore Falco, Fabio Malvarosa, Federico Minati, Francesco Trillo, and Francesco Vecchioli. “Persistent scatterer pair interferometry: approach and application to COSMO-SkyMed SAR data”. In: *IEEE Journal of Selected Topics in Applied Earth Observations and Remote Sensing* 7.7 (2014), pp. 2869–2879 (cit. on p. 15).

[CP11] Antonin Chambolle and Thomas Pock. “A first-order primal-dual algorithm for convex problems with applications to imaging”. In: *Journal of mathematical imaging and vision* 40.1 (2011), pp. 120–145 (cit. on p. 35).

[CQ11] Guangyi Chen and Shen-En Qian. “Denoising of hyperspectral imagery using principal component analysis and wavelet shrinkage”. In: *IEEE Transactions on Geoscience and remote sensing* 49.3 (2011), pp. 973–980 (cit. on p. 55).

[Cro+16] Michele Crosetto, Oriol Monserrat, María Cuevas-González, Núria Devanthéry, and Bruno Crippa. “Persistent scatterer interferometry: A review”. In: *ISPRS Journal of Photogrammetry and Remote Sensing* 115 (2016), pp. 78–89 (cit. on p. 28).

[CV99] Tony Chan and Luminita Vese. “An active contour model without edges”. In: *International Conference on Scale-Space Theories in Computer Vision*. Springer. 1999, pp. 141–151 (cit. on p. 49).

[CWB08] Emmanuel J Candes, Michael B Wakin, and Stephen P Boyd. “Enhancing sparsity by reweighted L1 minimization”. In: *Journal of Fourier analysis and applications* 14.5-6 (2008), pp. 877–905 (cit. on p. 61).

[DDT11] Charles-Alban Deledalle, Loïc Denis, and Florence Tupin. “NL-InSAR: Nonlocal interferogram estimation”. In: *IEEE Transactions on Geoscience and Remote Sensing* 49.4 (2011), pp. 1441–1452 (cit. on p. 63).

[Dek03] Rob J Dekker. “Texture analysis and classification of ERS SAR images for map updating of urban areas in the Netherlands”. In: *IEEE transactions on geoscience and remote sensing* 41.9 (2003), pp. 1950–1958 (cit. on p. 48).

[Del+15] Charles-Alban Deledalle, Loïc Denis, Florence Tupin, Andreas Reigber, and Marc Jäger. “NL-SAR: A unified nonlocal framework for resolution-preserving (Pol)(In) SAR denoising”. In: *IEEE Transactions on Geoscience and Remote Sensing* 53.4 (2015), pp. 2021–2038 (cit. on p. 29).

[Den+09] Loïc Denis, Florence Tupin, Jérôme Darbon, and Marc Sigelle. “Joint regularization of phase and amplitude of InSAR data: Application to 3-D reconstruction”. In: *IEEE Transactions on Geoscience and Remote Sensing* 47.11 (2009), pp. 3774–3785 (cit. on p. 35).

[DGH13] Olivier DHondt, Stéphane Guillaso, and Olaf Hellwich. “Iterative bilateral filtering of polarimetric SAR data”. In: *IEEE Journal of Selected Topics in Applied Earth Observations and Remote Sensing* 6.3 (2013), pp. 1628–1639 (cit. on p. 31).

[DHo+18] O. DHondt, C. López-Martínez, S. Guillaso, and O. Hellwich. “Nonlocal Filtering Applied to 3-D Reconstruction of Tomographic SAR Data”. In: *IEEE Transactions on Geoscience and Remote Sensing* 56.1 (2018), pp. 272–285. ISSN: 0196-2892. DOI: 10.1109/TGRS.2017.2746420 (cit. on p. 31).

[DL+94] L De Lathauwer, B De Moor, J Vandewalle, and Blind Source Separation by Higher-Order. “Singular value decomposition”. In: *Proc. EUSIPCO-94, Edinburgh, Scotland, UK*. Vol. 1. 1994, pp. 175–178 (cit. on p. 58).

[DLDMV00] Lieven De Lathauwer, Bart De Moor, and Joos Vandewalle. “A multilinear singular value decomposition”. In: *SIAM journal on Matrix Analysis and Applications* 21.4 (2000), pp. 1253–1278 (cit. on p. 58).

[DMFP09] Antonio De Maio, Gianfranco Fornaro, and Antonio Pauciullo. “Detection of single scatterers in multidimensional SAR imaging”. In: *IEEE Transactions on Geoscience and Remote Sensing* 47.7 (2009), pp. 2284–2297 (cit. on pp. 15, 33).

[Don06] David L Donoho. “Compressed sensing”. In: *IEEE Transactions on information theory* 52.4 (2006), pp. 1289–1306 (cit. on p. 31).

[DR+58] Wilbur B Davenport, William L Root, et al. *An introduction to the theory of random signals and noise*. Vol. 159. McGraw-Hill New York, 1958 (cit. on p. 21).

[DZLD11] Francesco De Zan and Paco López-Dekker. “SAR image stacking for the exploitation of long-term coherent targets”. In: *IEEE Geoscience and Remote Sensing Letters* 8.3 (2011), pp. 502–506 (cit. on p. 29).

[D+18] Olivier D’Hondt, Ronny Hänsch, Nicolas Wagener, and Olaf Hellwich. “Exploiting SAR Tomography for Supervised Land-Cover Classification”. In: *Remote Sensing* 10.11 (2018), p. 1742 (cit. on p. 100).

[Ein+09] Michael Eineder, Nico Adam, Richard Bamler, Nestor Yague-Martinez, and Helko Breit. “Spaceborne spotlight SAR interferometry with TerraSAR-X”. In: *IEEE Transactions on Geoscience and Remote Sensing* 47.5 (2009), pp. 1524–1535 (cit. on p. 31).

[EKS83] Herbert Edelsbrunner, David Kirkpatrick, and Raimund Seidel. “On the shape of a set of points in the plane”. In: *IEEE Transactions on information theory* 29.4 (1983), pp. 551–559 (cit. on p. 50).

[Fer+11] Alessandro Ferretti, Alfio Fumagalli, Fabrizio Novali, Claudio Prati, Fabio Rocca, and Alessio Rucci. “A new algorithm for processing interferometric data-stacks: SqueeSAR”. In: *IEEE Transactions on Geoscience and Remote Sensing* 49.9 (2011), pp. 3460–3470 (cit. on pp. 15, 16, 28, 29, 52, 87, 97).

[Fle12] Karen Fletcher. *SENTINEL 1: ESA’s Radar Observatory Mission for GMES Operational Services*. European Space Agency, 2012 (cit. on pp. 3, 5, 15).

[For+14] Gianfranco Fornaro, Fabrizio Lombardini, Antonio Pauciullo, Diego Reale, and Federico Viviani. “Tomographic processing of interferometric SAR data: Developments, applications, and future research perspectives”. In: *IEEE Signal Processing Magazine* 31.4 (2014), pp. 41–50 (cit. on p. 30).

[For+15] Gianfranco Fornaro, Simona Verde, Diego Reale, and Antonio Pauciullo. “CAESAR: An approach based on covariance matrix decomposition to improve multibaseline–multitemporal interferometric SAR processing”. In: *IEEE Transactions on Geoscience and Remote Sensing* 53.4 (2015), pp. 2050–2065 (cit. on pp. 29, 55, 87).

[FPR01] Alessandro Ferretti, Claudio Prati, and Fabio Rocca. “Permanent scatterers in SAR interferometry”. In: *IEEE Transactions on geoscience and remote sensing* 39.1 (2001), pp. 8–20 (cit. on pp. 15, 27, 28, 39, 62, 97).

[FPS09] G Fornaro, A Pauciullo, and F Serafino. “Deformation monitoring over large areas with multipass differential SAR interferometry: a new approach based on the use of spatial differences”. In: *International Journal of Remote Sensing* 30.6 (2009), pp. 1455–1478 (cit. on p. 15).

[FRS09] Gianfranco Fornaro, Diego Reale, and Francesco Serafino. “Four-dimensional SAR imaging for height estimation and monitoring of single and double scatterers”. In: *IEEE Transactions on Geoscience and Remote Sensing* 47.1 (2009), pp. 224–237 (cit. on p. 30).

[FSS03] Gianfranco Fornaro, Francesco Serafino, and Francesco Soldovieri. “Three-dimensional focusing with multipass SAR data”. In: *IEEE Transactions on Geoscience and Remote Sensing* 41.3 (2003), pp. 507–517 (cit. on p. 30).

[GA12] Kanika Goel and Nico Adam. “An advanced algorithm for deformation estimation in non-urban areas”. In: *ISPRS journal of photogrammetry and remote sensing* 73 (2012), pp. 100–110 (cit. on pp. 15, 29).

[GA14] Kanika Goel and Nico Adam. “A distributed scatterer interferometry approach for precision monitoring of known surface deformation phenomena”. In: *IEEE Transactions on Geoscience and Remote Sensing* 52.9 (2014), pp. 5454–5468 (cit. on p. 29).

[GB12] Stefan Gernhardt and Richard Bamler. “Deformation monitoring of single buildings using meter-resolution SAR data in PSI”. In: *ISPRS journal of photogrammetry and remote sensing* 73 (2012), pp. 68–79 (cit. on p. 15).

[Ge+18] Nan Ge, Fernando Rodriguez Gonzalez, Yuanyuan Wang, Yilei Shi, and Xiao Xiang Zhu. “Spaceborne Staring Spotlight SAR Tomography—A First Demonstration With TerraSAR-X”. In: *IEEE Journal of Selected Topics in Applied Earth Observations and Remote Sensing* 99 (2018), pp. 1–14 (cit. on p. 31).

[Get12] Pascal Getreuer. “Chan-vese segmentation”. In: *Image Processing On Line* 2 (2012), pp. 214–224 (cit. on p. 50).

[GHS00] Paolo Gamba, Bijan Houshmand, and Matteo Saccani. “Detection and extraction of buildings from interferometric SAR data”. In: *IEEE Transactions on Geoscience and Remote Sensing* 38.1 (2000), pp. 611–617 (cit. on p. 48).

[Gia+08] Vito Martino Giacovazzo, Alberto Refice, Fabio Bovenga, and Nicola Veneziani. “Identification of coherent scatterers: Spectral correlation vs. multi-chromatic phase analysis”. In: *Geoscience and Remote Sensing Symposium, 2008. IGARSS 2008. IEEE International*. Vol. 4. IEEE. 2008, pp. IV–411 (cit. on p. 27).

[GL05] Fulvio Gini and Fabrizio Lombardini. “Multibaseline cross-track SAR interferometry: A signal processing perspective”. In: *IEEE Aerospace and Electronic Systems Magazine* 20.8 (2005), pp. 71–93 (cit. on p. 30).

[GLM02] Fulvio Gini, Fabrizio Lombardini, and Monica Montanari. “Layover solution in multibaseline SAR interferometry”. In: *IEEE Transactions on Aerospace and Electronic Systems* 38.4 (2002), pp. 1344–1356 (cit. on p. 30).

[GQ14] Donald Goldfarb and Zhiwei Qin. “Robust low-rank tensor recovery: Models and algorithms”. In: *SIAM Journal on Matrix Analysis and Applications* 35.1 (2014), pp. 225–253 (cit. on pp. 45, 57, 61, 68, 91).

[GRY11] Silvia Gandy, Benjamin Recht, and Isao Yamada. “Tensor completion and low-n-rank tensor recovery via convex optimization”. In: *Inverse Problems* 27.2 (2011), p. 025010 (cit. on p. 45).

[GT08] Andrea Monti Guarnieri and Stefano Tebaldini. “On the exploitation of target statistics for SAR interferometry applications”. In: *IEEE Transactions on Geoscience and Remote Sensing* 46.11 (2008), pp. 3436–3443 (cit. on pp. 23, 29).

[Gu+14] Shuhang Gu, Lei Zhang, Wangmeng Zuo, and Xiangchu Feng. “Weighted nuclear norm minimization with application to image denoising”. In: *Proceedings of the IEEE Conference on Computer Vision and Pattern Recognition*. 2014, pp. 2862–2869 (cit. on p. 61).

[Han01] Ramon F Hanssen. *Radar interferometry: data interpretation and error analysis*. Vol. 2. Springer Science & Business Media, 2001 (cit. on p. 22).

[Hir08] Heiko Hirschmuller. “Stereo processing by semiglobal matching and mutual information”. In: *IEEE Transactions on pattern analysis and machine intelligence* 30.2 (2008), pp. 328–341 (cit. on pp. 52, 54, 69).

[HO93] Per Christian Hansen and Dianne Prost O’Leary. “The use of the L-curve in the regularization of discrete ill-posed problems”. In: *SIAM Journal on Scientific Computing* 14.6 (1993), pp. 1487–1503 (cit. on p. 68).

[Hoo+04] Andrew Hooper, Howard Zebker, Paul Segall, and Bert Kampes. “A new method for measuring deformation on volcanoes and other natural terrains using InSAR persistent scatterers”. In: *Geophysical research letters* 31.23 (2004) (cit. on p. 27).

[Hoo06] Andrew John Hooper. *Persistent scatter radar interferometry for crustal deformation studies and modeling of volcanic deformation*. 2006 (cit. on pp. 27, 28).

[JDL14] Mi Jiang, Xiaoli Ding, and Zhiwei Li. “Hybrid Approach for Unbiased Coherence Estimation for Multitemporal InSAR.” In: *IEEE Trans. Geoscience and Remote Sensing* 52.5 (2014), pp. 2459–2473 (cit. on p. 29).

[Ji+16] Teng-Yu Ji, Ting-Zhu Huang, Xi-Le Zhao, Tian-Hui Ma, and Gang Liu. “Tensor completion using total variation and low-rank matrix factorization”. In: *Information Sciences* 326 (2016), pp. 243–257 (cit. on p. 36).

[Jia+15] Mi Jiang, Xiaoli Ding, Ramon F Hanssen, Rakesh Malhotra, and Ling Chang. “Fast statistically homogeneous pixel selection for covariance matrix estimation for multitemporal InSAR”. In: *IEEE Transactions on Geoscience and Remote Sensing* 53.3 (2015), pp. 1213–1224 (cit. on p. 15).

[Kam06] Bert M Kampes. *Radar interferometry*. Springer, 2006 (cit. on pp. 15, 27).

[Kan+17] Jian Kang, Yuanyuan Wang, Marco Körner, and Xiao Xiang Zhu. “Robust object-based multipass InSAR deformation reconstruction”. In: *IEEE Transactions on Geoscience and Remote Sensing* 55.8 (2017), pp. 4239–4251 (cit. on pp. 33, 57, 63, 68).

[Kan+18] Jian Kang, Yuanyuan Wang, Michael Schmitt, and Xiao Xiang Zhu. “Object-Based Multipass InSAR via Robust Low-Rank Tensor Decomposition”. In: *IEEE Transactions on Geoscience and Remote Sensing* 56.6 (2018), pp. 3062–3077 (cit. on p. 55).

[KB09] Tamara G Kolda and Brett W Bader. “Tensor decompositions and applications”. In: *SIAM review* 51.3 (2009), pp. 455–500 (cit. on pp. 19, 23, 58).

[KH04] Bert M Kampes and Ramon F Hanssen. “Ambiguity resolution for permanent scatterer interferometry”. In: *IEEE Transactions on Geoscience and Remote Sensing* 42.11 (2004), pp. 2446–2453 (cit. on p. 28).

[Lee+94] Jong-Sen Lee, Karl W Hoppel, Stephen A Mango, and Allen R Miller. “Intensity and phase statistics of multilook polarimetric and interferometric SAR imagery”. In: *IEEE Transactions on Geoscience and Remote Sensing* 32.5 (1994), pp. 1017–1028 (cit. on p. 23).

[LL14] Jingchen Liu and Yanxi Liu. “Local regularity-driven city-scale facade detection from aerial images”. In: *Proceedings of the IEEE Conference on Computer Vision and Pattern Recognition*. 2014, pp. 3778–3785 (cit. on p. 49).

[LMG03] Fabrizio Lombardini, Monica Montanari, and Fulvio Gini. “Reflectivity estimation for multibaseline interferometric radar imaging of layover extended sources”. In: *IEEE Transactions on Signal Processing* 51.6 (2003), pp. 1508–1519 (cit. on p. 30).

[Lom05] Fabrizio Lombardini. “Differential tomography: A new framework for SAR interferometry”. In: *IEEE Transactions on Geoscience and Remote Sensing* 43.1 (2005), pp. 37–44 (cit. on p. 30).

[LSG17] Qinghua Liu, Xinyue Shen, and Yuantao Gu. "Linearized admm for non-convex non-smooth optimization with convergence analysis". In: *arXiv preprint arXiv:1705.02502* (2017) (cit. on p. 36).

[Mar+15] Dimitrios Marmanis, F Adam, Mihai Datcu, Thomas Esch, and Uwe Stilla. "Deep neural networks for above-ground detection in very high spatial resolution digital elevation models". In: *ISPRS Annals of the Photogrammetry, Remote Sensing and Spatial Information Sciences* 2.3 (2015), p. 103 (cit. on p. 49).

[Mat+15] Gellert Mattyus, Shenlong Wang, Sanja Fidler, and Raquel Urtasun. "Enhancing road maps by parsing aerial images around the world". In: *Proceedings of the IEEE International Conference on Computer Vision*. 2015, pp. 1689–1697 (cit. on p. 49).

[MKS17] Takeshi Motohka, Yukihiro Kankaku, and Shinichi Suzuki. "Advanced land observing Satellite-2 (ALOS-2) and its follow-on L-band SAR mission". In: *2017 IEEE Radar Conference (RadarConf)*. IEEE. 2017, pp. 0953–0956 (cit. on pp. 3, 5, 15).

[Mor+13] Alberto Moreira, Pau Prats-Iraola, Marwan Younis, Gerhard Krieger, Irena Hajnsek, and Konstantinos P Papathanassiou. "A tutorial on synthetic aperture radar". In: *IEEE Geoscience and remote sensing magazine* 1.1 (2013), pp. 6–43 (cit. on pp. 19, 21).

[MU12] Ivan Markovsky and KONSTANTIN Usevich. *Low rank approximation*. Springer, 2012 (cit. on p. 55).

[NKL18] Sankarambadi Navneet, Jin-Woo Kim, and Zhong Lu. "A New InSAR Persistent Scatterer Selection Technique Using Top Eigenvalue of Coherence Matrix". In: *IEEE Transactions on Geoscience and Remote Sensing* 56.4 (2018), pp. 1969–1978 (cit. on p. 27).

[OPH96] Timo Ojala, Matti Pietikäinen, and David Harwood. "A comparative study of texture measures with classification based on featured distributions". In: *Pattern recognition* 29.1 (1996), pp. 51–59 (cit. on p. 49).

[OPM02] Timo Ojala, Matti Pietikainen, and Topi Maenpaa. "Multiresolution gray-scale and rotation invariant texture classification with local binary patterns". In: *IEEE Transactions on pattern analysis and machine intelligence* 24.7 (2002), pp. 971–987 (cit. on p. 49).

[OS88] Stanley Osher and James A Sethian. "Fronts propagating with curvature-dependent speed: algorithms based on Hamilton-Jacobi formulations". In: *Journal of computational physics* 79.1 (1988), pp. 12–49 (cit. on p. 49).

[OY13] Shunsuke Ono and Isao Yamada. "Optimized JPEG image decompression with super-resolution interpolation using multi-order total variation". In: *Image Processing (ICIP), 2013 20th IEEE International Conference on*. IEEE. 2013, pp. 474–478 (cit. on p. 41).

[PB+14] Neal Parikh, Stephen Boyd, et al. "Proximal algorithms". In: *Foundations and Trends® in Optimization* 1.3 (2014), pp. 127–239 (cit. on p. 25).

[PB11] Alessandro Parizzi and Ramon Brcic. “Adaptive InSAR stack multilooking exploiting amplitude statistics: A comparison between different techniques and practical results”. In: *IEEE Geoscience and Remote Sensing Letters* 8.3 (2011), pp. 441–445 (cit. on p. 29).

[Pen+14] Yigang Peng, Jinli Suo, Qionghai Dai, and Wenli Xu. “Reweighted low-rank matrix recovery and its application in image restoration”. In: *IEEE Transactions on cybernetics* 44.12 (2014), pp. 2418–2430 (cit. on p. 61).

[PFS17] Evangelos E Papalexakis, Christos Faloutsos, and Nicholas D Sidiropoulos. “Tensors for data mining and data fusion: Models, applications, and scalable algorithms”. In: *ACM Transactions on Intelligent Systems and Technology (TIST)* 8.2 (2017), p. 16 (cit. on p. 23).

[PPMA12] Béatrice Pinel-Puysségur, Rémi Michel, and Jean-Philippe Avouac. “Multi-link InSAR time series: Enhancement of a wrapped interferometric database”. In: *IEEE Journal of Selected Topics in Applied Earth Observations and Remote Sensing* 5.3 (2012), pp. 784–794 (cit. on p. 97).

[RB74] DCBP Rife and Robert Boorstyn. “Single tone parameter estimation from discrete-time observations”. In: *IEEE Transactions on information theory* 20.5 (1974), pp. 591–598 (cit. on pp. 28, 33).

[Ric03] John A Rice. *Mathematical statistics and data analysis*. China machine press Beijing, 2003 (cit. on p. 88).

[RM00] Andreas Reigber and Alberto Moreira. “First demonstration of airborne SAR tomography using multibaseline L-band data”. In: *IEEE Transactions on Geoscience and Remote Sensing* 38.5 (2000), pp. 2142–2152 (cit. on p. 30).

[Ros+00] Paul A Rosen, Scott Hensley, Ian R Joughin, Fuk K Li, Soren N Madsen, Ernesto Rodriguez, and Richard M Goldstein. “Synthetic aperture radar interferometry”. In: *Proceedings of the IEEE* 88.3 (2000), pp. 333–382 (cit. on p. 19).

[Sch+06] R Zandoná Schneider, Konstantinos P Papathanassiou, Irena Hajnsek, and Alberto Moreira. “Polarimetric and interferometric characterization of coherent scatterers in urban areas”. In: *IEEE Transactions on Geoscience and Remote Sensing* 44.4 (2006), pp. 971–984 (cit. on p. 27).

[SDT11] Aymen Shabou, Jérôme Darbon, and Florence Tupin. “A Markovian approach for InSAR phase reconstruction with mixed discrete and continuous optimization”. In: *IEEE Geoscience and Remote Sensing Letters* 8.3 (2011), pp. 527–531 (cit. on p. 35).

[SE+16] Sami Samiei-Esfahany, Joana Esteves Martins, Freek van Leijen, and Ramon F Hanssen. “Phase estimation for distributed scatterers in InSAR stacks using integer least squares estimation”. In: *IEEE Transactions on Geoscience and Remote Sensing* 54.10 (2016), pp. 5671–5687 (cit. on pp. 15, 29, 87).

[SF+15] Maria J Sanjuan-Ferrer, Irena Hajnsek, Konstantinos P Papathanassiou, and Alberto Moreira. "A new detection algorithm for coherent scatterers in SAR data". In: *IEEE Transactions on Geoscience and Remote Sensing* 53.11 (2015), pp. 6293–6307 (cit. on p. 27).

[Shi+18] Y. Shi, X. X. Zhu, W. Yin, and R. Bamler. "A Fast and Accurate Basis Pursuit Denoising Algorithm With Application to Super-Resolving Tomographic SAR". In: *IEEE Transactions on Geoscience and Remote Sensing* 56.10 (2018), pp. 6148–6158. ISSN: 0196-2892. DOI: 10.1109/TGRS.2018.2832721 (cit. on p. 31).

[Sid+16] Muhammad Adnan Siddique, Urs Wegmüller, Irena Hajnsek, and Othmar Frey. "Single-look SAR tomography as an add-on to PSI for improved deformation analysis in urban areas". In: *IEEE Transactions on Geoscience and Remote Sensing* 54.10 (2016), pp. 6119–6137 (cit. on p. 31).

[Sid+17] Nicholas D Sidiropoulos, Lieven De Lathauwer, Xiao Fu, Kejun Huang, Evangelos E Papalexakis, and Christos Faloutsos. "Tensor decomposition for signal processing and machine learning". In: *IEEE Transactions on Signal Processing* 65.13 (2017), pp. 3551–3582 (cit. on p. 23).

[SM+05] Petre Stoica, Randolph L Moses, et al. "Spectral analysis of signals". In: (2005) (cit. on p. 30).

[SO14] Keiichiro Shirai and Masahiro Okuda. "FFT based solution for multivariable L 2 equations using KKT system via FFT and efficient pixel-wise inverse calculation". In: *Acoustics, Speech and Signal Processing (ICASSP), 2014 IEEE International Conference on*. IEEE. 2014, pp. 2629–2633 (cit. on pp. 36, 41–43).

[Sou+11] Joaquim J Sousa, Andrew J Hooper, Ramon F Hanssen, Luisa C Bastos, and Antonio M Ruiz. "Persistent scatterer InSAR: a comparison of methodologies based on a model of temporal deformation vs. spatial correlation selection criteria". In: *Remote Sensing of Environment* 115.10 (2011), pp. 2652–2663 (cit. on p. 15).

[SST11] Simon Setzer, Gabriel Steidl, and Tanja Teuber. "Infimal convolution regularizations with discrete l1-type functionals". In: *Communications in Mathematical Sciences* 9.3 (2011), pp. 797–827 (cit. on p. 41).

[Ste70] Michael A Stephens. "Use of the Kolmogorov-Smirnov, Cramér-Von Mises and related statistics without extensive tables". In: *Journal of the Royal Statistical Society. Series B (Methodological)* (1970), pp. 115–122 (cit. on p. 28).

[SZ16a] Michael Schmitt and Xiao Xiang Zhu. "Demonstration of single-pass millimeterwave SAR tomography for forest volumes". In: *IEEE Geoscience and Remote Sensing Letters* 13.2 (2016), pp. 202–206 (cit. on p. 31).

[SZ16b] Muhammad Shahzad and Xiao Xiang Zhu. "Automatic detection and reconstruction of 2-D/3-D building shapes from spaceborne TomoSAR point clouds". In: *IEEE Transactions on Geoscience and Remote Sensing* 54.3 (2016), pp. 1292–1310 (cit. on p. 48).

[TBQ95] JA Tough, D Blacknell, and S Quegan. “A statistical description of polarimetric and interferometric synthetic aperture radar data”. In: *Proc. R. Soc. Lond. A* 449.1937 (1995), pp. 567–589 (cit. on p. 23).

[Teb10] Stefano Tebaldini. “Single and multipolarimetric SAR tomography of forested areas: A parametric approach”. In: *IEEE Transactions on Geoscience and Remote Sensing* 48.5 (2010), pp. 2375–2387 (cit. on p. 31).

[Thi+07] Antje Thiele, Erich Cadario, Karsten Schulz, Ulrich Thonnessen, and Uwe Soergel. “Building recognition from multi-aspect high-resolution InSAR data in urban areas”. In: *IEEE Transactions on Geoscience and Remote Sensing* 45.11 (2007), pp. 3583–3593 (cit. on p. 48).

[Tis+04] Céline Tison, J-M Nicolas, Florence Tupin, and Henri Maître. “A new statistical model for Markovian classification of urban areas in high-resolution SAR images”. In: *IEEE transactions on geoscience and remote sensing* 42.10 (2004), pp. 2046–2057 (cit. on p. 48).

[TTM07] Cline Tison, Florence Tupin, and Henri Maître. “A fusion scheme for joint retrieval of urban height map and classification from high-resolution interferometric SAR images”. In: *IEEE Transactions on Geoscience and remote Sensing* 45.2 (2007), pp. 496–505 (cit. on p. 48).

[TYH09] Min Tao, Junfeng Yang, and Bingsheng He. “Alternating direction algorithms for total variation deconvolution in image reconstruction”. In: *TR0918, Department of Mathematics, Nanjing University* (2009) (cit. on p. 35).

[Voi+13] Aurélie Voisin, Vladimir A Krylov, Gabriele Moser, Sebastiano B Serpico, and Josiane Zerubia. “Classification of very high resolution SAR images of urban areas using copulas and texture in a hierarchical Markov random field model”. In: *IEEE Geoscience and Remote Sensing Letters* 10.1 (2013), pp. 96–100 (cit. on p. 48).

[WAL18] Yanting Wang, Thomas L Ainsworth, and Jong-Sen Lee. “Evaluation of Coherent Scatterers in High-Resolution Polarimetric SAR Imagery”. In: *IGARSS 2018-2018 IEEE International Geoscience and Remote Sensing Symposium*. IEEE. 2018, pp. 5871–5874 (cit. on p. 27).

[Wan+17] Yuanyuan Wang, Xiao Xiang Zhu, Bernhard Zeisl, and Marc Pollefeys. “Fusing meter-resolution 4-D InSAR point clouds and optical images for semantic urban infrastructure monitoring”. In: *IEEE Transactions on Geoscience and Remote Sensing* 55.1 (2017), pp. 14–26 (cit. on pp. 33, 48).

[Wan+18] Yao Wang, Jiangjun Peng, Qian Zhao, Yee Leung, Xi-Le Zhao, and Deyu Meng. “Hyperspectral image restoration via total variation regularized low-rank tensor decomposition”. In: *IEEE Journal of Selected Topics in Applied Earth Observations and Remote Sensing* 11.4 (2018), pp. 1227–1243 (cit. on p. 36).

[WB10] Rolf Werninghaus and Stefan Buckreuss. “The TerraSAR-X mission and system design”. In: *IEEE Transactions on Geoscience and Remote Sensing* 48.2 (2010), pp. 606–614 (cit. on pp. 3, 5, 15, 30).

[WCX15] Fenghui Wang, Wenfei Cao, and Zongben Xu. “Convergence of multi-block Bregman ADMM for nonconvex composite problems”. In: *arXiv preprint arXiv:1505.03063* (2015) (cit. on p. 36).

[Weg+10] Urs Wegmuller, Diana Walter, Volker Spreckels, and Charles L Werner. “Nonuniform ground motion monitoring with TerraSAR-X persistent scatterer interferometry”. In: *IEEE Transactions on Geoscience and Remote Sensing* 48.2 (2010), pp. 895–904 (cit. on p. 27).

[WEG87] Svante Wold, Kim Esbensen, and Paul Geladi. “Principal component analysis”. In: *Chemometrics and intelligent laboratory systems* 2.1-3 (1987), pp. 37–52 (cit. on p. 55).

[Wer+03] Charles Werner, U Wegmuller, Tazio Strozzi, and Andreas Wiesmann. “Interferometric point target analysis for deformation mapping”. In: *Geoscience and Remote Sensing Symposium, 2003. IGARSS'03. Proceedings. 2003 IEEE International*. Vol. 7. IEEE. 2003, pp. 4362–4364 (cit. on p. 27).

[WZ16] Yuanyuan Wang and Xiao Xiang Zhu. “Robust estimators for multipass SAR interferometry”. In: *IEEE Transactions on Geoscience and Remote Sensing* 54.2 (2016), pp. 968–980 (cit. on pp. 15, 23, 28, 29, 33).

[WZB12] Yuanyuan Wang, Xiao Xiang Zhu, and Richard Bamler. “Retrieval of phase history parameters from distributed scatterers in urban areas using very high resolution SAR data”. In: *ISPRS Journal of Photogrammetry and Remote Sensing* 73 (2012), pp. 89 –99. ISSN: 0924-2716. DOI: http://dx.doi.org/10.1016/j.isprsjprs.2012.06.007 (cit. on pp. 15, 29, 87).

[WZB14] Yuanyuan Wang, Xiao Xiang Zhu, and Richard Bamler. “An efficient tomographic inversion approach for urban mapping using meter resolution SAR image stacks”. In: *IEEE Geoscience and Remote Sensing Letters* 11.7 (2014), pp. 1250–1254 (cit. on p. 15).

[WZS14] Jan Dirk Wegner, Jens R Ziehn, and Uwe Soergel. “Combining high-resolution optical and InSAR features for height estimation of buildings with flat roofs”. In: *IEEE Transactions on Geoscience and Remote Sensing* 52.9 (2014), pp. 5840–5854 (cit. on p. 48).

[YB13] Osama Yousif and Yifang Ban. “Improving urban change detection from multitemporal SAR images using PCA-NLM”. In: *IEEE Transactions on Geoscience and Remote Sensing* 51.4 (2013), pp. 2032–2041 (cit. on p. 55).

[YT03] Haibo Yao and Lei Tian. “A genetic-algorithm-based selective principal component analysis (GA-SPCA) method for high-dimensional data feature extraction”. In: *IEEE Transactions on Geoscience and Remote Sensing* 41.6 (2003), pp. 1469–1478 (cit. on p. 55).

[ZB10a] Xiao Xiang Zhu and Richard Bamler. “Tomographic SAR inversion by L1-norm regularization—The compressive sensing approach”. In: *IEEE Transactions on Geoscience and Remote Sensing* 48.10 (2010), pp. 3839–3846 (cit. on p. 31).

[ZB10b] Xiao Xiang Zhu and Richard Bamler. “Very high resolution spaceborne SAR tomography in urban environment”. In: *IEEE Transactions on Geoscience and Remote Sensing* 48.12 (2010), pp. 4296–4308 (cit. on pp. 30, 31, 48).

[ZB14] Xiao Xiang Zhu and Richard Bamler. “Superresolving SAR tomography for multidimensional imaging of urban areas: Compressive sensing-based TomoSAR inversion”. In: *IEEE Signal Processing Magazine* 31.4 (2014), pp. 51–58 (cit. on p. 31).

[ZC08] Mingqiang Zhu and Tony Chan. “An efficient primal-dual hybrid gradient algorithm for total variation image restoration”. In: *UCLA CAM Report* 34 (2008) (cit. on p. 35).

[ZDL11] Lei Zhang, Xiaoli Ding, and Zhong Lu. “Modeling PSInSAR time series without phase unwrapping”. In: *IEEE Transactions on Geoscience and Remote Sensing* 49.1 (2011), pp. 547–556 (cit. on pp. 15, 28).

[ZGS15a] X. X. Zhu, N. Ge, and M. Shahzad. “Joint Sparsity in SAR Tomography for Urban Mapping”. In: *IEEE Journal of Selected Topics in Signal Processing* 9.8 (2015), pp. 1498–1509. ISSN: 1932-4553. DOI: 10.1109/JSTSP.2015.2469646 (cit. on p. 15).

[ZGS15b] Xiao Xiang Zhu, Nan Ge, and Muhammad Shahzad. “Joint sparsity in SAR tomography for urban mapping”. In: *IEEE Journal of Selected Topics in Signal Processing* 9.8 (2015), pp. 1498–1509 (cit. on p. 31).

[Zha+14] Hongyan Zhang, Wei He, Liangpei Zhang, Huanfeng Shen, and Qiangqiang Yuan. “Hyperspectral image restoration using low-rank matrix recovery”. In: *IEEE Transactions on Geoscience and Remote Sensing* 52.8 (2014), pp. 4729–4743 (cit. on p. 57).

[Zho+15] Xiaowei Zhou, Can Yang, Hongyu Zhao, and Weichuan Yu. “Low-rank modeling and its applications in image analysis”. In: *ACM Computing Surveys (CSUR)* 47.2 (2015), p. 36 (cit. on p. 55).

[Zhu+13] Xiao Xiang Zhu, Yuanyuan Wang, Stefan Gernhardt, and Richard Bamler. “Tomo-GENESIS: DLR’s tomographic SAR processing system”. In: *Urban Remote Sensing Event (JURSE), 2013 Joint*. IEEE. 2013, pp. 159–162 (cit. on p. 48).

[Zhu+97] Ciyou Zhu, Richard H Byrd, Peihuang Lu, and Jorge Nocedal. “Algorithm 778: L-BFGS-B: Fortran subroutines for large-scale bound-constrained optimization”. In: *ACM Transactions on Mathematical Software (TOMS)* 23.4 (1997), pp. 550–560 (cit. on p. 36).

[ZRH97] Howard A Zebker, Paul A Rosen, and Scott Hensley. “Atmospheric effects in interferometric synthetic aperture radar surface deformation and topographic maps”. In: *Journal of Geophysical Research: Solid Earth* 102.B4 (1997), pp. 7547–7563 (cit. on p. 22).

[ZV92] Howard A Zebker and John Villasenor. “Decorrelation in interferometric radar echoes”. In: *IEEE Transactions on geoscience and remote sensing* 30.5 (1992), pp. 950–959 (cit. on p. 22).

List of figures

List of tables

Acknowledgments

Here, I would like to thank many people's support for the work in this thesis.

First and foremost, I would like to thank my supervisor Prof. Zhu for providing me an interesting research topic and the scientific discussions. Her excellent PhD work and the passion for novel technology have always been leading me to do better research. I also want to express my gratitude towards Prof. Bamler, who does not hesitate to share his critical comments and insights for all the students. Moreover, I would like to express my thanks to Dr. Wang, who has patiently supported me in my PhD research.

I also want to thank in particular Dr. Schmitt, Dr. Yokoya, Dr. Körner, Dr. Ghamisi, Dr. Baier and Dr. Xu. They share their valuable advice and research experiences, which help me a lot to overcome the difficulties I met during my PhD life.

Hereby, it's also my pleasure to mention all the great colleagues, who I worked with in the past years. I would like to thank Dr. Shazad, for the invitation of Pakistan food, Dr. Werner, for the ride to Bodensee during the summer school, Dr. Montazeri, for never missing my oral talks, Dr. Ansari, for every wonderful speech in the conference, Dr. Hoegner, for the organization of beer event during oktoberfest, Nan Ge, for his precise attitude to everything, which I respect, Jingliang Hu, for the leader as SiPEO team event and his humor which makes everyone laugh, Yao Sun, for her kindness when you need help, Danfeng Hong, for his passion and the attitude in doing research and his sincerity for sharing his ideas, Hossein Bagheri, for his saffron from Iran, Lichao Mou, for the thought sharing in Valencia, Chunping Qiu, for her hand-made Baozi as the breakfast, Lloyd Hughes, for his kind help when I have IT related problems, Rong Huang, who does not hesitate to share her sincere thoughts and her invitation of hot pot, Tobias Koch, for his IT support for others and openness to hear my stories, Sandra Aigner, for her kindness whenever you need help and the cooperation of our joint workshop in the summer school, Lukas Liebel, for his help in how to use LRZ DGX, Richard Boerner, who always was a helping hand, Yuansheng Hua, for his perfect travel guidance in Valencia, Zhen Ye, for being a good listener, Bo Zhang, for sharing his GIS background, Tengyu Ji, for his deep knowledge in optimization, and Yuan Zhang, for his invitation of hot pot in his apartment.

Especially, I would like to express my thankfulness to my third supervisor, Prof.Sörgel, who invited me to give a presentation about my PhD work in Stuttgart. His kind comments and suggestions really helped me a lot for my presentation. I am very appreciated of his support.

Furthermore, I would like to thank Prof. Fraundorfer, who hosted me as a visiting researcher in TU Graz, and the discussions with him inspired me a lot. Many thanks also go for his team members: they not only demonstrate their creativity in computer vision, but also suggest the delicious food of Graz.

I also need to thank my bachelor and master supervisor, Prof. Wang, who opened a door for me in radar signal processing field and guided me through my bachelor and master thesis.

Also, I would like to thank Dr. Zhang, who helped me a lot for doing research in TUM.

Last but not least, I would like to thank my wife, Hongli Yin, who always accompanies with me whenever I have troubles and supports me in my life, and my parents who selflessly support my every decision and back me up.